UNIVERSITEIT ANTWERPEN
UNIVERSITAIRE INSTELLING ANTWERPEN
Departement Natuurkunde

Schatten van Signaal en Ruis in Magnetische Resonantie Beelden

Signal and Noise Estimation from Magnetic Resonance Images

Proefschrift voorgelegd tot het behalen van de graad van

Doctor in de Wetenschappen

aan de Universitaire Instelling Antwerpen, te verdedigen door

Jan SIJBERS

Promotor: Prof. Dr. Dirk Van Dyck
Copromotor: Prof. Dr. Erik Raman

Antwerpen, 1998

.

Contents

Dankwoord

- Op de eerste plaats zou ik Prof. Dr. Dirk Van Dyck willen danken voor zijn onuitputbare bron van ideeën en voor zijn niet-te-dempen optimisme en enthousiasme voor de wetenschap. Hij had steeds een geschikt antwoord op gestelde vragen over eender welk onderwerp, zelfs wanneer hij slechts enkele seconden tijd had ...

- Daarnaast ben ik veel verschuldigd aan Prof. Dr. Erik Raman voor de kans die me geboden werd het onderzoek te starten binnen de groep Biomedische Fysica, hetgeen resulteerde in dit proefwerk, en voor de voortdurende morele ondersteuning tijdens dat onderzoek, evenals tijdens de begeleiding van studenten.

- Aan Dr. Paul Scheunders voor de wetenschappelijke begeleiding tijdens de eerste jaren van mijn doctoraal onderzoek, evenals voor de morele steun tijdens sommige moeilijke momenten in die periode.

- Een speciaal woord van dank gaat uit naar Dr. A. J. den Dekker (Arjan voor de vrienden) van de Technische Universiteit van Delft. Tijdens Arjans verblijf op de Universiteit van Antwerpen, hebben we van elkaars kennis kunnen profiteren, hetgeen leidde tot een erg vruchtbare wetenschappelijke samenwerking. Belangrijker is echter dat ik een nu vriend rijker ben ...

- Aan Dr. Annemie Van der Linden, Ir. Johan Van Audekerke en Dr. Marleen Verhoye van het bruisende en hoogst in-vivo Bio Imaging Lab voor de voortdurende aanvoer van experimentele MR data om onze bevindingen te testen.

- Aan Eva Bettens, mijn kamergenote, voor het delen van de interessante (maar soms ondankbare) taak van PC-beheer. Eva is trouwens de enige in't Visielab die een computer kan herstellen met een eenvoudige 'female touch'.

- To Johan Garcia en Piotr Jedrasik for keeping me company during the weekends. To Johan, I'm also grateful for encouraging me to study some books on stochastic processes: it helped me a lot indeed.

- Aan Dirk Meersman and Johan Van Audekerke voor het onderhoud van de HP werkstations.

- Aan Paul, Gert, Steve, Dirk and Staf voor het spelen van bridge tijdens de middagpauze, zodat zelfs tijdens de pauze mijn mentale conditie op peil bleef.

- Aan alle andere leden van het Visielab, Biomedische Fysica, Bio Imaging lab en het Departement Natuurkunde, in het bijzonder aan Hilde, Marise en Suzan van het secretariaat.

- Tenslotte dank ik hierbij mijn ouders en mijn vrouw An voor alles wat ze voor me gedaan hebben. Hopelijk kunnen we nu iets meer tijd met elkaar doorbrengen ...

Summary

This thesis deals with the estimation of noise and signal from Magnetic Resonance (MR) images with a special reference to magnitude MR images. Other subjects in this work, related to this topic, include the estimation and improvement of the image signal-to-noise ratio (SNR) and an application to 3D segmentation.

After a short introduction on the principles of MR imaging, the thesis starts with an overview of the origin and statistical properties of MR noise and signal (Chapter 2). In the same chapter, it is also clarified which factors influence the SNR during an image acquisition.

In order to process experimental data in a scientifically justified manner, knowledge of the underlying probability density function (PDF) is indispensable. For this reason, in Chapter 3, the probability distributions of raw as well as of processed MR data are derived. Thereby, distinction has been drawn between the PDF of complex data, before and after the Fourier transform, and the PDF of processed or derived MR data. For in practice, instead of treating the raw complex data, one often works with magnitude or phase data as these types of data are often directly related to physical quantities such as the pseudo-proton density, flow or diffusion. Characteristic PDF's for processed data are discussed in Chapter 3 to serve as a basis for solving of various estimation problems.

The estimation problems include estimation of noise and signal from MR data which are discussed in Chapter 4 and 5, respectively. In both chapters, conventional estimation techniques are compared to the Maximum Likelihood (ML) estimation method where use is made of the specific PDF characterizing the MR data. Conventional estimation methods are in general based on Gauss distributed data. However, magnitude and phase data are not 'normally' distributed. Hence, conventional estimation methods often yield biased results. In Chapter 4 and 5, it is shown how the knowledge of the proper PDF can be used to avoid (or at least reduce) systematic errors during the estimation of noise or signal.

In Chapter 6, the importance of ML estimation using the correct PDF is illustrated in the estimation of T_1- and T_2-maps. The construction of such maps is a common technique to visualize characteristic physiological information. However, T_1- and T_2-maps are often derived from magnitude MR data, which are Rice distributed. Again, to the author's knowledge, this information is hardly exploited. Though, the Rice distribution has a significant influence on the quantitative determination of T_1- and T_2-maps. This is demonstrated in Chapter 6.

In Chapter 7 and 8, attention has been paid to the estimation and improvement, respectively, of the image SNR. An efficient and accurate method for the estimation of the image SNR is proposed, based on the cross-correlation of two realizations of the same image. In Chapter 8 it is shown that cross-correlation can as well be used to improve the image SNR. However, improving the SNR often goes along with a degradation of spatial resolution. Therefore, an adaptive and anisotropic diffusion filter is discussed. Application of the diffusion filter results in a major improvement of the image SNR while retaining the spatial resolution.

Finally, in Chapter 9, the use of the adaptive, anisotropic diffusion filter is demonstrated in the description of a new segmentation technique which was developed for precise and accurate volume quantization from 3D MR data. The proposed method is semi-automatic and allows to guide the segmentation process in an interactive way. Several applications are discussed.

Chapter 1

Introduction

From the discovery of the nuclear magnetic resonance (NMR) phenomenon in materials by the group of Bloch and Purcell in 1946, the popularity of the NMR technique has been increased ever since [1, 2]. During the next decennia, NMR applications were mainly situated in the structure analysis of materials. It was not before 1973 that, by Lauterbur, the NMR phenomena could be exploited for imaging [3]. Magnetic resonance imaging (MRI) was born and a huge amount of papers on MRI appeared. Initially, these papers mainly dealt with the improvement of the MRI experiment itself: new imaging sequences were developed, and major improvements were reported on MRI hardware. From the early eighties on, research tended to focus also on processing of MR images.

In this chapter, the principles of MR imaging are briefly reviewed. For an excellent and complete description of the principles of magnetic resonance (imaging) it is referred to the work of Slichter and Callaghan [4, 5].

1.1 The intrinsic MR signal

The MR signal generally originates from hydrogen nuclei (protons). A proton has a property of intrinsic angular momentum, often referred to as spin $\vec{I}$, with an associated magnetic moment $\vec{\mu}$:

$$\vec{\mu} = \gamma \vec{I} \quad , \tag{1.1}$$

with γ denoting the gyromagnetic ratio unique to each atom. In a single volume element corresponding to a pixel in an MR image, there are many such protons, each with an associated moment. The net magnetization $\vec{M}$ is the resultant of the individual dipole moments contained therein. In absence of a magnetic field, the orientation of the individual dipole moments will be random. Hence, the net magnetization will be zero. In a static magnetic induction $\vec{B}_0$, conventionally oriented along the spatial direction z, the energy levels of the spins are splitted. The energy separation ΔE between the levels is given by:

$$\Delta E = \hbar \gamma B_0 \quad , \tag{1.2}$$

with $\hbar$ Planck's constant divided by 2π. The lowest energy state of the spins corresponds to an orientation along $\vec{B}_0$. Hence, in equilibrium and in absence of thermal energy, the net magnetization $\vec{M}_0$ will be orientated along $\vec{B}_0$. On the other hand, thermal energy drives the individual spins toward random orientations. In thermal equilibrium, these tendencies are balanced with the net magnetization being aligned parallel to $\vec{B}_0$ with a strength corresponding to the Boltzmann distribution of the possible energy states of the proton [5]:

$$\rho_m = \frac{\exp(\hbar \gamma m B_0 / k_b T_s)}{\sum\limits_{m=-I}^{I} \exp(\hbar \gamma m B_0 / k_b T_s)} \quad , \tag{1.3}$$

1

with m the magnetic quantum number, k_b the Boltzman constant, and T_s the sample temperature. Usually the energy $\hbar\gamma B_0$ is much smaller than $k_b T_s$ such that Eq. (1.3) can be approximated by:

$$\rho_m \simeq \left(1 + \frac{\hbar\gamma m B_0}{k_b T_s}\right)/(2I + 1) \quad . \tag{1.4}$$

The magnetization M_0 per unit volume is given by [6]:

$$M_0 \;=\; N_s \sum_{m=-I}^{I} \rho_m \hbar\gamma m \tag{1.5}$$

$$\simeq\; N_s \frac{\gamma^2 \hbar^2 I(I+1)B_0}{3k_b T_s} \quad , \tag{1.6}$$

with N_s the number of spins at resonance per unit volume. In general, the behaviour of the spins must be described by quantummechanics. However, if the number of spins N_s is huge, classical mechanics has been shown to be suited for the description of the net magnetic moment $\vec{M}$ behaviour [4] in a magnetic induction field $\vec{B}$:

$$\frac{d\vec{M}}{dt} = \gamma\vec{M} \times \vec{B} \quad . \tag{1.7}$$

1.2 Excitation and relaxation

In thermal equilibrium, the net magnetization $\vec{M}_0$ is oriented along $\vec{B}_0$, i.e., along the z direction. In a typical MR experiment, the equilibrium is disturbed via a resonant radio frequent (RF) pulse. Resonant energy absorption by the spin system occurs with an angular frequency $\omega_0 = \gamma B_0$, often referred to as the Larmor frequency.

After excitation, the net magnetization $\vec{M}$ relaxes back to its original state, during which energy is transferred from the spin system to the molecular environment. The spin-lattice energy transfer only contributes to the relaxation of M_z and occurs exponentially with a time constant T_1. Therefore, T_1 is called the spin-lattice or the longitudinal relaxation time. The initial phase coherence of the spins, immediately after excitation, is disturbed through spin-spin interaction such that $M_{x,y}$ decreases to zero exponentially with a time constant T_2. T_2 is called the spin-spin or the transversal relaxation time. Excitation and relaxation are phenomenologically described by the Bloch equations [6] from a frame rotating with angular frequency ω:

$$\frac{dM_x}{dt} \;=\; \gamma M_y(B_0 - \omega/\gamma) - \frac{M_x}{T_2} \tag{1.8}$$

$$\frac{dM_y}{dt} \;=\; \gamma M_z B_1 - \gamma M_x(B_0 - \omega/\gamma) - \frac{M_y}{T_2} \tag{1.9}$$

$$\frac{dM_z}{dt} \;=\; \gamma M_y B_1 - \frac{M_z - M_0}{T_1} \quad , \tag{1.10}$$

where B_1 denotes the magnitude of the RF pulse magnetic induction, which is conventionally directed along the x-axis. In case the rotating frame precesses with the Larmor frequency, after RF perturbation, relaxation occurs according to:

$$M_{x,y}(t) \;=\; M_{x,y}(0)\exp\left(-\frac{t}{T_2}\right) \tag{1.11}$$

$$M_z(t) \;=\; M_z(0)\exp\left(-\frac{t}{T_1}\right) + M_0\left(1 - \exp\left(-\frac{t}{T_1}\right)\right) \quad . \tag{1.12}$$

By placing a couple of conductive coils around the system, the relaxation and rotation of $\vec{M}_{xy}$ will induce a complex electric signal in the coils: the Free Induction Decay (FID) signal.

1.3 Image formation

In order to obtain an MR image, physical hardware is needed to encode spatial information into the MR signal and a mathematical tool is needed to decode the measured signals. Spatial information is encoded through application of slice selecting, frequency encoding, and/or phase encoding magnetic field gradients. During the time these gradients are applied, the precession frequencies of the voxel magnetizations are modulated, depending on their spatial coordinates $\vec{r}$:

$$\omega(\vec{r}) = \gamma(B_0 + \vec{G}.\vec{r}) \quad , \tag{1.13}$$

with $\vec{G}$ denoting the magnetic field gradient vector. The MR signal received is the total signal coming from all voxel magnetizations excited by the RF pulse. Ignoring the precession due to the main magnetic induction B_0, we have:

$$S(t) = \iiint \beta(\vec{r}) \exp\left(i\gamma\vec{G}.\vec{r}t\right) d\vec{r} \quad , \tag{1.14}$$

where $d\vec{r}$ is used to represent volume integration. In Eq. (1.14), $\beta(\vec{r})$ denotes the magnetic resonance coefficient, representing the spin density, weighted by for example T_1 and T_2 relaxation:

$$\beta(\vec{r}) = \rho(\vec{r})f(T_1(\vec{r}), T_2(\vec{r})) \quad , \tag{1.15}$$

where the function $f(.)$ is determined by the scanning pulse sequence.

An inverse discrete Fourier transform is used to decode the acquired MR signals. Indeed, Eq. (1.14) has the form of a Fourier transformation. To make this more obvious, Mansfield introduced the concept of a reciprocal space vector $\vec{k}$, given by [7]:

$$\vec{k} = \frac{1}{2\pi}\gamma\vec{G}t \quad . \tag{1.16}$$

For this reason, the Fourier space, in which MR signals are acquired, is often referred to as the K-space. Fourier reconstruction is the most commonly used reconstruction method in MR imaging that results in a final complex valued image given by:

$$\beta(\vec{r}) = \iiint S(\vec{k}) \exp\left(-i\vec{k}.\vec{r}\right) d\vec{k} \quad . \tag{1.17}$$

Hence an MR image is a spatial representation of the magnetization distribution.

Chapter 2

Signal and noise in MRI

2.1 Introduction

Signal-to-noise considerations are of prime importance in MRI because the nuclear magnetic resonance signal is inherently weak. This section gives an insight into the various parameters influencing the SNR in an MR experiment. Only these considerations on signal and noise in MRI that are considered important for the understanding of the thesis, are given.

2.2 The MR signal

The MR signal is the electro-magnetic force (*emf*) induced in a coil by a rotating magnetization. The larger this magnetization, the larger the MR signal. The magnetization M_0 per unit volume is given by [6]:

$$M_0 = N_s \sum_{m=-I}^{I} \rho_m \hbar \gamma m \tag{2.1}$$

$$= \frac{N_s \gamma^2 \hbar^2 I(I+1) B_0}{3 k_b T_s} \quad , \tag{2.2}$$

with N_s the number of spins at resonance per unit volume.
An elegant way to determine the *emf* was proposed by Hoult and Richards [8]:

$$S(t) = -\frac{\partial}{\partial t} \left(\vec{B}_1 \cdot \vec{M}_0 \right) \quad . \tag{2.3}$$

Here, $\vec{B}_1 \equiv \vec{B}_1(\vec{r}, t)$ denotes the magnetic induction, produced by a coil carrying unit current at $\vec{M}_0 \equiv M_0(\vec{r})$. For a sample with volume V_s the *emf* becomes:

$$S(t) = -\int_{V_s} \frac{\partial}{\partial t} \left(\vec{B}_1 \cdot \vec{M}_0 \right) d\vec{r} \quad . \tag{2.4}$$

If $\vec{B}_1$ is assumed to be homogeneous over the sample, the signal is easily seen to be:

$$S(t) = K \omega_0 B_{1,xy} M_0 V_s \cos \omega_0 t \quad , \tag{2.5}$$

with ω_0 the angular frequency with which the magnetization $\vec{M}_0$ precesses in the main magnetic induction $\vec{B}_0$. The factor K includes possible inhomogeneities of $\vec{B}_1$ over the sample.

2.2.1 Imaging parameters

In MRI, many different pulse sequences are available. The choice of the sequence parameters will have an influence on the amount of signal coming from the object and hence will affect the SNR. These parameters include the echo time TE, the inversion time TI, the repetition time TR, the flip angle α, the shape of the radio frequent pulses, etc. The actual relationship between those parameters and the SNR was investigated by Edelstein et al. for a spin echo (SE) and inversion recovery (IR) imaging sequence [9]. Also the data sampling period is an important parameter affecting the signal-to-noise ratio (SNR). A detailed discussion was provided by Mugler and Brookeman [10].

2.3 The noise

2.3.1 Thermal noise

Once generated, the MR signal is processed by the receiver chain. Each component in the chain is a source of noise. The noise generated by the receiver coil, is the first to be considered. In any conductor/resistor, thermal noise is produced by the stochastic motion of free electrons. These free electrons collide with atoms, resulting in an exchange of energy. The electron motion, and hence the number of collisions, depends on the coil temperature. The resultant thermal noise power $\langle V^2 \rangle$, coming from the coil resistance, is given by:

$$\langle V^2 \rangle = 4k_b T_c \Delta\nu R_c \quad , \tag{2.6}$$

with T$_c$ the coil temperature, $\Delta\nu$ the receiver frequency bandwidth, and R_c the coil resistance. Note that a wider receiver bandwidth increases the system noise. From Eq. (2.6) it is clear that an increase in sensitivity of about a factor 3 may be expected if the receiving coil is cooled to e.g., liquid nitrogen temperature (77K). This is however only true if the noise coming from the preamplifier, is negligible. Prediction of the SNR becomes difficult as the calculation of the coil resistance R_c may not be performed accurately. E.g., for a long, straight cylindrical conductor R_c is given by:

$$R_c = \frac{l}{p} \sqrt{\frac{\mu_r \mu_0 \omega \rho \left(T_c\right)}{2}} \quad , \tag{2.7}$$

with l, p, μ_r and ρ the length, circumference, permeability and resistivity of the conductor, respectively. Other conductor configurations, such as the saddle-shaped coils, were discussed by Hoult and Richards [8].
Thermal noise is often termed *Johnson noise* after J.B. Johnson who, in 1928, experimentally investigated the effects of thermal noise. At the same time, H. Nyquist studied thermal noise theoretically. A full derivation of thermal noise voltage was given by Connor in 1982 [11].
The spectral density of thermal noise is given by:

$$S_n(\vec{k}) = 2k_b T_c R_c \quad . \tag{2.8}$$

As the spectral density is uniform, Johnson noise is often referred to as *white noise*. Furthermore, it can be shown that thermal noise is characterized by a Gauss probability density function [12].

2.3.2 Sample losses

Loss of sensitivity also occurs because of the resistivity of the object to be imaged. These losses are associated, when signal is being received, with the induction of noise from the sample in the receiving coils, thus reducing sensitivity. Inductive losses were discussed in detail by Hoult and Lauterbur for several coil configurations [13]. They investigated noise originating from the human sample. Every

coil has a distributed capacitance and the human body, when placed inside the coil, acts as a dielectric medium. The effective resistance R_e characterizes the resultant dielectric loss. Furthermore, the resistivity of human tissue causes an actual reduction in the penetration of the RF field. The RF field is effectively shielded by currents caused by magnetic induction within the surface layers of the sample. This is referred to as the *skin depth* effect [14, 15]. The resultant thermal noise by these currents has an associated resistance R_m. In conclusion, placing the object inside the coil results in an increase of the series impedance. Hence, the noise power is more realistic given by:

$$\langle V^2 \rangle = 4k_b T_c \Delta\nu (R_c + R_e + R_m) \quad . \tag{2.9}$$

Again, the total noise component will be Gauss distributed.

2.3.3 Imaging parameters

Next to the MR system characteristics, the noise variance is also influenced by the imaging parameters. These parameters include the number of samples in the x and y directions (N_x, N_y), the number of averages (N_{av}), the field of view in the x and y directions $(\text{FOV}_x, \text{FOV}_y)$ and the sampling interval (Δt). The relationship of these parameters to the image noise variance was discussed in detail by Parker and Gullberg [16]. In this paragraph, only the main results are mentioned.

The noise variance is derived from the acquisition of an image containing only noise. Fourier reconstruction of the raw data yields:

$$i_n(x,y) = \sum_{k_x=0}^{N_x-1} \sum_{k_y=0}^{N_y-1} n(k_x \Delta t + k_y \Delta T) \exp\left[-2\pi i \left(\frac{xk_x}{N_x} + \frac{yk_y}{N_y}\right)\right] \Delta f_x \Delta f_y \quad , \tag{2.10}$$

with ΔT the time elapse between two phase encoding steps and (k_x, k_y) denoting the K-space coordinates. Δf_x and Δf_y are the K-space sampling intervals: $\Delta f_x = \gamma G_x \Delta t$ and $\Delta f_y = \gamma G_y T_y$, where γ is the gyro-magnetic ratio and G_x and G_y are the magnetic gradient strengths in the respective directions. T_y denotes the time interval the phase-encoding gradient was activated. Then the expected reconstructed image variance can be written:

$$\sigma^2[i_n(x,y)] = \frac{\Delta f_x^2 \Delta f_y^2}{N_{av}} \sum_{k_x=0}^{N_x-1} \sum_{k_y=0}^{N_y-1} \sum_{k_x'=0}^{N_x-1} \sum_{k_y'=0}^{N_y-1} E[n(k_x \Delta t + k_y \Delta T)$$
$$n(k_x' \Delta t + k_y' \Delta T)] \exp\left[-2\pi i \left(\frac{x(k_x - k_x')}{N_x} + \frac{y(k_y - k_y')}{N_y}\right)\right] \quad . \tag{2.11}$$

Over the sampling time intervals used in MRI, which is of the order of microseconds, the noise voltage is completely uncorrelated. This is true because most of the thermal noise energy is found in the infrared frequencies ($> 10^{10}$ Hz). From this observation, Eq. (2.11) can be computed to yield:

$$\sigma^2[i_n(x,y)] = K \frac{N_x N_y \langle V^2 \rangle}{N_{av} \text{FOV}_x^2 \text{FOV}_y^2 \Delta t} \quad , \tag{2.12}$$

where the noise power $\langle V^2 \rangle$ is given by Eq. (2.9), and K is a factor depending on the filter characteristics.

2.3.4 Structured noise

Structured noise is defined as signal contributions that have a non-random nature and that only affect a certain area of the image [17]. Examples of structured noise include ghosting, ringing, DC artifacts

and non-uniform signal distributions. The causes of structured noise are numerous, originating from equipment malfunction such as drift of the magnetic induction, and external interference such as radio frequency (RF) pickup. Usually, with careful engineering design and setup, most sources can be eliminated or minimized. However, those that remain, present difficulties in SNR estimation.

External RF interference can be a contributor to both random and structured noise in the MR image. Several authors addressed the need for adequate decoupling between the transmit and receive circuitry to prevent noise interference. Further sources of RF interference can be broadcasting stations and close proximity of electrical equipment, such as computers. In practice however, if great care is taken to shield interference using an effective RF cage, this source of noise can be eliminated.

Chapter 3

Probability density functions of MR data

3.1   Introduction

Image processing can hardly be practiced without knowledge of the proper data probability density function (PDF). Knowledge of the data PDF is vital for image processing techniques based on parameter estimation such as noise filtering or image restoration. In this chapter, various ways in which MR data appear, are discussed and the PDF of the raw and processed MR data are derived.

After acquisition of the MR data in K-space, commonly the complex valued data are Fourier transformed to obtain the magnetization distribution. It will be shown that, before as well as after the Fourier transform, the complex data will be characterized by a Gauss PDF. Although all information is contained in the real and imaginary parts of the Fourier transformed data, it is common practice to work with magnitude and phase data as they have more physical meaning. For example, flow information can be obtained from either the magnitude or the phase of the MR signal. Similarly, magnetic susceptibility, chemical shift and perfusion can all be encoded using either the magnitude or phase angle. However, computation of a magnitude image is a nonlinear operation in which the Gauss PDF of the pixels is transformed into a Rice PDF [18, 19]. In addition, Rice distributed data do not solely occur in conventional magnitude reconstructed data, they are also found in phase contrast MR (PCMR) or angiography imaging [20]. It will be shown that PCMR data are governed by a generalized Rice PDF.

3.2   PDF of raw MR data

During the acquisition, complex valued MR signals are sampled in the K-space. These sampled data are referred to as raw MR data. From Chapter 2, we know that the noise contributions of the complex valued raw MR data are additive and uncorrelated, characterized by a zero mean Gauss PDF [12, 21]. As was discussed in Chapter 1, an MR image is obtained by estimating Fourier coefficients of the acquired complex signals. The optimal coefficient estimates, in terms of precision, are obtained via a simple (inverse) Fourier transformation, provided that the raw MR data are Gauss distributed [22]. After the inverse Fourier transform, the complex data are still independent and Gauss distributed due to the linearity and orthogonality of the Fourier transform [1][23].

Let A and ϕ be the true amplitude and phase of a given complex data point such that $A\cos\phi$ and

---

[1]It will be assumed that the MR signals are sampled on a uniform grid in K-space. Furthermore, the variance of the noise will be assumed to be equal for each raw data point.

$A \sin \phi$ represent the true real and imaginary values, respectively. As the real and imaginary data are independent, the joint PDF of the complex data is simply the product of the real and imaginary PDF:

$$p(R, I | A, \phi, \sigma) = \frac{1}{2\pi\sigma^2} e^{-\frac{(A\cos\phi - R)^2}{2\sigma^2}} e^{-\frac{(A\sin\phi - I)^2}{2\sigma^2}} \quad , \tag{3.1}$$

where σ denotes the standard deviation of the data, and R and I are the real and imaginary data, respectively.

3.3 PDF of magnitude data

As was stated before, it is common practice to work with magnitude data instead of real and imaginary data because magnitude data have the advantage to be immune to the effects of incidental phase variations due to RF angle inhomogeneity, system delay, non-centered sampling windows, etc. In this section the PDF of the magnitude data is discussed.

To construct a magnitude image from the complex data, the magnitude is computed on a pixel-by-pixel base:

$$M_i = \sqrt{R_i^2 + I_i^2} \quad , \tag{3.2}$$

with M_i denoting the ith data point of the magnitude image. As root extraction is a nonlinear transformation, the PDF of the magnitude data is no longer expected to be Gaussian. In the next section, the proper PDF of the magnitude data is derived.

3.3.1 The Rice distribution

The PDF of magnitude data is found by transforming the joint PDF of the real and imaginary data, given in Eq. (3.1), into polar coordinates:

$$p(M, \varphi | A, \phi, \sigma) = \frac{1}{2\pi\sigma^2} e^{-\frac{(A\cos\phi - M\cos\varphi)^2}{2\sigma^2}} e^{-\frac{(A\sin\phi - M\sin\varphi)^2}{2\sigma^2}} M \quad , \tag{3.3}$$

where M is the Jacobian of the transformation. Integrating this expression over φ along with some rearrangements yields:

$$p_M(M | A, \phi, \sigma) = \frac{1}{2\pi\sigma^2} \int_0^{2\pi} e^{-\frac{A^2 + M^2 - 2AM\cos(\varphi - \phi)}{2\sigma^2}} M d\varphi \quad . \tag{3.4}$$

As integration is over a full cycle of the cosine, we can equivalently write:

$$p_M(M | A, \sigma) = \frac{M}{2\pi\sigma^2} e^{-\frac{A^2 + M^2}{2\sigma^2}} \int_0^{2\pi} e^{\frac{AM}{\sigma^2}\cos\varphi} d\varphi \quad . \tag{3.5}$$

The integral over φ is related to the integral representation of the 0th order modified Bessel function of the first kind:

$$I_0(z) = \frac{1}{2\pi} \int_0^{2\pi} e^{z\cos\varphi} d\varphi \quad . \tag{3.6}$$

This leads us to the PDF that characterizes magnitude data:

$$p_M(M | A, \sigma) = \frac{M}{\sigma^2} e^{-\frac{M^2 + A^2}{2\sigma^2}} I_0\left(\frac{AM}{\sigma^2}\right) \epsilon(M) \quad . \tag{3.7}$$

The unit step Heaviside function $\epsilon(.)$ is used to indicate that the expression for the PDF of M is valid for non-negative values of M only. The distribution is called the *Rice distribution* after S. O. Rice
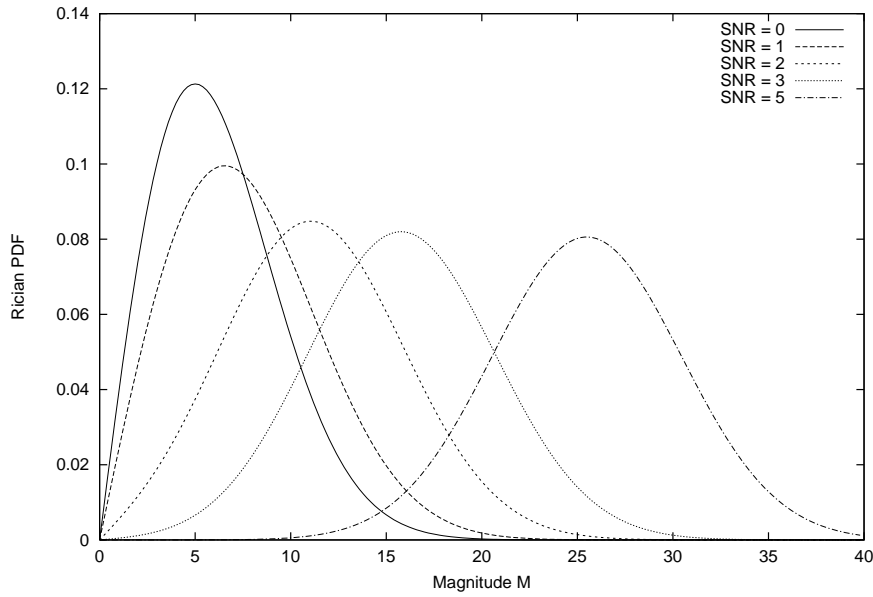
Figure 3.1: The Rice PDF as a function of the magnitude M, drawn for various values of the SNR where $\sigma = 5$. At SNR = 0, the distribution equals a Rayleigh distribution while at high SNR (SNR > 3) the Rice distribution approaches a Gauss distribution.

who derived it in the context of communication theory in 1944 [18].

The shape of the Rice distribution depends on the SNR, which is here defined as the ratio A/σ. Fig. 3.1 shows the Rice PDF as a function of the magnitude M for various values of the SNR. For low SNR, the Rice PDF tends to a Rayleigh distribution, which only depends on the noise variance σ^2:

$$p_M\left(M|\sigma\right) = \frac{M}{\sigma^2} e^{-\frac{M^2}{2\sigma^2}} \epsilon\left(M\right) \quad . \tag{3.8}$$

The Rayleigh PDF characterizes the random intensity distribution of the non-signal background area such as air. At high SNR, the Rice distribution approaches a Gauss distribution. The transition between the two limits of the Rice distribution can visually be appreciated in Fig. 3.1. For further discussion, the moments of the Rice PDF are required.

Moments of the Rice distribution

In general, the μth moment of a PDF p_M is defined as:

$$E\left[M^\nu\right] = \int_0^\infty M^\nu p_M(M)dM \quad . \tag{3.9}$$

For a Rice PDF, the moments can be analytically expressed as a function of the confluent hypergeometric function of the first kind, denoted by $_1F_1$ [24]:

$$E\left[M^\nu\right] = \left(2\sigma^2\right)^{\nu/2} \Gamma\left(1 + \frac{\nu}{2}\right) {}_1F_1\left[-\frac{\nu}{2}; 1; -\frac{A^2}{2\sigma^2}\right] \quad , \tag{3.10}$$

with Γ representing the Gamma function. The even moments of the Rice distribution (i.e., when ν is even) are simple polynomials. E.g:

$$E\left[M^2\right] = A^2 + 2\sigma^2 \tag{3.11}$$

$$E\left[M^4\right] = A^4 + 8\sigma^2 A^2 + 8\sigma^4 \quad . \tag{3.12}$$

The expressions for the odd moments are much more complex. However, the confluent hypergeometric function can be expressed in terms of the modified Bessel functions, from which an analytic expression of the odd moments can be derived. E.g:

$$E\left[M\right] = \sigma\sqrt{\frac{\pi}{2}}e^{-\frac{A^2}{4\sigma^2}}\left[\left(1+\frac{A^2}{2\sigma^2}\right)I_0\left(\frac{A^2}{4\sigma^2}\right)+\frac{A^2}{2\sigma^2}I_1\left(\frac{A^2}{4\sigma^2}\right)\right] \tag{3.13}$$

$$E\left[M^3\right] = \sigma^3\sqrt{\frac{\pi}{2}}e^{-\frac{A^2}{4\sigma^2}}\left[\left(3+3\frac{A^2}{\sigma^2}+\frac{A^4}{2\sigma^4}\right)I_0\left(\frac{A^2}{4\sigma^2}\right)+\left(2\frac{A^2}{\sigma^2}+\frac{A^4}{2\sigma^4}\right)I_1\left(\frac{A^2}{4\sigma^2}\right)\right] \quad . \tag{3.14}$$

For completeness, we also mention the general expression for the moments of the limits of the Rice distribution. For the Rayleigh distribution we have:

$$E\left[M^\nu\right] = (2\sigma^2)^{\nu/2}\Gamma\left(1+\frac{\nu}{2}\right) \quad . \tag{3.15}$$

For the Gauss PDF (i.e., the Rice PDF for SNR $\rightarrow \infty$), we have [25]:

$$E\left[M^\nu\right] = \sigma^{2(\nu-1)}\left[\frac{d^{\nu-1}}{dA^{\nu-1}}\left(Ae^{\frac{A^2}{2\sigma^2}}\right)\right]e^{-\frac{A^2}{2\sigma^2}} \quad . \tag{3.16}$$

3.3.2 The generalized Rice distribution

In this section, the generalized Rice distribution is discussed, which characterizes magnitude data that are computed from more than two Gauss distributed variables. These data are found in phased array magnitude MR images, where use is made of multiple receiver coils [26], and in phase contrast MR images [20].

Phase Contrast Magnetic Resonance (PCMR) imaging is widely used to detect flow. It is an enhancement procedure by which signal contributions from stationary spins are suppressed through posterior image processing. PCMR images can be computed in several ways [27]. One way is by acquiring a complex valued base image $\mathbf{S}^+$ with a flow encoding gradient applied in for example the positive X direction, followed by an identical acquisition of $\mathbf{S}^-$, where the flow encoding gradient is applied in the opposite direction. The complex base images $\mathbf{S}^+$ and $\mathbf{S}^-$ are assumed to be corrupted by Gauss distributed, zero mean noise $\mathbf{n}_r^\pm$ and $\mathbf{n}_i^\pm$ with variance σ_n^2, where r and i denote the real and imaginary image component, respectively. The goal of phase contrast image formation is to visualize the phase difference $\Delta\Phi$ associated with flow. The complex base images are given by:

$$\mathbf{S}^+ = Ce^{j(\Phi_0+\Delta\Phi)} + \mathbf{n}_r^+ + j\mathbf{n}_i^+ \tag{3.17}$$

$$\mathbf{S}^- = Ce^{j(\Phi_0-\Delta\Phi)} + \mathbf{n}_r^- + j\mathbf{n}_i^- \quad , \tag{3.18}$$

where Φ_0 is an unknown phase offset and $j = \sqrt{-1}$. In Eq. (3.17-3.18), it is assumed that the voxel magnitude C is identical in both base images.
The same flow encoding strategy can be employed to acquire two additional pairs of complex valued MR images, $\mathbf{S}_Y^\pm$ and $\mathbf{S}_Z^\pm$, where the flow encoding gradients are applied in the other two orthogonal

directions, Y and Z, respectively. Then, from the six complex valued MR images, the phase contrast magnitude image $\mathbf{S}_{CD}$ can be computed via complex difference calculation:

$$\|\mathbf{S}_{CD}\| = \sqrt{\left\|\mathbf{S}_X^+ - \mathbf{S}_X^-\right\|^2 + \left\|\mathbf{S}_Y^+ - \mathbf{S}_Y^-\right\|^2 + \left\|\mathbf{S}_Z^+ - \mathbf{S}_Z^-\right\|^2} \quad . \tag{3.19}$$

It is now easy to show that the PCMR pixel variable, denoted by M, can be written as:

$$M = \sqrt{\sum_{k=1}^{K} s_k^2} \quad , \tag{3.20}$$

with K denoting twice the number of orthogonal Cartesian directions in which flow is encoded. The set $\{s_k\}$ are independent Gauss distributed variables with variance $2\sigma_n^2$. Without loss of generality, the mean values $\{a_k\}$ of $\{s_k\}$ can be written as:

$$a_k = \begin{cases} 2C_k \sin(\Delta\Phi_k) & \text{for} \quad \text{odd} \\ 0 & \quad \text{even} \end{cases} k \text{ values.} \tag{3.21}$$

Hence, the deterministic signal component of the PCMR pixel variable is given by:

$$A = \sqrt{\sum_{k=1}^{K} a_k^2} \quad . \tag{3.22}$$

As PCMR data are derived from the square root of the sum of the squares of Gauss distributed variables, which is a non-linear transformation, the PCMR data are no longer expected to be Gauss distributed. In appendix A, the PDF of such a PCMR variable is shown to be a generalized Rice PDF, given by:

$$p_M(M) = \frac{M}{\sigma^2}\left(\frac{M}{A}\right)^{\frac{K}{2}-1} \exp\left(-\frac{M^2+A^2}{2\sigma^2}\right) I_{\frac{K}{2}-1}\left(\frac{MA}{\sigma^2}\right) \epsilon(M) \quad . \tag{3.23}$$

When $A \to 0$, the PDF of the magnitude PCMR variable becomes a generalized Rayleigh PDF:

$$p_M(M) = \frac{2M^{K-1}}{(\sigma\sqrt{2})^K \Gamma(K/2)} \exp\left(-\frac{M^2}{2\sigma^2}\right) \epsilon(M) \quad . \tag{3.24}$$

Fig. 3.2 shows the generalized Rice PDF for SNR $= 0$ and SNR $= 3$ and for $K = 2, 4$ and 6 and $\sigma = 5$. The general expression for the moments is given by:

$$E[M^\nu] = (2\sigma^2)^{\nu/2}\frac{\Gamma[(K+\nu)/2]}{\Gamma(K/2)} {}_1F_1\left(-\frac{\nu}{2}, \frac{K}{2}; -\frac{A^2}{2\sigma^2}\right) \quad . \tag{3.25}$$

Again, the even moments turn out to be simple polynomials:

$$E\left[M^2\right] = K\sigma^2 + A^2 \tag{3.26}$$

$$E\left[M^4\right] = K^2\sigma^4 + 2K\sigma^4 + 2A^2K\sigma^2 + 4A^2\sigma^2 + A^4 \quad . \tag{3.27}$$
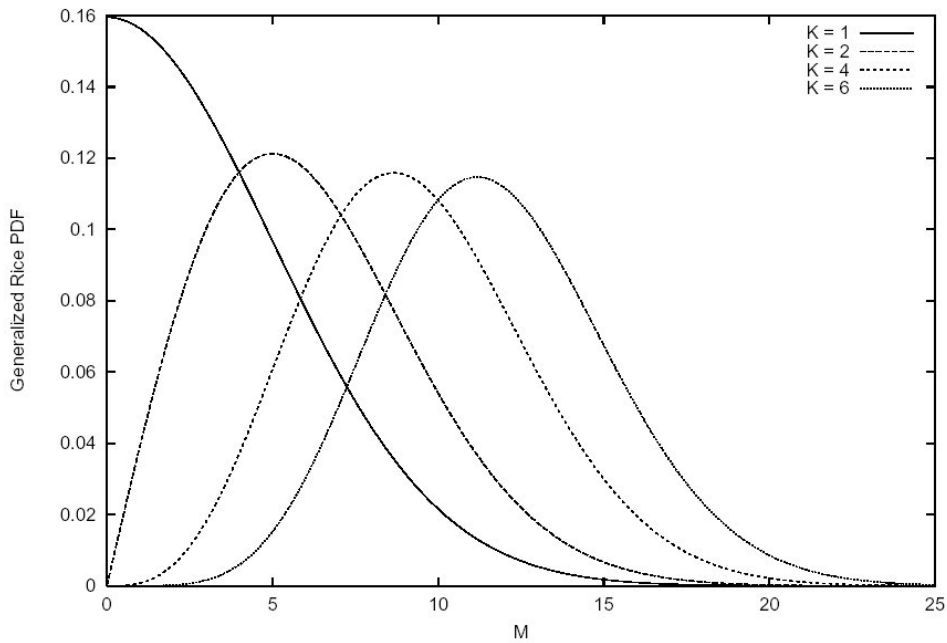
(a) SNR = 0
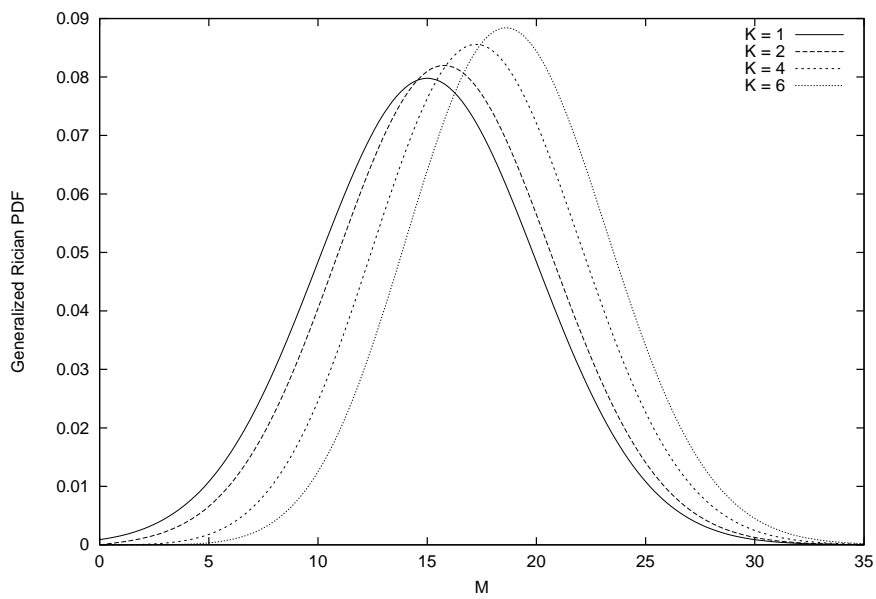
(b) SNR = 3

Figure 3.2: Plots of the generalized Rice PDF as a function of the magnitude M for $K = 1$, 2, 4 and 6 and with $\sigma = 5$.

3.4 PDF of phase data

Phase data, which are commonly used in flow imaging, are constructed from the real and imaginary data $\{(R_i, I_i)\}$ by calculating for each complex data point the arctangent of their ratio:

$$\Phi_i = \arctan\left(\frac{I_i}{R_i}\right) \quad . \tag{3.28}$$

As the arctangent is a nonlinear function, we again no longer expect the phase variables to be Gauss distributed. Indeed, the distribution of the phase deviation $\Delta\Phi$ from the true phase value is given by [28]:

$$p(\Delta\Phi) = \frac{1}{2\pi}e^{-A^2/2\sigma^2}\left[1 + \frac{A}{\sigma}\cos\Delta\Phi e^{A^2\cos^2\Delta\Phi/2\sigma^2}\int_{-\infty}^{\frac{A\cos\Delta\Phi}{\sigma}} e^{-x^2/2}dx\right] \quad . \tag{3.29}$$

Note that the distribution can be expressed solely in terms of the SNR, defined as A/σ. A graphical representation of the phase difference PDF as a function of the SNR is shown in Fig. 3.3.

Although the general expression for the distribution of $\Delta\Phi$ is complicated, the two limits of the SNR turn out to yield simple distributions. In regions where there is only noise, the SNR is zero and Eq. (3.29) reduces to a uniform PDF:

$$p(\Delta\Phi) = \begin{cases} \frac{1}{2\pi} & \text{if } -\pi < \Delta\Phi < \pi \\ 0 & \text{otherwise} \end{cases} \quad . \tag{3.30}$$

Stated in another way, the complex data, which only consist of noise, 'point in all directions' with the same probability. For large SNR, it is easy to see that the deviation in the phase angle, $\Delta\Phi$, due to noise will be small. In that case, Eq. (3.29) reduces to:

$$p(\Delta\Phi) = \frac{1}{\sqrt{2\pi}}\frac{A}{\sigma}\exp\left(-\frac{\Delta\Phi^2 A^2}{2\sigma^2}\right) \quad . \tag{3.31}$$

Thus, the phase noise $\Delta\Phi$ is governed by a Gauss distribution when SNR $\rightarrow \infty$.

The standard deviations for the phase noise can in general be calculated from Eq. (3.29). However, for the SNR limits, given in Eq. (3.30) and Eq. (3.31), it is given by:

$$\sigma_{\Delta\Phi} = \begin{cases} \pi/\sqrt{3} & \text{if } \text{SNR} = 0 \\ \sigma/A & \text{if } \text{SNR} \gg 1 \end{cases} \quad . \tag{3.32}$$
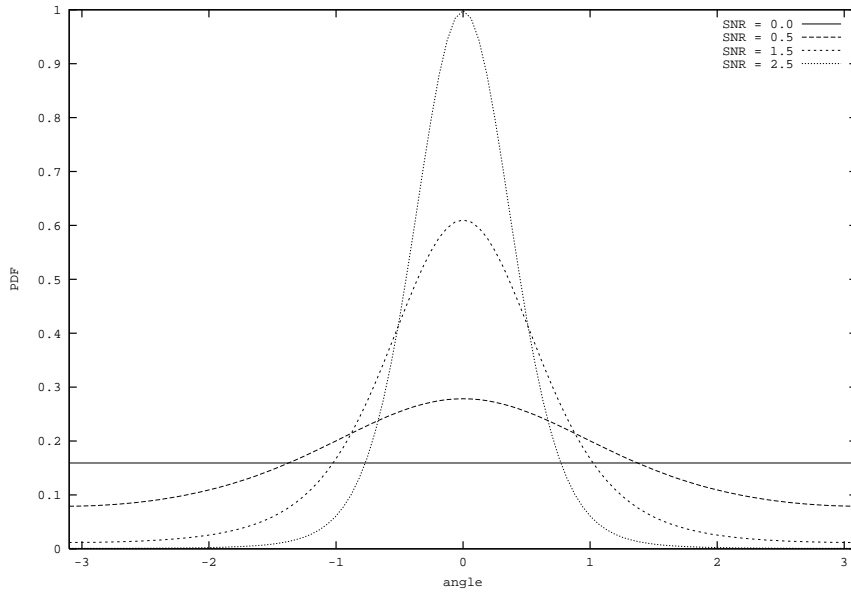
(a)
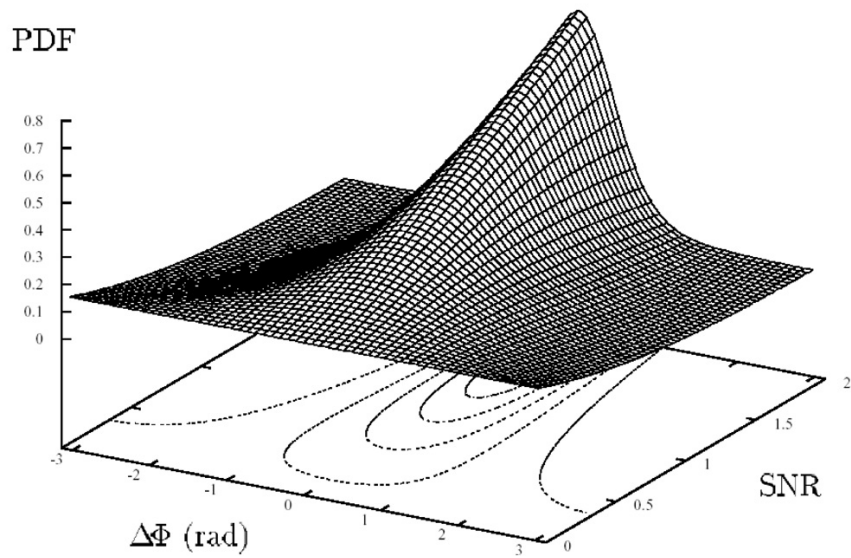
(b)

Figure 3.3: Plots of the phase error PDF as a function of the SNR.

Chapter 4

Noise estimation

4.1 Introduction

This chapter elaborates on noise estimation from Magnetic Resonance images. Emphasis is put on noise estimation from magnitude MR images.

Estimation of the image noise variance (NV) is important for several reasons. Firstly, it provides a measure of the image quality in terms of image detail: small signal variations tend to get lost in a sea of random variations when the noise variance increases. Furthermore, knowledge of the NV is useful in the analysis of the MR system: e.g., to test the performance of the MR system itself (receiver coil, preamplifier, etc.). Also, the NV is an important quality measure in functional MR imaging, where signal variations of the order of a few percent need to be detected. Finally, the NV value is often used as an input for image processing techniques such as image restoration [29, 30] or image filtering [31, 32].

In the image processing literature, most of the proposed methods to estimate the image noise variance assume Gauss or Poisson distributed noise [33, 34, 35, 36, 37, 38, 39]. However, as we saw in Chapter 3, magnitude MR data are no longer Gauss but Rice distributed. In this chapter, it is demonstrated how the properties of the Rice distribution can be exploited to estimate the image noise variance from magnitude MR data.

In MRI, the image NV is commonly estimated from a single magnitude MR image. Thereby, the NV is determined directly from a large uniform signal region or from non-signal regions [19, 40]. Although these methods may lead to useful NV estimates, large homogeneous regions are often hard to find, and, therefore, only a small amount of data points is available for estimation. Also, background data points sometimes suffer from systematic intensity variations.
To cover these disadvantages, methods were developed based on two acquisitions of the same image: the so-called double acquisition methods. Thereby, the amount of noise is for example computed by subtracting two acquisitions of the same object and calculating the standard deviation of the resulting image pixels [41]. Murphy et al. [42] elaborated this technique further and used a parallel rod test object for NV measurements from the signal and non-signal blocks. The double acquisition methods have that advantage over the single image techniques that they are relatively insensitive to structured noise such as ghosting, ringing and DC artefacts. However, a strict requirement is the perfect geometrical registration of the images. Beside geometrical registration, another problem may arise: due to small timing errors the raw data from one acquisition may be shifted relative to the other. After Fourier transformation, this results in additional phase variations of the complex data such that the above double acquisition NV estimation methods are no longer valid. To circumvent phase related problems, methods were proposed for the estimation of the image NV from magnitude MR images

[19, 28, 43].

This chapter is organized as follows. The first section elaborates on parameter estimation, where emphasis is put on Maximum Likelihood estimation. Next, conventional methods are discussed for the estimation of the image noise variance from magnitude MR images. Also, a new double acquisition noise NV estimation method is proposed, which exploits the properties of the Rice distribution. The proposed method is first tested on an artificial image as under controlled conditions, unforeseen errors, such as a bias, can be detected. Finally, the method is tested on various MR images.

4.2 Parameter estimation

4.2.1 Minimum Variance Bound

Suppose that the PDF of a variable x is determined by a parameter θ. Consider an unbiased estimator, t, of some function of θ, say $\tau(\theta)$. Then the lower bound on the variance of t is given by:

$$\mathrm{Var} = -\frac{\{\tau'(\theta)\}^2}{E\left(\frac{\partial^2 \log L}{\partial \theta^2}\right)} \quad . \tag{4.1}$$

This is the fundamental inequality for the variance of an estimator, often known as the Minimum Variance Bound (MVB) or the Cramér-Rao Lower Bound (CRLB).

4.2.2 Maximum Likelihood estimation

Suppose we have a number of N independent observations from the same distribution. The joint PDF of the observations, regarded as a function of a single unknown parameter θ, is called the Likelihood Function (LF) of the sample, and is written:

$$L(x|\theta) = p(x_1|\theta)p(x_2|\theta)\cdots p(x_N|\theta) \quad . \tag{4.2}$$

The Maximum Likelihood principle states that the estimator of θ, denoted by $\hat{\theta}$, should make the LF as large as possible within the admissible range of θ. That is, $\hat{\theta}$ should be chosen such that for any admissible value of θ

$$L(x|\hat{\theta}) \geq L(x|\theta) \quad . \tag{4.3}$$

If condition 4.3 applies, $\hat{\theta}$ is called the Maximum Likelihood (ML) estimator [44, 45].
Concerning the accuracy and precision of the ML estimator, it is known that, under very general conditions, the ML estimator is consistent and asymptotically most precise [46]:

- <u>Consistency</u>. Under very general conditions, ML estimators are consistent, i.e.,

$$\forall \epsilon \in \Re^+ \mid \left\{\Pr\left(|\hat{\theta} - \theta| < \epsilon\right) = 1 \quad \text{if} \quad N \to \infty\right\} \quad , \tag{4.4}$$

  with $\Re^+$ denoting the set of positive real numbers.

- <u>Asymptotic efficiency</u>. Under not too restrictive conditions, the variance-covariance matrix of the estimator $\hat{\theta}$ equals the CRLB, asymptotically. Hence, if the number of data points increases, the distribution of the ML estimator approaches the normal distribution with mean θ and variance equal to the Minimum Variance Bound (MVB), which is a lower bound on the variance of any unbiased estimator [47]. Furthermore, it is known that if there exists an unbiased estimator having the MVB as variance, it is the ML estimator [46].

4.3 Noise estimation

In the following, various methods for estimation of the noise standard deviation or the noise variance from magnitude MR data are discussed. Thereby, it will be assumed that the available data is governed by a generalized Rice distribution. The methods described below can also be applied to conventional Rice distributed magnitude MR data; that would be the case when $K = 2$.

4.3.1 Single image methods

The value of σ^2 can be estimated in many different ways. Usually, σ^2 is estimated from the background data points, where the deterministic signal is assumed to be zero, by exploiting the second moment of the generalized Rice PDF [19]:

$$\widehat{\sigma^2} = \frac{1}{KN} \sum_{i=1}^{N} M_i^2 \quad , \tag{4.5}$$

where N squared magnitude data points $\{M_i^2\}$ are averaged within any region that is assumed to have no signal, i.e., where $A = 0$. From Chapter 3, we learned that in such regions the magnitude data are governed by a generalized Rayleigh distribution:

$$p_M(M) = \frac{2M^{K-1}}{(2\sigma^2)^{K/2}\Gamma\left(\frac{K}{2}\right)} \exp\left(-\frac{M^2}{2\sigma^2}\right) \epsilon(M) \quad . \tag{4.6}$$

It can easily be shown that (4.5) is an unbiased estimator of σ^2 with a variance equal to σ^4/N. In addition, the estimator is identical to the Maximum Likelihood estimator. This can be seen as follows. The likelihood function L is given by:

$$L = \left(\sigma^2\right)^{-NK/2} \left(\prod_{i=1}^{N} \frac{2M_i^{K-1}}{2^{K/2}\Gamma\left(\frac{K}{2}\right)}\right) \prod_{i=1}^{N} \exp\left(-\frac{M_i^2}{2\sigma^2}\right) \quad , \tag{4.7}$$

where factors depending on σ^2 were grouped. Taking the logarithm and leaving only the terms that depend on σ^2, we have:

$$\log L \sim -\frac{NK}{2}\log\left(\sigma^2\right) - \frac{1}{2\sigma^2}\sum_{i=1}^{N} M_i^2 \quad . \tag{4.8}$$

Maximization of (4.8) requires the first order derivative of L, with respect to σ^2, to be zero:

$$\frac{\partial \log L}{\partial \sigma^2} = 0 \quad , \tag{4.9}$$

yielding the unbiased estimator given in Eq. (4.5). Its variance equals the Cramér-Rao lower bound (CRLB) for all N, given by:

$$\text{CRLB} = -\left(E\left[\frac{\partial^2 \log L}{\partial \left(\sigma^2\right)^2}\right]\right)^{-1} \tag{4.10}$$

$$= -\left(E\left[\frac{NK}{2\sigma^4} - \frac{1}{\sigma^6}\sum_{i=1}^{N} M_i^2\right]\right)^{-1} \tag{4.11}$$

$$= \frac{2\sigma^4}{NK} \quad . \tag{4.12}$$

One might be interested in the value of the standard deviation σ as well, e.g., to estimate the true SNR: A/σ. Simply taking the square root of the ML estimator of σ^2 yields an estimator of σ:

$$\hat{\sigma}_{ML} = \sqrt{\frac{1}{KN} \sum_{i=1}^{N} M_i^2} \quad . \tag{4.13}$$

This estimator is identical to the ML estimator of σ, as the square root operation has a single valued inverse (cfr. Invariance property of ML estimators [48]). Its variance is approximately equal to:

$$\text{Var}\,(\hat{\sigma}_{ML}) \simeq \frac{\sigma^2}{2NK} \quad , \tag{4.14}$$

which equals the CRLB. The estimator (4.13) is, however, biased because of the square root operation. Its expectation value is approximately equal to:

$$E\,[\hat{\sigma}_{ML}] \simeq \sigma \left(1 - \frac{1}{4NK}\right) \quad . \tag{4.15}$$

Notice that this means that it is possible to apply a bias correction. This however would increase the variance of the estimator.

Another commonly used estimator of σ can be found by exploiting the knowledge that the Rice PDF turns into a Rayleigh PDF in image regions with no signal. Since the mean value of the generalized Rayleigh PDF is given by

$$E[M] = \sqrt{2}\sigma \frac{\Gamma\,((K+1)/2)}{\Gamma\,(K/2)} \quad , \tag{4.16}$$

an unbiased estimator of σ is easily seen to be:

$$\hat{\sigma}_c = \frac{\Gamma\,(K/2)}{\Gamma\,((K+1)/2)} \frac{1}{\sqrt{2}N} \sum_{i=1}^{N} M_i \quad . \tag{4.17}$$

The variance of this estimator is given by

$$\text{Var}\,(\hat{\sigma}_c) = \frac{\sigma^2}{N} \left(\frac{K}{2} \left(\frac{\Gamma\,(K/2)}{\Gamma\,((K+1)\,/2)} \right)^2 - 1 \right) , \tag{4.18}$$

which is always larger than the CRLB. Next, we can compare both estimators of σ, described above, in terms of the Mean Squared Error (MSE), which is defined as [47]:

$$E\left[(\sigma - \hat{\sigma})^2\right] = \{E\,[\hat{\sigma}] - \sigma\}^2 + \text{Var}(\hat{\sigma}) \quad , \tag{4.19}$$

or explicitly for the conventional and the ML estimators:

$$\text{MSE}_{\hat{\sigma}_{ML}} \simeq \frac{\sigma^2}{N} \left(\frac{1}{2K} + \frac{1}{16NK^2} \right) \tag{4.20}$$

$$\text{MSE}_{\hat{\sigma}_c} = \frac{\sigma^2}{N} \left(\frac{K}{2} \left(\frac{\Gamma\,(K/2)}{\Gamma\,((K+1)\,/2)} \right)^2 - 1 \right) \tag{4.21}$$

To compare the conventional estimator with the ML estimator, an MSE ratio is defined as:

$$\text{MSE}_{\text{ratio}} = \frac{\text{MSE}_{\hat{\sigma}_c} - \text{MSE}_{\hat{\sigma}_{ML}}}{\text{MSE}_{\hat{\sigma}_{ML}}} \quad . \tag{4.22}$$

Note that the MSE ratio is independent of the noise variance. The MSE ratio, as a function of the number of data points, is shown in Fig. 4.1 for $K = 2, 4$ and 6. For large N, the MSE of the common estimator (4.17) is significantly larger than that of the ML estimator (4.13). The performance of the conventional estimator, compared to the ML estimator, is worst for conventional magnitude MR images, where $K = 2$.
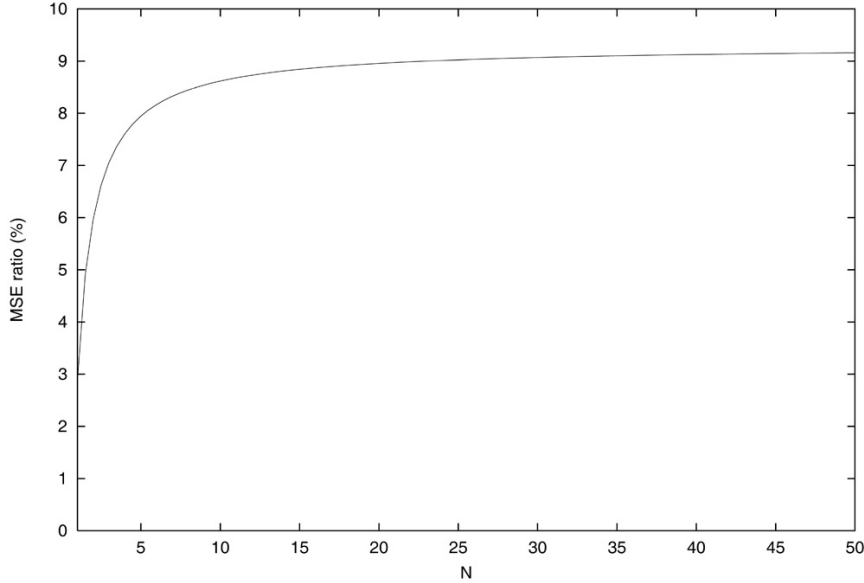
Figure 4.1: Performance comparison between the conventional and the ML estimator of the noise standard deviation: MSE ratio as a function of the number of data points N for $K = 2, 4$ and 6.

4.3.2 Double image method

When two conventional MR images ($K = 2$) are acquired under identical imaging conditions, one can solve σ^2 from two equations and two unknowns using the averaged and single images, since:

$$E\left[\langle M_s^2 \rangle\right] = \frac{1}{N}\sum_{n=1}^{N} A_n^2 + 2\sigma^2 \tag{4.23}$$

$$E\left[\langle M_a^2 \rangle\right] = \frac{1}{N}\sum_{n=1}^{N} A_n^2 + 2\left(\frac{\sigma}{\sqrt{2}}\right)^2 \quad , \tag{4.24}$$

where $\langle \rangle$ denotes a spatial average of the whole image. The subscripts s and a refer to the single and averaged images, respectively. From Eq. (4.24) and Eq. (4.23) an unbiased estimator of the noise variance is derived:

$$\widehat{\sigma^2} = \langle M_s^2 \rangle - \langle M_a^2 \rangle \quad . \tag{4.25}$$

This approach has the following advantages:

- it does not require any user interaction, as no background pixels need to be selected;

- it is insensitive to systematic errors, as long as these appear in both images. It is clear that, if this type of error appears in only one of the two images, none of the double acquisition methods yields the correct result;

- the precision of the noise variance estimator (4.25) is drastically increased, compared to the precision of the estimator given in (4.5), as all the data points are involved in the estimation;

- it is valid for any image signal-to-noise ratio.

An obvious disadvantage is the double acquisition itself. However, in MR acquisition schemes, it is common practice to acquire two or more images for averaging. Hence, those images may as well be used for the proposed noise quantization procedure, without additional acquisition time. In addition,

the images require proper geometrical registration, i.e., no movement of the object during acquisition is allowed.

4.4 Experiments and discussion

The performance of the noise variance estimation method was in a first phase tested on an artificial image: the 'Lena' image, well known in image processing. This was done as under controlled conditions, a possible bias should reveal, if present. The dimensions of the image were 128×128. From the Lena image, two independent Rice distributed images with variance σ^2 were generated. The proposed noise estimation method was tested for various values of σ^2. Simulation results (see Fig. 4.2) show a perfect linear behavior with unit slope of the estimated NV as a function of the true NV, demonstrating the accuracy of the method. Furthermore, the NV estimation was observed to be highly precise, owing to the fact that all image pixels were used in the estimation.

Next to the test images, the noise estimation method was applied to Magnetic Resonance images. The data were generated using an MR apparatus (SMIS, Surrey, England) with a horizontal bore of 8 cm, a main magnetic field strength of 7 Tesla, and a maximal gradient strength of 0.1 Tesla/m. In all experiments, a birdcage RF coil with a diameter of 32 mm was used. The method was tested using 2D Spin Echo (SE) as well as Gradient Echo (GE) sequences. The object imaged, was initially a vegetable (cucumber) and secondly an animal (head of a mouse). For each experiment, 20 images of size 256×128 were acquired with TR = 500 ms and TE = 30 ms. For each object, the number of averages (NA) was varied from 2 untill 32 with step 2. For each NA, 20 images were acquired, allowing 10 independent noise estimations from 2 images using Eq. (4.23-4.24). Only the mean value and standard deviation of the 10 NV estimates were retained.
No artefacts were observed in the images of the cucumber though small ringing and ghosting artefacts were present in the images of the mouse head. These, however, did not influence the NV estimations as they appeared in both images. The results of this experiment (for the mouse head) are shown in Fig. 4.3, where the inverse NV estimates are plotted as a function of the number of averages, along with their 95% confidence intervals. As can be observed from the figure, the results are in correspondence with the theory in that the inverse NV estimates increase linearly with the number of averages, with zero offset.

4.5 Conclusions

When it comes to estimation of the image noise variance, methods based on a double acquisition are far superior to single image techniques in terms of precision. However, existing double acquisition methods become useless when different phase variations are present in the two images. To overcome this problem, a noise variance estimation method has been proposed, based on two magnitude images. Under the condition of geometrical registration, the proposed noise variance estimator has been shown to be highly precise and accurate.
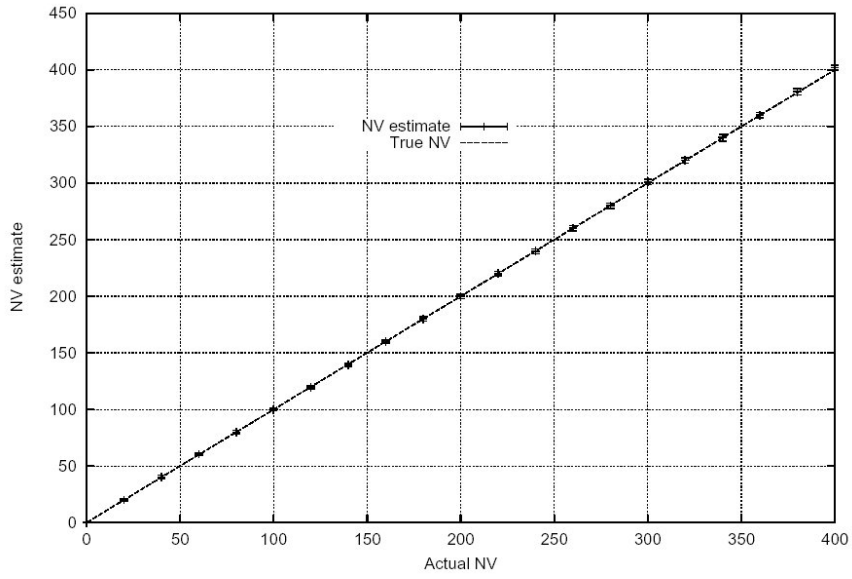
Figure 4.2: Estimation of the noise variance: simulation experiment.
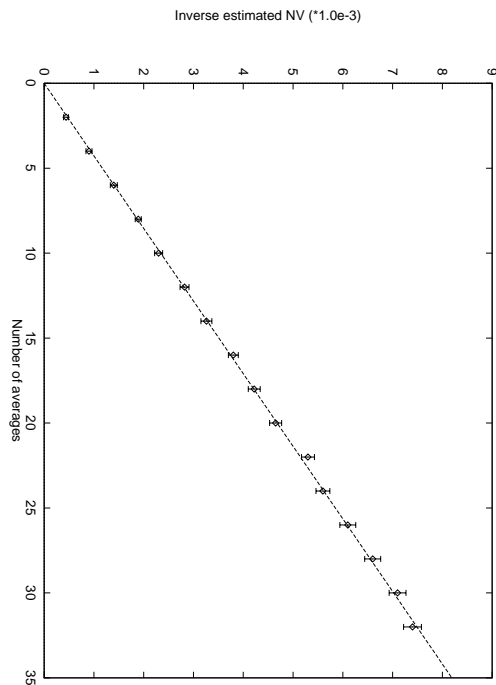
Figure 4.3: Estimation of the noise variance from magnitude MR images.

Chapter 5

Signal estimation

5.1 Introduction

In this chapter, the problem of parameter estimation from (generalized) Rice distributed data (e.g., magnitude MR images, magnitude PCMR images) is addressed. The properties of conventional estimation methods are discussed and compared to Maximum Likelihood estimation, which is known to yield optimal results asymptotically. In contrast to previously proposed methods, Maximum Likelihood estimation is demonstrated to be unbiased for high signal-to-noise ratio (SNR) and to yield physical relevant results for low SNR.

Conventional estimation techniques usually assume the data to be Gauss distributed. Whenever other PDF's come into play, e.g., in magnitude MR images, one still tends to use parameter estimation techniques that are based on Gauss distributed data [29, 31, 32]. The justification for this is that, when the signal-to-noise ratio (SNR) is high, the actual data PDF is very similar to a Gauss PDF. Also, Gauss PDF's have attractive computational properties.

With magnitude MR images, the Rice data PDF deviates significantly from a Gauss PDF when the SNR is low, leading to biased results. To reduce this bias, parameter estimation methods were proposed that exploit the knowledge of the Rice PDF [28, 49, 50, 51]. However, although the proposed estimators reduce the bias, they are not able to completely remove it. In this chapter, it is shown where the bias appears in the conventional estimation. In addition, a Maximum Likelihood (ML) estimator for (generalized) Rice distributed data is constructed. The performance of the conventional estimator is compared to that of the ML estimator [52]. This is motivated by the fact that, if there exists an unbiased estimator of which the variance attains the lowest possible value, it is obtained by the ML method.

5.2 Signal estimation from Rice distributed data

The problem, posed in this section, is the estimation of a deterministic signal component A from a region of interest (ROI), where A is assumed to be constant. The ROI consists of N Rice distributed data points $\{M_i\}$. First, conventional signal estimation methods are discussed. Afterwards, a signal estimation technique is proposed, based on Maximum Likelihood estimation. All methods described exploit the knowledge of the Rice PDF and its properties, given in Section 3.3.1.

5.2.1 Conventional approach

Conventional estimator

Commonly, Eq. (3.11) is exploited for the estimation of the underlying signal A. Thereby, $E\left[M^2\right]$ is estimated from a simple spatial average of the squared pixel values of the ROI [40, 42, 50, 51]:

$$E\widehat{[M^2]} = \langle M^2 \rangle = \frac{1}{N}\sum_{i=1}^{N} M_i^2 \quad . \tag{5.1}$$

Note that this estimator is unbiased since $E[\langle M^2 \rangle] = E[M^2] = A^2 + 2\sigma^2$. In the following, the noise variance σ^2 is currently assumed to be known. Consequently, an unbiased estimator of A^2 is given by:

$$\widehat{A^2} = \langle M^2 \rangle - 2\sigma^2 \quad . \tag{5.2}$$

Taking the square root of Eq. (5.2) gives the conventional estimator of A [40, 42, 50, 51]:

$$\hat{A}_c = \sqrt{\langle M^2 \rangle - 2\sigma^2} \quad . \tag{5.3}$$

Discussion

The parameter to be estimated is the signal A. Obviously, A is a priori known to be real valued and non-negative. However, this a priori knowledge has not been incorporated into the conventional estimation procedure. Consequently, the conventional estimator $\hat{A}_c$, given in Eq. (5.3), may reveal estimates that violate the a priori knowledge and are therefore physically meaningless. This is the case when $\widehat{A_c^2}$ becomes negative. Therefore, $\hat{A}_c$ can not be considered a useful estimator of A if the probability that $\widehat{A_c^2}$ is negative differs from zero significantly. The PDF of $\widehat{A_c^2}$ can be derived from Eq. (A.15):

$$p_y(y) = \frac{1}{2\sigma^2}\left(\frac{y}{(NA)^2}\right)^{\frac{N-1}{2}}\exp\left(-\frac{y+(NA)^2}{2\sigma^2}\right)I_{N-1}\left(\frac{\sqrt{y}(NA)}{\sigma^2}\right)\epsilon(y) \quad , \tag{5.4}$$

where y is now given by the sum of N real and N imaginary, independent, squared, Gauss distributed variables:

$$y = \sum_{i=1}^{2N} x_i^2 = \sum_{i=1}^{N} M_i^2 \quad . \tag{5.5}$$

The deterministic signal component of the variable y is given by NA^2. From Eq. (5.1) and Eq. (5.2), we see that $\widehat{A_c^2} = y/N - 2\sigma^2$, and with

$$p_{\widehat{A_c^2}}\left(\widehat{A_c^2}\right) = N p_y\left(N\left(\widehat{A_c^2} + 2\sigma^2\right)\right) \quad , \tag{5.6}$$

the PDF of $\widehat{A_c^2}$ becomes explicitly:

$$
\begin{aligned}
p_{\widehat{A_c^2}}\left(\widehat{A_c^2}\right) &= \frac{N}{2\sigma^2}\left(\frac{\widehat{A_c^2}+2\sigma^2}{A^2}\right)^{\frac{N-1}{2}}\exp\left(-N\frac{(\widehat{A_c^2}+2\sigma^2)+A^2}{2\sigma^2}\right) \\
&\times I_{N-1}\left(\frac{NA\sqrt{\widehat{A_c^2}+2\sigma^2}}{\sigma^2}\right)\epsilon\left(\widehat{A_c^2}+2\sigma^2\right) \quad .
\end{aligned}
\tag{5.7}
$$

In Fig. 5.1, the probability that $\widehat{A_c^2}$ is negative, $\Pr[\widehat{A_c^2} < 0]$, is drawn as a function of the local SNR for several values of N, where the local SNR is defined as:

$$\mathrm{SNR} = \frac{A}{\sigma} \quad . \tag{5.8}$$
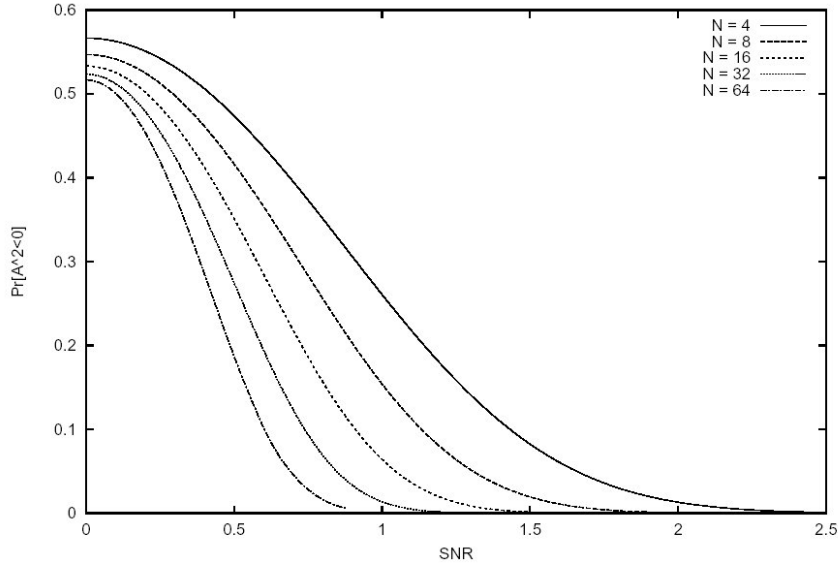
Figure 5.1: The probability $\Pr[\widehat{A_c^2} < 0]$ as a function of the SNR for various N.

From the figure, one can conclude that for low SNR $\hat{A}_c$ cannot be a valid estimator of A unless a large amount of data points is used for the estimation. Therefore, in practice, $\hat{A}_c$ will only be a useful estimator if the local SNR is high.

However, even if the condition of high SNR is met, the use of $\hat{A}_c$ as an estimator of A should still not be recommended, since the results obtained are biased because of the square root operation in Eq. (5.3). This becomes more clear when $E[\hat{A}_c]$ is expanded about the unbiased value A, yielding:

$$E\left[\hat{A}_c\right] \approx A\left(1 - \frac{\sigma^2}{2NA^2}\right) \quad . \tag{5.9}$$

Eq. (5.9) is valid for high SNR. The bias appears in the second term of Eq. (5.9). Note that it decreases with increasing SNR and increasing number of data points N. It is also remarked that the bias can be removed by jackknifing, but this requires a lot of computation [53].

5.2.2 Maximum Likelihood estimation

In this section, the ML method is introduced into the problem of the estimation of Rice distribution parameters. The ML estimator exploits the a priori knowledge of the data statistics in an optimal way.

ML estimator

From the joint PDF of a sample of N independent observations $\{M_i\}$, the likelihood function of the sample can be constructed:

$$L = \prod_{i=1}^{N} p\left(M_i | A\right) \quad , \tag{5.10}$$

where $p(M_i|A)$ is given in Eq. (3.7). The ML estimator can be constructed directly from the likelihood function L. Once the observations have been made and numbers can be substituted for $\{M_i\}$, L is a

function of the unknown parameter A only. The ML estimator of A is now defined as the estimator maximizing L, or equivalently $\log L$, as a function of A. Hence, using Eq. (3.7), it follows that:

$$\log L = \log \prod_{i=1}^{N} \frac{M_i}{\sigma^2} e^{-\frac{M_i^2 + A^2}{2\sigma^2}} I_0 \left(\frac{AM_i}{\sigma^2} \right) \tag{5.11}$$

$$= \sum_{i=1}^{N} \log \frac{M_i}{\sigma^2} - \sum_{i=1}^{N} \left(\frac{M_i^2 + A^2}{2\sigma^2} \right) + \sum_{i=1}^{N} \log I_0 \left(\frac{AM_i}{\sigma^2} \right) \quad, \tag{5.12}$$

or only as a function of A:

$$\log L \sim \sum_{i=1}^{N} \log I_0 \left(\frac{AM_i}{\sigma^2} \right) - \frac{NA^2}{2\sigma^2} \quad. \tag{5.13}$$

Since I_0 is symmetric about $A = 0$, L as well as $\log L$ are also symmetric about $A = 0$. The ML estimate is the global maximum of $\log L$:

$$\hat{A}_{ML} = \arg \left\{ \max_A \left(\log L \right) \right\} \quad. \tag{5.14}$$

Discussion

It is not possible to find the maximum of the $\log L$ function directly because the parameter A enters that function in a nonlinear way. Therefore, finding the maximum of the $\log L$ function will in general be an iterative numerical process.

In order to get some insight into the properties of the ML estimator, the structure of the $\log L$ function is now studied. This structure is established by the number and nature of the stationary points of the function. Stationary points are defined as points where the gradient vanishes, i.e., where

$$\frac{\partial}{\partial A} \log L = 0 \quad. \tag{5.15}$$

Substituting Eq. (5.13) into Eq. (5.15), we obtain:

$$\sum_{i=1}^{N} \frac{\partial}{\partial A} \log I_0 \left(\frac{AM_i}{\sigma^2} \right) - \frac{NA}{\sigma^2} = 0 \quad. \tag{5.16}$$

Given that the derivative of $I_0(z)$, with respect to z, equals $I_1(z)$, it follows:

$$\sum_{i=1}^{N} \frac{\frac{M_i}{\sigma^2} I_1 \left(\frac{AM_i}{\sigma^2} \right)}{I_0 \left(\frac{AM_i}{\sigma^2} \right)} - \frac{NA}{\sigma^2} = 0 \quad. \tag{5.17}$$

Hence, the condition for the stationary points becomes:

$$A = \frac{1}{N} \sum_{i=1}^{N} M_i \frac{I_1 \left(\frac{AM_i}{\sigma^2} \right)}{I_0 \left(\frac{AM_i}{\sigma^2} \right)} \quad. \tag{5.18}$$

It follows from Eq. (5.18) that $A = 0$ is a stationary point of $\log L$, independent of the particular data set. The nature of a stationary point is determined by the sign of the second order derivative of the function in that point. From this derivative, it follows whether a stationary point is a minimum or a maximum, and whether or not it is degenerate. From Eq. (5.13), the second order derivative of the $\log L$ function can be computed to yield:

$$\frac{\partial^2 \log L}{\partial A^2} = \sum_{i=1}^{N} \frac{M_i^2}{\sigma^4} \left[1 - \frac{\sigma^2}{AM_i} \frac{I_1 \left(\frac{AM_i}{\sigma^2} \right)}{I_0 \left(\frac{AM_i}{\sigma^2} \right)} - \frac{I_1^2 \left(\frac{AM_i}{\sigma^2} \right)}{I_0^2 \left(\frac{AM_i}{\sigma^2} \right)} \right] - \frac{N}{\sigma^2} \quad. \tag{5.19}$$

From the knowledge that [24]

$$I_\nu(z) \sim \left(\frac{z}{2}\right)^\nu \Gamma(\nu+1) \quad \text{when} \quad z \to 0 \tag{5.20}$$

it is easy to verify that $A = 0$ is a minimum of $\log L$ whenever:

$$\frac{1}{N}\sum_{i=1}^{N} M_i^2 > 2\sigma^2 \quad . \tag{5.21}$$

If this condition is met, the $\log L$ function will have two further stationary points, being maxima.

This can be seen by studying the possible structures of the $\log L$ function using catastrophe theory. Catastrophe theory is concerned with the structural change of a parametric function under influence of its parameters [54]. It tells us that a structural change of the function is always preceded by a degeneracy of one of its stationary points. In order to analyze such a structural change, the parametric function can be replaced by a Taylor expansion in the essential variables about the latter stationary point. The essential variables correspond to the directions in which degeneracy may occur. According to the catastrophe theory, the global structure of a parametric function, with only one essential variable, is completely set by its Taylor expansion up to the degree of which the coefficient cannot vanish under the influence of its parameters. The function studied here is the $\log L$ function as a function of A. Its parameters are the observations. Thus, the structural change of the $\log L$ function under the influence of the observations, has to be studied. The only essential variable is the signal parameter A. The stationary point that may become degenerate, is the point $A = 0$ (degeneracy occurs whenever (5.19) becomes equal to zero). If the $\log L$ function is Taylor expanded about the stationary point $A = 0$, we yield:

$$\log(L) = a + \frac{b}{2!}A^2 + \frac{c}{4!}A^4 + O\left(A^6\right) \quad , \tag{5.22}$$

with

$$a = \sum_{i=1}^{N} \frac{M_i^2}{\sigma^4}\left[1 - \frac{1}{2}\frac{\sigma^2}{M_i}\right] - \frac{N}{\sigma^2} \tag{5.23}$$

$$b = \sum_{i=1}^{N} \frac{M_i^2}{2\sigma^4} - \frac{N}{\sigma^2} \tag{5.24}$$

$$c = -\frac{3}{8}\sum_{i=1}^{N} \frac{M_i^2}{\sigma^8} \tag{5.25}$$

and $O(.)$ is the order symbol of Landau. Notice that, since the $\log L$ function is symmetric about $A = 0$, the odd terms are absent in Eq. (5.22). In order to investigate if the expansion up to the quartic term in Eq. (5.22) is sufficient, it has to be determined if the coefficients may change sign under influence of the observations. It is clear from Eq. (5.24) that the coefficient b may change sign. The coefficient c, however, will always be negative, independent of the particular set of observations. This means that the expansion (5.22) is sufficient to describe the possible structures of the $\log L$ function. Consequently, the study of the $\log L$ function as a function of the observations can be replaced by a study of the following quartic Taylor polynomial in the essential variable A:

$$\frac{b}{2!}A^2 + \frac{c}{4!}A^4 \quad , \tag{5.26}$$

where the term a has been omitted, since it does not influence the structure. The polynomial (5.26) is always stationary at $A = 0$. This will be a minimum, a degenerate maximum or a maximum when

b is positive, equal to zero, or negative, respectively. It follows directly from (5.26) that $\log L$ has two additional stationary points (being maxima) if b is positive, that is, if Eq. (5.21) is met. Notice that condition (5.21) is always met for noise free data. However, in practice, the data will be corrupted by noise, and for particular realizations of the noise, condition (5.21) may not be met. Then $A = 0$ will be a maximum. Moreover, if condition (5.21) is not met, b in (5.26) is negative and thus $\log L$ is convex, which means that $A = 0$ will be the only, and therefore, the global maximum of the $\log L$ function. This implies that, under the influence of noise, the two maxima and one minimum have merged into one single maximum at $A = 0$. This maximum then corresponds to the ML estimate. Note that, since condition (5.21) is identical to (and therefore can be replaced by) the condition $\widehat{A_c^2} > 0$, the probability that the ML estimate is found at $A = 0$, is equal to the probability that $\widehat{A_c^2} \leq 0$. This probability can be computed from the PDF, given in Eq. (5.7).

It follows from these considerations that, when the conventional estimator becomes invalid, the ML estimator will still yield physically relevant results.

5.2.3 Experiments and discussion

In order to compare the conventional estimator $\hat{A}_c$ to the ML estimator $\hat{A}_{ML}$ described above, an experiment was simulated in which the underlying signal was estimated from 16 Rice distributed data points ($N = 16$) as a function of the noise standard deviation σ. The true value of A was 100. The ML estimate was obtained by maximization of the likelihood function using Brent's algorithm [55]. This is an efficient one-dimensional optimization method based on parabolic interpolation, which converges rapidly as the likelihood function is well described by a parabola. The same experiment of determining $\hat{A}_c$ and $\hat{A}_{ML}$ was repeated 2.10^5 times, after which the averages $\langle \hat{A}_c \rangle$ and $\langle \hat{A}_{ML} \rangle$ were computed. The results are shown in Fig. 5.2, along with the 95% confidence intervals. From that figure, one can see that, at high SNR (SNR > 3), the ML estimator cannot be distinguished from an unbiased estimator, whereas the conventional estimator is clearly biased (Fig. 5.2(a)). As can also be observed, the experimental estimations $\hat{A}_c$ are in agreement with the expectation value of $\hat{A}_c$, predicted by Eq. (5.9).

At low SNR (SNR < 3) the use of $\hat{A}_c$ is no longer justified because the probability that $\hat{A}_c^2$ is negative becomes too high. As to still compare the ML estimator with the conventional one, we modified the conventional estimator in these adverse cases to yield the same estimate as the ML estimator: $\hat{A}_c = 0$. From Fig. 5.2(b), one can observe that both estimators become biased though the bias of the ML estimator is significantly smaller compared to the modified conventional estimator. The bias of the ML estimator has to do with the increasing probability of a structural change of the likelihood function. For low SNR, simulation experiments have shown the occurrence of both structures of $\log L$, described above, i.e., only one maximum or two maxima and one minimum. Some $\log L$ functions obtained from simulation experiments are shown in Fig. 5.3 for high and low SNR. Up to now, no other structures were observed. Remark that the occurrence of only one maximum at positive A-values makes the computational requirements for the maximization of the $\log L$ function very low.

In this section, the true value of the noise variance σ^2 was assumed to be known. In practice however, σ^2 needs to be estimated from the background or from homogeneous signal regions [19]. In general, the precision of the noise variance estimator is much better than that of the signal because often much more background data points are available. However, the accuracy of the σ^2 estimate is often influenced by systematic errors due to for example ghosting artefacts. As was discussed in Chapter 4, this problem can be tackled by acquiring two realizations of the same image [43]. However, if the noise variance estimate can not be prevented from degradation by systematic errors, σ^2 will automatically be over-estimated. An erroneous noise estimate will in turn influence the signal estimates. Simulation experiments however showed that, even with a 10% over- or under-estimated noise

variance value, ML estimation still yields significantly more accurate results compared to conventional estimation.

5.3   Signal estimation from PCMR data

From Chapter 3 we learned that phase contrast magnitude MR (PCMR) data are derived from the square root of the sum of the squares of a number of Gauss distributed variables, which is again a non-linear transformation. It has been shown that, when PCMR data are being used in quantitative analysis as an estimate of the underlying flow-related signal component magnitude, results are biased [20]. The bias is due to the contributions from inherent random noise, which is not Gauss distributed. Since the bias is not merely an additive component, it cannot be just subtracted out. To remove the bias, knowledge of the actual shape of the data probability density function (PDF) becomes essential. In this section, the full knowledge of the probability distribution of the phase contrast magnitude MR data is exploited for optimal estimation of the underlying signal.

It has to be noticed that, although this section focuses on complex difference processed images, the estimation techniques, derived in the remainder of this section, can, under certain conditions, also be applied to images obtained by phase difference processing. This has to do with the fact that for both methods, in the end, one has to estimate the underlying signal component from magnitude images of which the pixel variable M can be described by Eq. (3.20). The only difference is that, for phase difference processing, the dimension, or number of degrees of freedom K, directly equals the number of orthogonal Cartesian directions in which flow is encoded, whereas for complex difference processing the dimension K is twice this physical dimension [20].

5.3.1   Methods

In the following, it is assumed that an unknown deterministic signal component A needs to estimated from a number of PCMR pixel values of a region Ω where the signal component is assumed to be constant. Below, three signal estimation methods are discussed, two of which are based on spatial averaging, whereas one is based on Maximum Likelihood estimation.

Mean estimator

The most intuitive way of estimating the unknown signal component is through simple averaging of pixel values in the region Ω. Without a priori knowledge of the proper data PDF, this action would be justified as it is the optimal (i.e., Maximum Likelihood) estimation procedure if the data would be corrupted by Gauss distributed noise:

$$\hat{A}_m = \frac{1}{N} \sum_{i=1}^{N} M_i \quad . \tag{5.27}$$

The variance of this 'mean estimator' is given by:

$$\text{Var}\left(\hat{A}_m\right) = \frac{1}{N}\left(E\left[M_i^2\right] - E[M_i]^2\right) \quad . \tag{5.28}$$

However, as PCMR data are not Gauss distributed, it is clear that a huge bias would be introduced if the signal is estimated by averaging pixel values. The bias, relative to the true signal component A, is in general defined by:

$$\text{Relative bias} = \left|\frac{E[\hat{A}] - A}{A}\right| \times 100\% \quad , \tag{5.29}$$

where $E[\hat{A}]$ denotes the expectation value of the signal estimator $\hat{A}$. In the definition, the absolute value was taken as to make the relative bias logarithmically plottable. For the mean estimator (5.27), the expectation value $E[\hat{A}_m]$ is given by $E[M]$, because the average operator is an unbiased estimator of the expectation value. Hence, the relative bias of $\hat{A}_m$ can be computed from the expression for the moments of the generalized Rice PDF as given in Eq. (3.25) with $\nu = 1$. Note that it follows from Eq. (3.25) and Eq.(5.29) that the relative bias can be written solely in terms of the SNR, and is independent of the number of averaged pixel values N. Fig. 5.4 shows the relative bias of $\hat{A}_m$ as a function of the SNR for various values of K. From the figure, it is clear that the bias increases rapidly with decreasing SNR. Also, the bias increases with increasing number of flow encoding directions.

Modified RMS estimator

An easy way to reduce the bias is by exploiting the second moment of the generalized Rice distribution, as was given in Eq. (3.26). Indeed, an unbiased estimator of A^2 is given by:

$$\widehat{A^2} = \frac{1}{N}\sum_{i=1}^{N}M_i^2 - K\sigma^2 \quad . \tag{5.30}$$

The PDF of $\widehat{A^2}$ can be computed to yield:

$$p_{\widehat{A^2}}\left(\widehat{A^2}\right) = \frac{N}{2\sigma^2}\left(\frac{\widehat{A^2}+K\sigma^2}{A^2}\right)^{\frac{NK-2}{4}}\exp\left(-N\frac{\widehat{A^2}+K\sigma^2+A^2}{2\sigma^2}\right)$$

$$\times I_{\frac{NK}{2}-1}\left(\frac{\sqrt{\widehat{A^2}+K\sigma^2}NA}{\sigma^2}\right)\epsilon\left(\widehat{A^2}+K\sigma^2\right) \quad . \tag{5.31}$$

From the unbiased estimator of A^2, given in Eq. (5.30), a modified root mean square (RMS) estimator of A would be given by:

$$\hat{A}_{\text{rms}} = \sqrt{\frac{1}{N}\sum_{i=1}^{N}M_i^2 - K\sigma^2} \quad . \tag{5.32}$$

However, root extraction is a non-linear operation that makes the estimator $\hat{A}_{\text{rms}}$ biased. Also, the modified RMS estimator is only appropriate whenever the argument of the square root operator is non-negative. A possible, at first sight quite arbitrary, solution to this problem is to artificially put the estimator $\hat{A}_{\text{rms}}$ to zero whenever $\widehat{A^2}$ is negative:

$$\hat{A}_{\text{rms}} = \begin{cases} \sqrt{\widehat{A^2}} & \text{if} \quad \widehat{A^2} \geq 0 \\ 0 & \text{if} \quad \widehat{A^2} < 0 \quad . \end{cases} \tag{5.33}$$

The PDF of $\hat{A}_{\text{rms}}$ is then given by:

$$p_{\hat{A}_{\text{rms}}}\left(\hat{A}_{\text{rms}}\right) = \int_{-K\sigma^2}^{0}p_{\widehat{A^2}}(x)\,dx\ \delta\left(\hat{A}_{\text{rms}}\right) + \frac{N\hat{A}_{\text{rms}}}{\sigma^2}\left(\frac{\hat{A}_{\text{rms}}^2+K\sigma^2}{A^2}\right)^{\frac{NK-2}{4}}$$

$$\times \exp\left(-N\frac{\hat{A}_{\text{rms}}^2+K\sigma^2+A^2}{2\sigma^2}\right)I_{\frac{NK}{2}-1}\left(\frac{\sqrt{\hat{A}_{\text{rms}}^2+K\sigma^2}NA}{\sigma^2}\right)\epsilon\left(\hat{A}_{\text{rms}}\right) \quad , \tag{5.34}$$

where $\delta(.)$ denotes the Dirac delta function. Notice that the first term of Eq. (5.34) vanishes for high SNR. The bias of the modified estimator (5.33) can be computed from

$$E[\hat{A}_{\text{rms}}] = \int_0^\infty p_{\hat{A}_{\text{rms}}}(x)\,x dx \quad . \tag{5.35}$$

Fig. 5.5 shows the bias for various values of K and N. In general, the bias of the modified estimator is significantly smaller compared to the bias of the mean estimator. It should be noticed that the bias of the mean estimator turns out to be positively valued, whereas the bias of the modified RMS estimator has a negative sign. That, however, can not be observed from Fig. 5.5 or Fig. 5.4 due to the absolute value operator in Eq. (5.29). For both estimators, the bias increases with increasing number of flow encoding directions. However, in contrast to the mean estimator (5.27), the bias of the modified estimator (5.33) decreases with increasing N.

Maximum Likelihood estimator

In this section, the ML approach is clarified for the estimation of the unknown signal parameter A from a set of N independent magnitude PCMR data points $\{M_i\}$. The proposed technique consists of maximizing the likelihood function of N generalized Rice distributed data points, with respect to A. The likelihood function of N independent magnitude data points $\{M_i\}$ is given by:

$$L(\{M_i\}|A) = \prod_{i=1}^N p_M(M_i|A) \quad . \tag{5.36}$$

Then the Maximum Likelihood (ML) estimate of the PCMR signal A is the global maximum of L, or equivalently, the maximum of $\log(L)$, with respect to A:

$$\hat{A}_{ML} = \arg\left\{\max_A (\log L)\right\} \quad . \tag{5.37}$$

Leaving only the terms that depend on the variable A, we have explicitly:

$$\log(L) \sim -N\left(\frac{K}{2} - 1\right)\log A - \frac{NA^2}{2\sigma^2} + \sum_{i=1}^N \log I_{\frac{K}{2}-1}\left(\frac{M_i A}{\sigma^2}\right) \quad . \tag{5.38}$$

It can be shown that $\log(L)$ has only one maximum for positive A values. Hence, the computational requirements are very low. It can also be shown that the ML estimator yields the value zero whenever $\widehat{A^2}$, given by Eq. (5.30), is negative. This observation makes the modification of $\hat{A}_{\text{rms}}$, as described by Eq. (5.33), less arbitrary.

5.3.2 Experiments and discussion

It is already clear from Fig. 5.4 and 5.5 that the accuracy of the modified RMS estimator, described in Subsection 5.3.1, is an order of magnitude better than that of the mean estimator (5.27), though a significant bias still remains. As to compare the modified RMS estimator with the ML estimator, described in Subsection 5.3.1, a simulation experiment was set up. Thereby, K data points with deterministic signal component a_k were polluted with Gauss distributed zero mean noise with equal variance, after which a magnitude data point M was computed according to Eq. (3.20). The same procedure was repeated N times as to obtain N generalized Rice distributed magnitude data points. The deterministic signal component A of M, given in Eq. (3.22), was then estimated, once using the modified RMS estimator and once using the ML estimator. The data generation process and posterior

signal estimation was repeated 10^5 times as a function of the SNR, after which the average value and the 95% confidence interval was computed. Fig. 5.6 shows the signal estimation results for $K = 6$ and $N = 8$ as a function of the SNR. When the percentage for obtaining negative $\widehat{A^2}$ values was larger than 5%, the modified RMS estimator was regarded to be inappropriate. The SNR levels for this to occur were observed to be smaller than 1.5. For this reason, the modified RMS estimator was compared to the ML estimator only for SNR values higher than 1.5.

From Fig. 5.6 it is clear that the ML estimator is slightly but significantly more accurate than the modified RMS estimator. A similar behavior of the performance of the estimators was observed for all combinations of $K = 2$, 4, and 6 and $N = 4$, 8, and 16. The results also show that the precision, i.e., the standard deviation, of both estimators is approximately equal. It can also be seen that at high SNR the ML estimator cannot be distinguished from an unbiased estimator.

5.4 Combined signal and noise estimation

If non-signal regions are not available for noise variance estimation, the signal A and variance σ^2 have to be estimated simultaneously from the N available data points by maximizing the log-likelihood function with respect to A and σ^2:

$$\{\hat{A}_{ML}, \widehat{\sigma^2}_{ML}\} = \arg \left\{ \max_{A, \sigma^2} (\log L) \right\} \quad . \tag{5.39}$$

Although optimization of a two-dimensional function is more difficult, computational requirements were observed to be limited since the likelihood function was observed to yield only one maximum.

5.5 Conclusions

In this chapter, the problem of signal estimation from (generalized) Rice distributed magnitude MR data was discussed. It has been shown that the conventional estimator may not be used at low SNR unless a large amount of data points is used, which is often not available in practice. Even at high SNR the use of this estimator is still not recommended since it is biased.

As an alternative, the Maximum Likelihood estimator was proposed because it outperforms conventional estimators with respect to accuracy. The ML estimator yields physically relevant solutions for the whole range of SNR's. Moreover, it was shown that, unlike the conventional estimators, the ML estimator cannot be distinguished from an unbiased estimator at high SNR. Finally, the proposed Maximum Likelihood estimation technique can be applied to a region of interest as well as on a pixel-by-pixel basis.
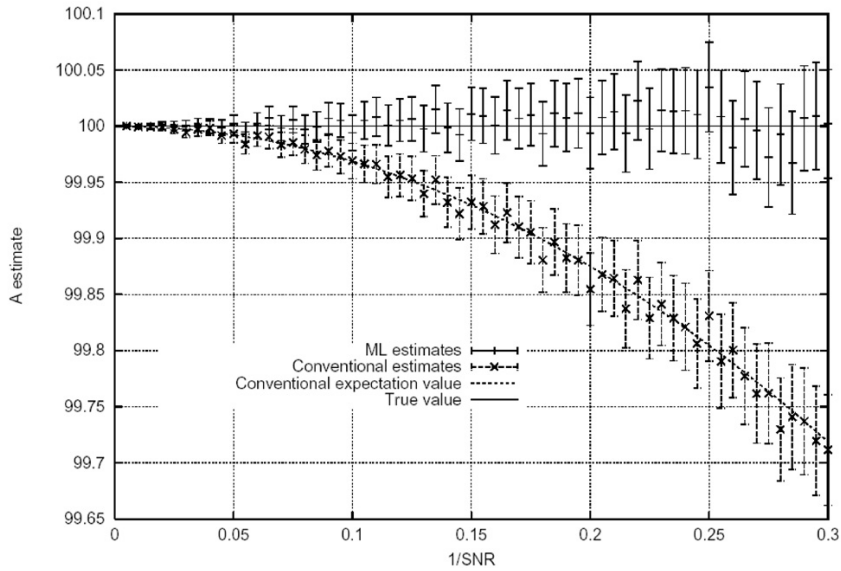
(a) High SNR
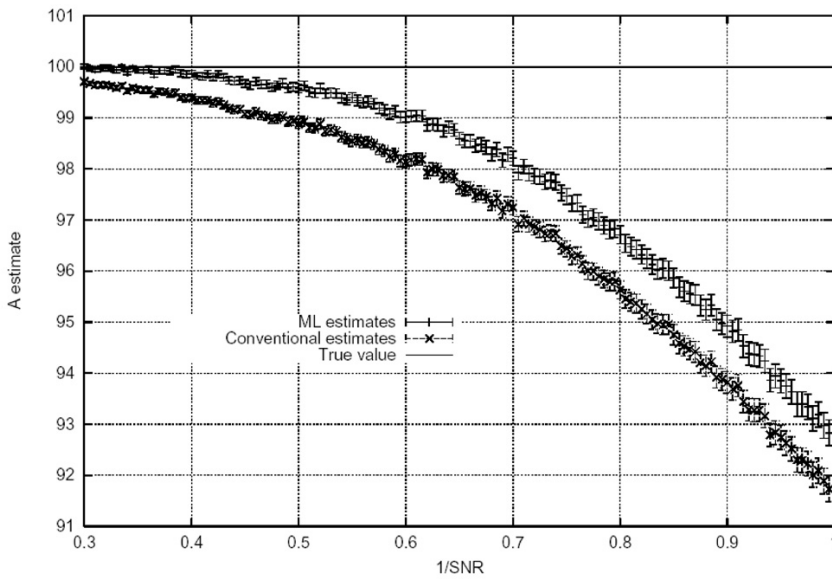
(b) Low SNR

Figure 5.2: Comparison between the conventional and the ML signal estimator for $N = 16$. Each point denotes the average of 10^5 estimations. The true signal component is $A = 100$. Also the 95% confidence interval is shown.
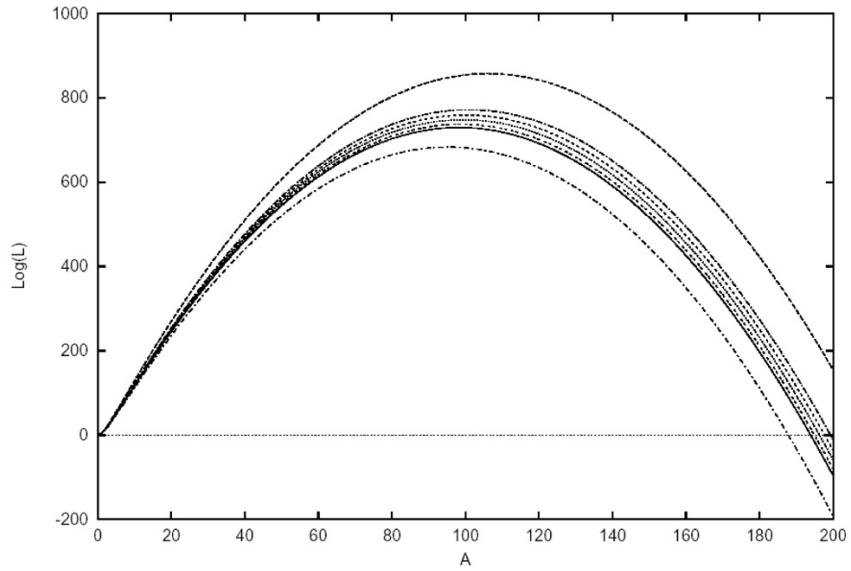
(a) SNR = 10
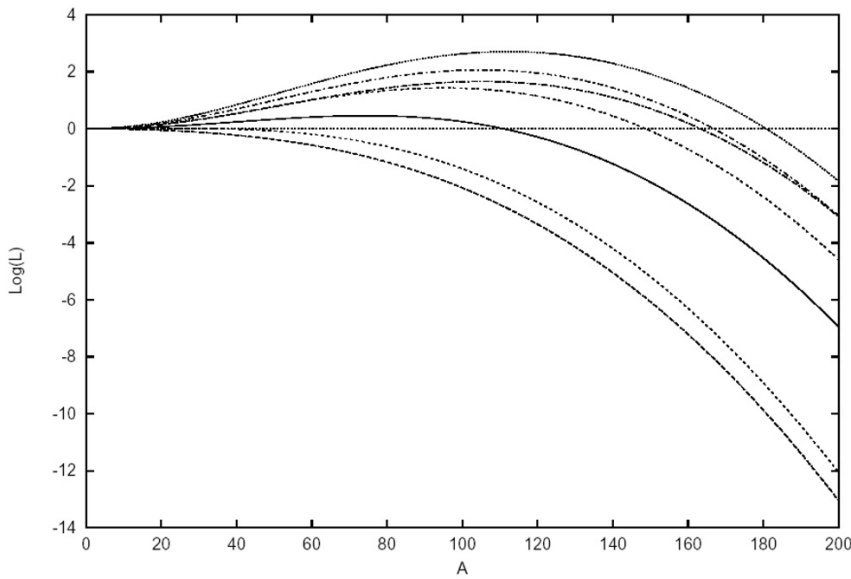
(b) SNR = 1

Figure 5.3: Likelihood functions for high (a) and low (b) SNR with $N = 16$. The different curves correspond to different realizations of the same experiment. The true value for A is 100.
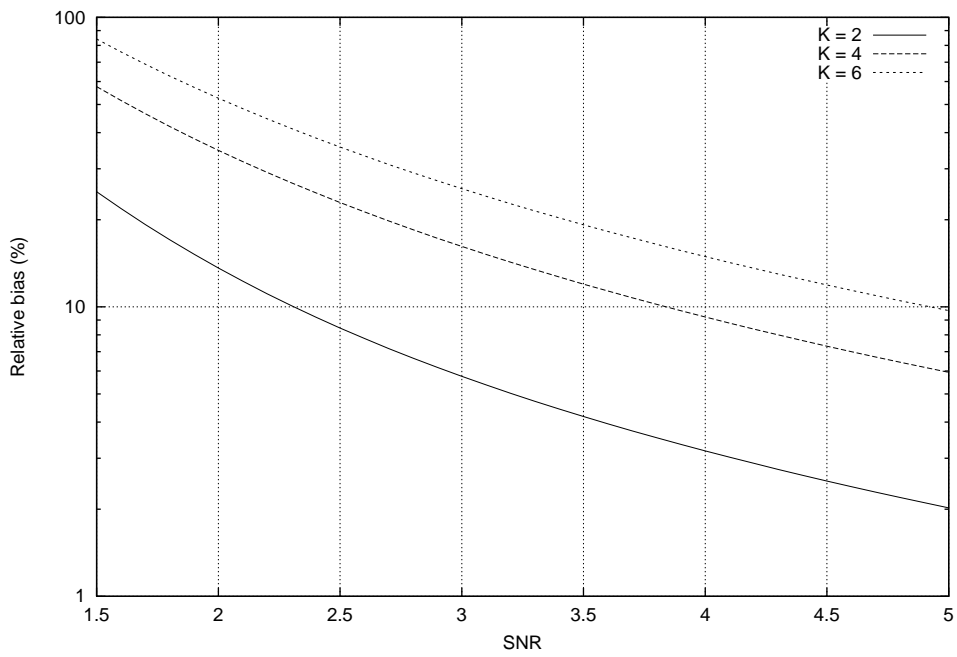
Figure 5.4: Relative bias of a simple spatial average estimator for $K = 2, 4$ and 6. The relative bias is independent of the number of averaged pixels N.
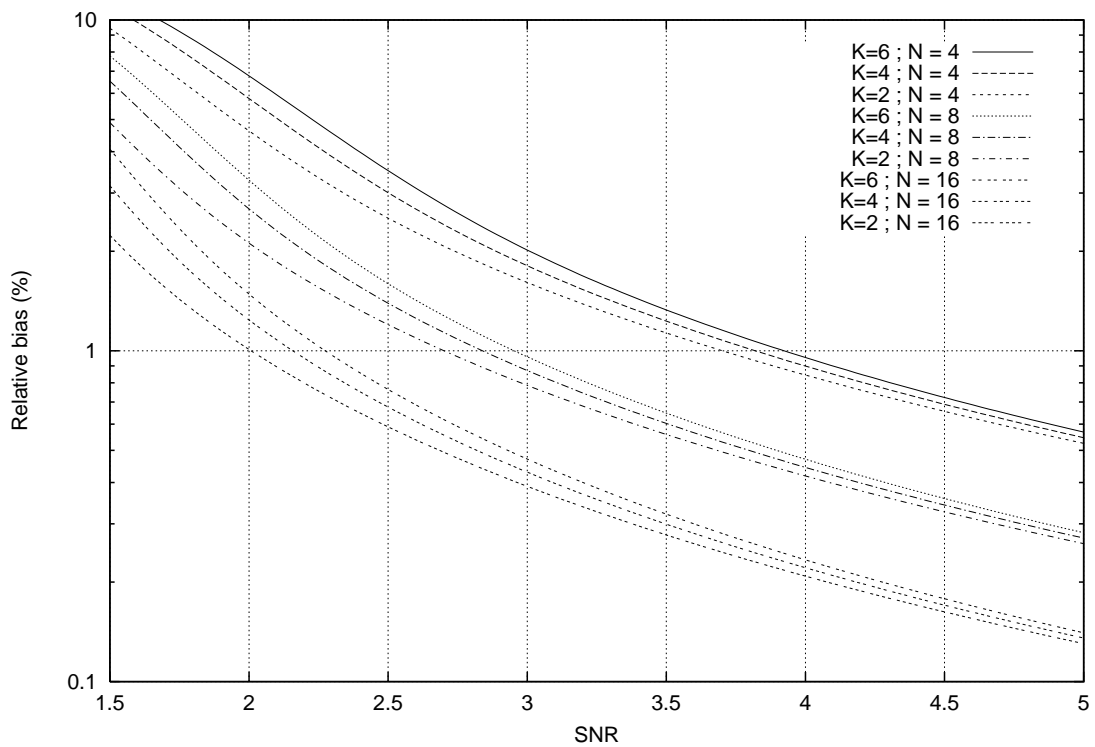
Figure 5.5: Relative bias of the estimator $\hat{A}_{\mathrm{rms}}$ for $K = 2, 4, 6$ and $N = 4, 8, 16$. The true value is $A = 100$.
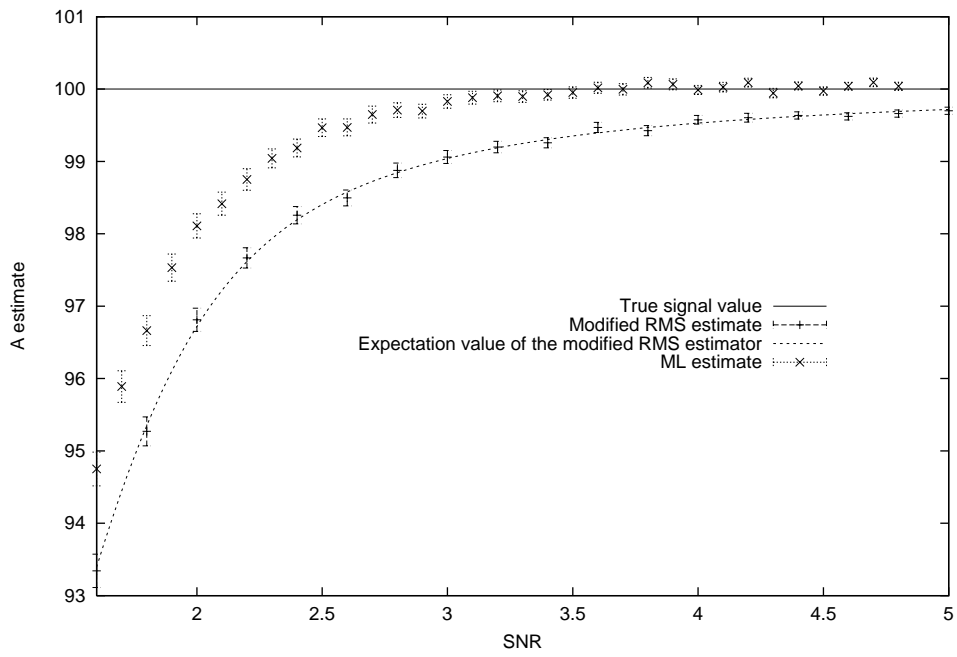
Figure 5.6: Comparison of the modified RMS estimator $\hat{A}_{\mathrm{rms}}$ with the ML estimator $\hat{A}_{ML}$ for $K = 6$ and $N = 8$. Each time, the average value of 10^5 signal estimates is given, along with the 95% confidence interval. The true value is $A = 100$. The expectation value of $\hat{A}_{\mathrm{rms}}$, according to Eq. (5.35), has also been shown.

Chapter 6

Application: T_1 and T_2 estimation

6.1 Introduction

Estimation of relaxation parameters has been a subject of considerable interest from the early years of MR imaging. Both the spin-lattice relaxation parameter T_1 and the spin-spin-relaxation parameter T_2 give useful information about the interaction with the local environment, and play a major role in the establishment of image contrast.

Conventional relaxation parameter estimation techniques, applied to magnitude MR images, are constructed from (weighted) least squares fitting procedures, which are only optimal in case of Gauss distributed data [56]. Magnitude MR data however are Rice distributed. Recently, a paper was published on the use of the Rice distribution in the problem of estimating T_2 maps from magnitude MR data [57]. In that paper, the problem of the data distribution was recognized, but parameter estimation was still performed assuming Gauss distributed, additive noise. The authors justified the use of least squares estimation by stating that the Rice distribution approaches a Gauss distribution at high signal-to-noise ratio (SNR). Although this is true, a bias is introduced in the estimation procedure, which becomes more pronounced with decreasing SNR.

In this chapter, a Maximum Likelihood (ML) estimation technique is proposed for optimal estimation of both the spin-lattice and the spin-spin relaxation time from a set of magnitude MR images. Again, this choice can be justified because an ML estimator is known to be consistent and asymptotically most precise [46]. In the construction of the ML estimator, full use is made of the Rice distribution. The validity of the proposed method is checked by simulation experiments. Finally, the method is tested on experimental MR data.

6.2 Method

6.2.1 Magnitude data PDF

As was discussed in Chapter 3, magnitude data are known to be Rice distributed:

$$p_M(M|f(\theta)) = \frac{M}{\sigma^2} \exp\left(-\frac{M^2 + f^2(\theta)}{2\sigma^2}\right) I_0\left(\frac{f(\theta)M}{\sigma^2}\right) \quad . \tag{6.1}$$

M denotes the pixel value of the magnitude image. Here, θ represents the parameter vector to be estimated of which the components are generally given by the pseudo proton density ρ, the spin-lattice or longitudinal relaxation constant T_1, and the spin-spin or transversal relaxation constant T_2: $\theta \equiv \{\rho, T_1, T_2\}$. $f(\theta)$ is a function of the parameter vector θ, which is completely determined by the MR imaging sequence applied. For example, for measurement of T_1 relaxation times, commonly a

snapshot FLASH imaging sequence is applied, where the magnetization relaxation can be described by:

$$f_i(\theta) = \rho \left(1 - 2 \exp \left(-\frac{t_i}{T_1} \right) \right) \quad , \tag{6.2}$$

where $f_i(\theta)$ denotes the deterministic signal component $f(\theta)$, at time t_i. If the transversal magnetization decay is mono-exponential and conventional spin-echo imaging is performed, the following model is known to be accurate:

$$f_i(\theta) = \rho \exp \left(-\frac{TE_i}{T_2} \right) \quad , \tag{6.3}$$

with TE_i denoting the echo time. The shape of the Rice distribution is strongly dependent on the signal-to-noise ratio (SNR), where the SNR is defined as the ratio $f(\theta)/\sigma$. It is therefore expected that, whenever parameter estimation techniques that were originally developed for Gauss distributed data are applied to magnitude data, systematic errors will be introduced due to the asymmetry of the Rice PDF, especially at low SNR.

6.2.2 Errors introduced in T_1 and T_2 estimation

For very high SNR, the expectation of the relaxation behavior is given by Eq. (6.3) and Eq. (6.2) because at high SNR, the value $f(\theta)$ equals the expectation value of the (approximately Gauss distributed) magnitude data. In general however, the expectation value of the magnitude data is given by:

$$E\left[M\right] = \sigma \sqrt{\frac{\pi}{2}} e^{-\frac{f(\theta)^2}{4\sigma^2}} \left[\left(1 + \frac{f(\theta)^2}{2\sigma^2} \right) I_0 \left(\frac{f(\theta)^2}{4\sigma^2} \right) + \frac{f(\theta)^2}{2\sigma^2} I_1 \left(\frac{f(\theta)^2}{4\sigma^2} \right) \right] \quad . \tag{6.4}$$

The deviation from $f(\theta)$ becomes more pronounced with decreasing SNR. In Fig. 6.1, the expectation value $E[M]$ for T_1 and T_2 relaxation is shown for various levels of the SNR. The true time constants were 100 ms and 2000 ms for T_1 and T_2, respectively, and 100 for the pseudo proton density ρ.

6.2.3 Maximum Likelihood estimation

In Subsection 4.2.2, the ML approach was clarified for the estimation of the unknown parameter vector $\theta \equiv \{\rho, T_2\}$ from a set of N independent magnitude data points $\{M_i\}$. The proposed technique consists of maximizing for each pixel position the likelihood function of N Rice distributed data points, with respect to θ. The likelihood function of N independent magnitude data points is given by (cfr. Eq. (5.12)):

$$L(\{M_i\}|\theta) \quad = \quad \prod_{i=1}^{N} p_M \left(M_i | \theta \right) \tag{6.5}$$

$$\stackrel{\text{Eq.(6.1)}}{=} \quad \frac{1}{\sigma^{2N}} \exp \left(-\sum_{i=1}^{N} \frac{M_i^2 + f_i(\theta)^2}{2\sigma^2} \right) \prod_{i=1}^{N} M_i I_0 \left(\frac{f_i(\theta) M_i}{\sigma^2} \right) \quad . \tag{6.6}$$

Maximization of L is equivalent to maximizing $\log L$ as log is a monotonic increasing function:

$$\log(L) = -N \log \sigma^2 - \sum_{i=1}^{N} \frac{M_i^2 + f_i(\theta)^2}{2\sigma^2} + \sum_{i=1}^{N} \log I_0 \left(\frac{f_i(\theta) M_i}{\sigma^2} \right) + \sum_{i=1}^{N} \log M_i \quad . \tag{6.7}$$

For maximization of $\log L$, only the terms that are a function of the unknown parameter vector θ are relevant:

$$\log(L) \sim \sum_{i=1}^{N} \left[\log I_0 \left(\frac{f_i(\theta) M_i}{\sigma^2} \right) - \frac{f_i(\theta)^2}{2\sigma^2} \right] \quad . \tag{6.8}$$

Then, the ML estimate for the parameter vector θ is the global maximum of $\log(L)$, with respect to θ:

$$\hat{\theta}_{ML} = \arg\left\{\max_{\theta}\left(\log L\right)\right\} \quad . \tag{6.9}$$

At high SNR, i.e., when the Rice distribution can be well approximated by a Gauss distribution, the likelihood function becomes:

$$L(\{M_i\}|\theta) = \left(\frac{1}{2\pi\sigma^2}\right)^{\frac{N}{2}} \prod_{i=1}^{N} \exp\left(-\frac{(M_i - f_i(\theta))^2}{2\sigma^2}\right) \quad . \tag{6.10}$$

In that case it is well known that maximization of $\log L$, with respect to the parameter θ, is equivalent to minimizing the quadratic distance E given by:

$$E = \sum_{i=1}^{N} [M_i - f_i(\theta)]^2 \quad . \tag{6.11}$$

This is also generally known as least squares (LS) fitting.

6.3   Experiments and Discussion

To validate the proposed estimation method, experiments were set up using simulated as well as experimental MR data. All data processing tasks were performed on a Hewlett Packard 720 workstation.

6.3.1   Simulation experiments

To show that a bias is introduced in the estimation, whenever Gauss instead of Rice distributed data are assumed, a simulation experiment was set up. Thereby, real valued data were corrupted with Gauss distributed noise. Zero mean imaginary data were also polluted with Gauss distributed noise with the same standard deviation, after which magnitude data were computed. From 16 Rice distributed data points, obtained in this way, θ was estimated, once using the conventional least squares (LS) fitting procedure and once using the proposed ML estimation technique. Here, θ was equal to (T_1, ρ) or (T_2, ρ) whether data decayed according to Eq. (6.2) or (6.3), respectively. The estimation was repeated 10^5 times for each value of the SNR, which is defined as:

$$\text{SNR} = \frac{\langle f(\theta)\rangle}{\sigma} \quad , \tag{6.12}$$

with $\langle f(\theta)\rangle$ the average signal value:

$$\langle f(\theta)\rangle = \frac{1}{N}\sum_{i=1}^{N} f_i(\theta) \quad , \tag{6.13}$$

where $f_i(\theta)$ is given by Eq. (6.2) or (6.3) for T_1- or T_2-estimation, respectively.

Fig. 6.2 shows the results for the estimation of $\theta \equiv \{\rho, T_1\}$. The true value for the pseudo proton density was $\rho = 100$ and 2000 ms for the T_1 relaxation constant. Each time, the average value was plotted as a function of the SNR. For clarity, the 95% confidence intervals are omitted: the relative error was of the order of 0.1% for both estimators. Fig. 6.2a and 6.2b show the results for the estimation of ρ and T_1, respectively. Both figures clearly demonstrate that the proposed ML technique is more accurate compared to conventional LS estimation. At high SNR, opposed to the outcomes of the LS estimator, no bias can be observed for the ML estimator. However, at low SNR (SNR < 5),

the ML estimator can be seen to become biased though the bias is still significantly smaller compared to that obtained by LS estimation.

Similar reasoning yields for simultaneous estimation of T_2 and ρ. Fig. 6.3a and 6.3b show the results for the estimation of ρ and T_2, respectively. The true value for the pseudo proton density was $\rho = 100$, and 100 ms for the T_2 relaxation constant. Also, in this case, ML estimation outperforms LS estimation in terms of accuracy.

The shape of the likelihood function is shown in Fig. 6.4 for T_1 (a) and T_2 (b) estimation. It was observed that the two-dimensional $\log L$ function has only one maximum, corresponding to the ML estimate of ρ and T_2. The general shape of the likelihood function did not change for different values of the true ρ and T_2 parameters, nor for various SNR. As a result, because of the occurrence of only one maximum of the likelihood function, optimization becomes a very simple task: it can be performed using standard optimization techniques with no risk of getting stuck into a local maximum. Each ML estimate was obtained by maximization of the likelihood function using the downhill simplex method of Nelder and Mead in two dimensions [55].

6.3.2 T_1-map estimation

Apart from the simulation experiments, tests were performed on experimental MR data. All data were generated on an MR apparatus (SMIS, Surrey, England) with a horizontal bore of 8 cm, a field strength of 7 Tesla, and a maximal gradient strength of 0.2 Tesla/m. A T_1-map was derived from a set of in vivo images of a mouse tumour (A high resolution coronal SE MR image of the tumour is shown in Fig. 6.5). T_1 tumour maps are useful to characterize the angiogenetic phase of tumours. Angiogenesis is the process in which blood vessels grow inside and towards the tumour. The tumour growth strongly depends on the surrounding vascular structures, as nutrients and oxygen are extracted from them. Hence, generation of new bloodvessels towards the tumour is essential for unlimited tumour growth. As a result, angiogenetics is also related to the metastasis and aggressiveness of the tumour. Various models describe the behaviour of T_1 maps over a time interval of 30 minutes before and after intravascular injection of a contrast agent, and this with respect to tumour permeability and tumour bloodvolume, which are both angiogenesis characteristics [58, 59, 60].

A number of 16 T_1-weighted in vivo images were obtained from a mouse tumour, using a snapshot FLASH pulse sequence with the following properties: $\text{FOV}_x = \text{FOV}_y = 20$ mm, slice thickness of 2 mm, TE-flash of 2.53 ms, TR-flash of 4.84 ms, 10 dummy scans prior to acquisition. Hence, the time between the inversion $180°$ RF pulse and the first acquisition was about 54 ms. The inversion time (TI) per image was about 310 ms. The acquisition matrix was 128×64, which was zero-filled to obtain 128×128 images. From 16 images the T_1 parameter was estimated on a pixel-by-pixel base, once using the conventional LS method and once using the proposed ML method. The resulting T_1-map obtained using the proposed ML method is shown in Fig. 6.6a. Fig. 6.6b shows the (intensity scaled) difference image between the map obtained from ML estimation, and the map obtained from LS estimation, as to visualize the bias reduction. The estimated T_1-values are shown for all but the background pixels.

6.3.3 T_2-map estimation

T_2 maps of a mouse brain were constructed in the context of studying the abnormalities in the ventricular system of hydrocephalic mice. The T_2 parameter is very sensitive to changes in water status, as they occur in development and in response to pathology. Among others, T_2 depends on the ratio of the free-to-bound water in tissue. Changes in this ratio often occur in degeneration processes, e.g., T_2 increases due to the formation of vasogenic edema following a stroke event.

To acquire T_2-weighted images, a 2D spin echo pulse sequence was used with TR $= 1500$ ms, $\text{FOV}_x =$

$\text{FOV}_y = 20$ mm, and slice thickness 1 mm. The acquisition matrix, 256×128, was zero filled to obtain a 256×256 image. From 6 magnitude images with echo times $\text{TE}_i = 20, 30, 40, 50, 60$ and 80 ms, respectively, the T_2 decay constant and the pseudo proton density were estimated for each pixel position. Two T_2-maps were obtained, one using the proposed ML estimation technique (shown in Fig. 6.7a) and one using LS estimation. Also the (intensity scaled) difference image was computed. As differences between the two maps could hardly be observed on a visual inspection, only the difference image is shown in Fig. 6.7b.

Finally, we remark that, in this experiment, a mono-exponentially decaying model was fitted to MR magnitude data points as to illustrate the consequences of not exploiting the proper data PDF. Obviously, as to make the imaging model more realistic, the model can be made arbitrarily complex by taking into account additional parameters. In that case, a higher dimensional likelihood function needs to be maximized.

6.4 Conclusions

The use of the ML estimator is highly recommended as, compared to conventional estimators, the results are in general superior with respect to accuracy. Finally, as the likelihood function was observed to yield only one maximum, the computational requirements for the maximization were very low.
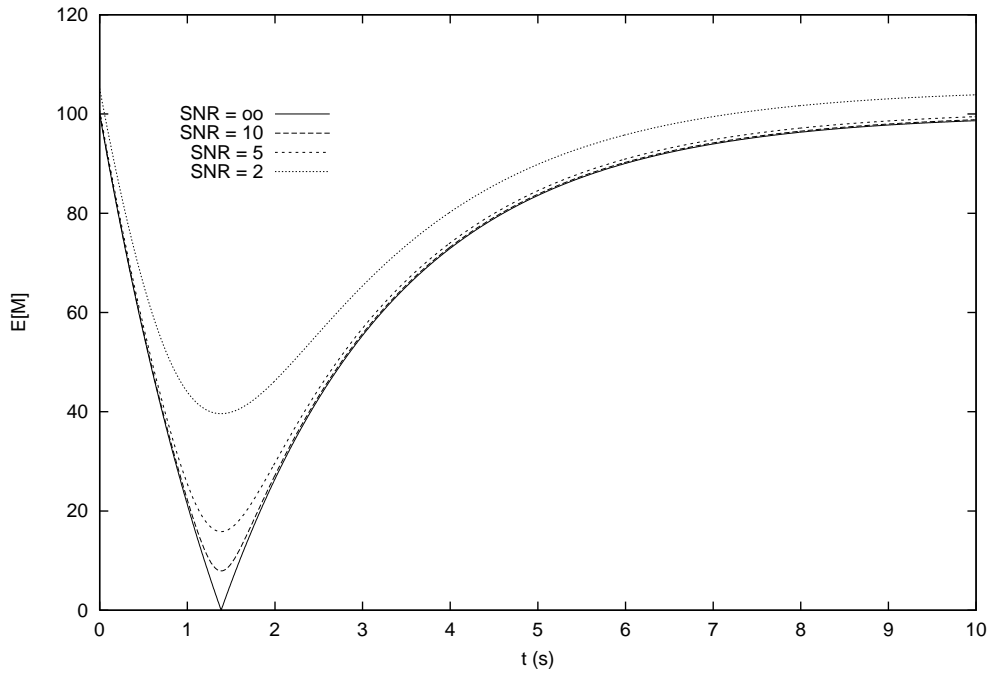
(a) Longitudinal relaxation with $T_1 = 2000$ ms
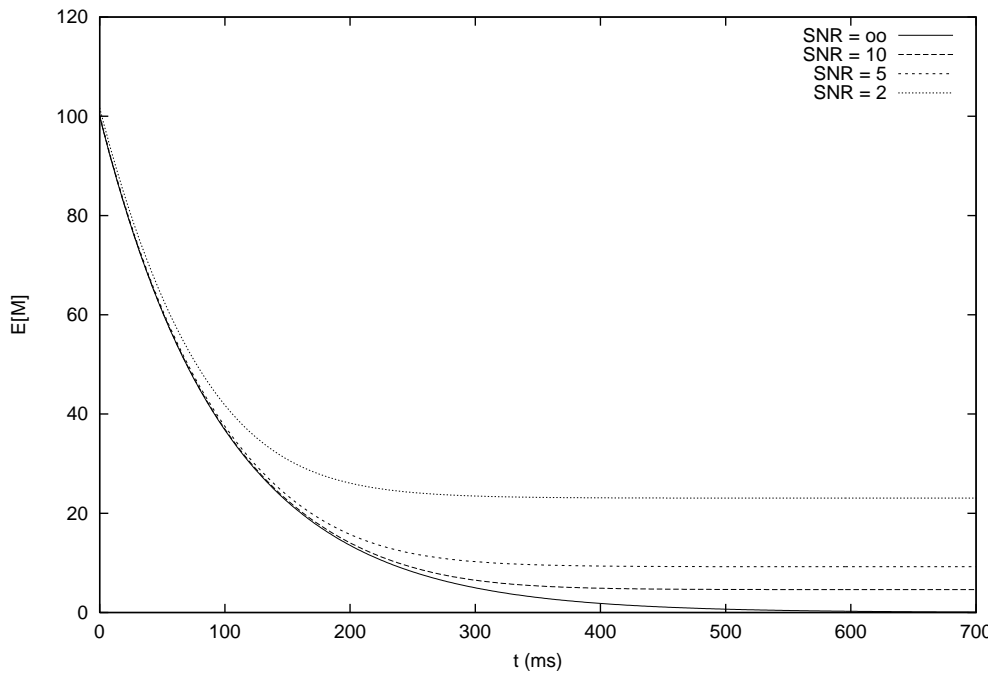
(b) Transversal relaxation with $T_2 = 100$ ms

Figure 6.1: Expectation values of magnitude MR signal for T_1 and T_2 relaxation as a function of time for various values of the SNR.
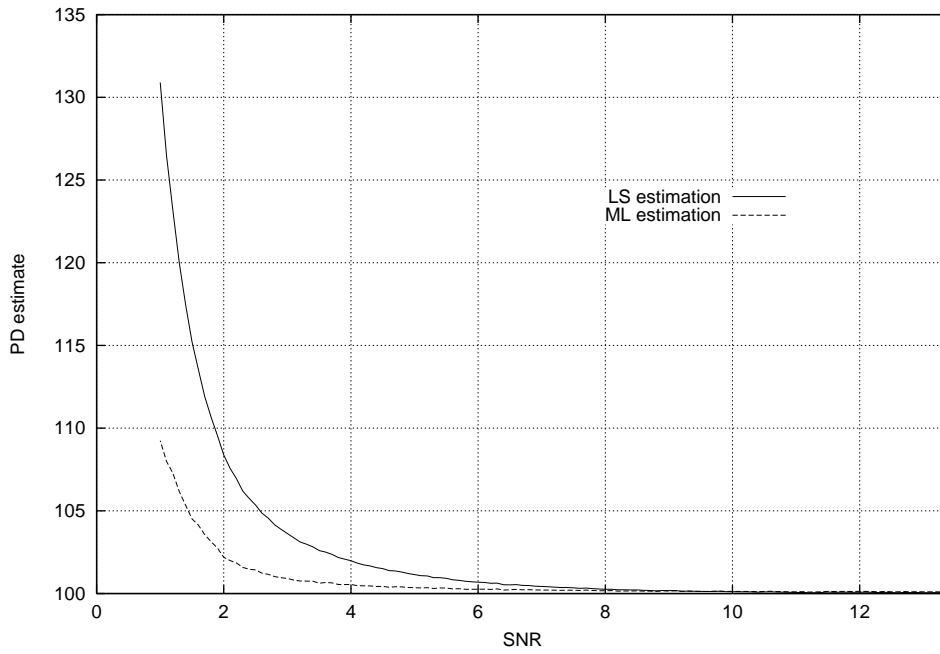
(a) ρ estimation
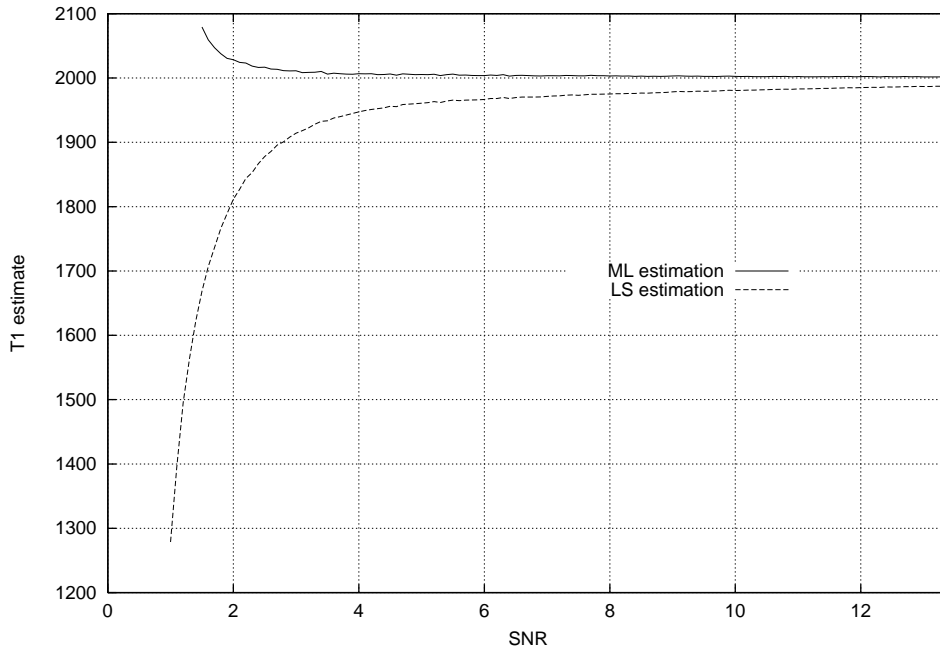
(b) T_1 estimation

Figure 6.2: Simulation experiment: simultaneous ρ and T_1 estimation as a function of the SNR. The true values are $\rho = 100$ and $T_1 = 2000$ ms.
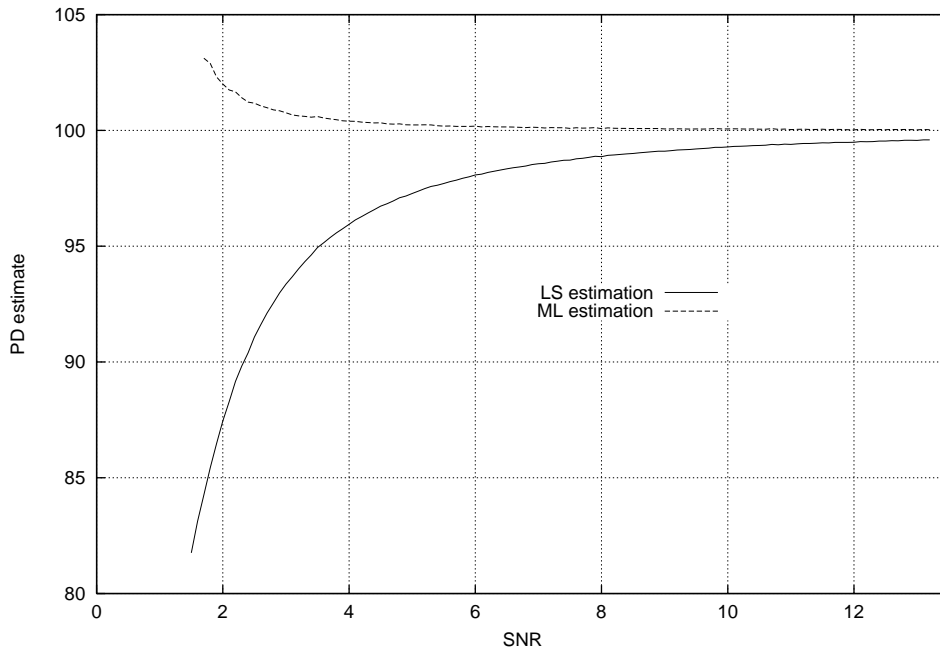
(a) ρ estimation
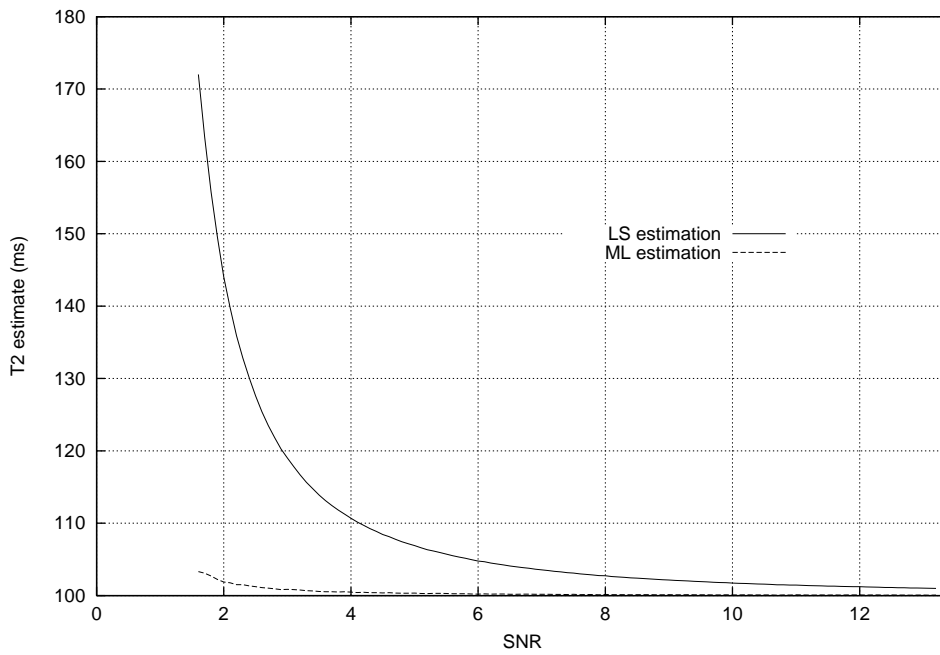
(b) T_2 estimation

Figure 6.3: Simulation experiment: simultaneous ρ and T_2 estimation from magnitude MR data as a function of the SNR. The true values are $\rho = 100$ and $T_2 = 100$ ms.

(a) (ρ, T_1) estimation
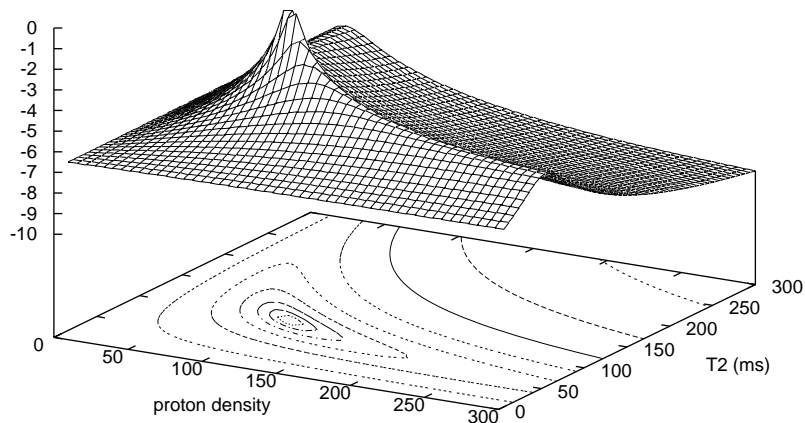
(b) (ρ, T_2) estimation

Figure 6.4: Shape of the $\log L$ function as a function of the pseudo proton density and T_1 (a) or T_2 (b).
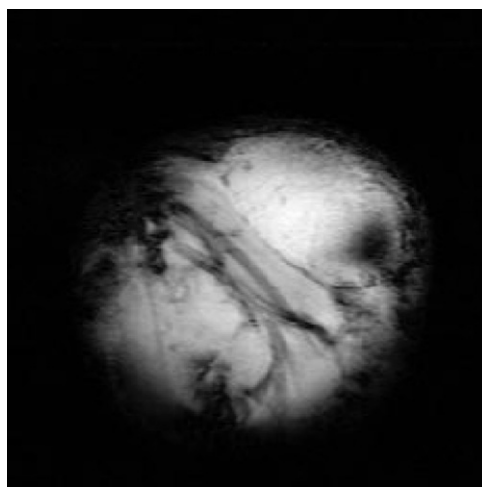
Figure 6.5: High resolution MR image of the a mouse tumour.
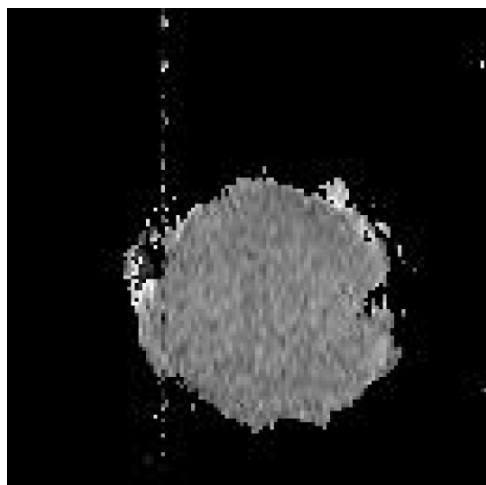
(a) T_1 map using ML
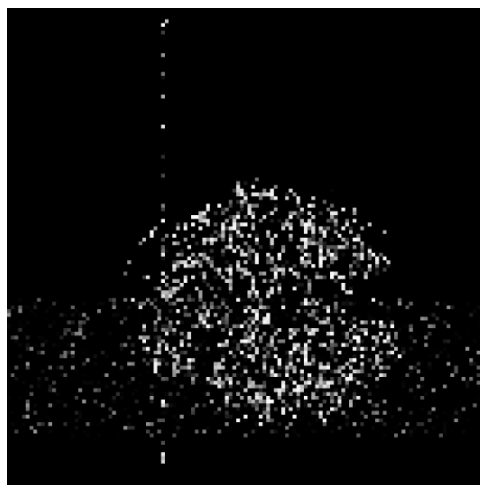
(b) Estimation difference map

Figure 6.6: T_1 maps of a mouse tumour.
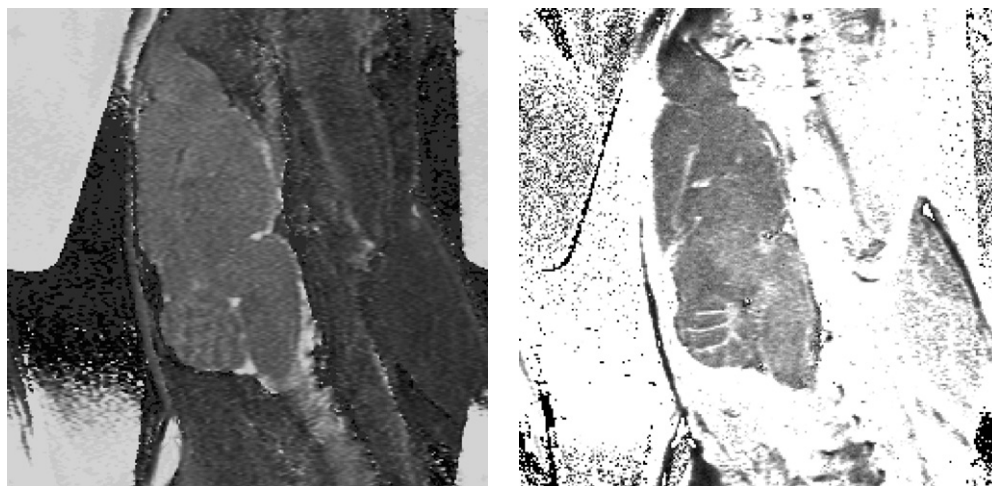
(a) T_2 map using ML   (b) Estimation difference map

Figure 6.7: T_2 maps of the mouse brain.

Chapter 7

SNR estimation

7.1 Introduction

This chapter deals with the estimation of the image signal-to-noise ratio (SNR). Conventional estimation methods are discussed and a new one is proposed.

Like the image noise variance, image SNR also provides a measure for the image quality in terms of image details. Also, besides testing different system parameters such as main magnetic field, homogeneity or DC offset between the real and imaginary signal components, the SNR can be used to check the performance of the MR system itself. Because the MR signal, and hence the SNR, strongly depends on the field homogeneity, the shape of the radio frequency (RF) pulses, the stability of the RF amplifiers, etc., estimation of the SNR is a useful tool in the analysis of the MR system. In the following, conventional methods for SNR estimation are described and a new method is proposed [61].

7.1.1 Single image methods

To determine the image SNR, it is standard to image a phantom object with a set imaging protocol for routine control. Protocols have been proposed by Sano [41], and Price et al. [62]. The resulting image consists of an area of uniform signal in an area of background noise. If the signal is uncorrupted by structured noise, the SNR is obtained by measuring the mean signal and standard deviation (characterizing the random noise) from a region of interest (ROI), within the area of the test object of the image.

If structured noise is present in the image, the noise standard deviation will be over-estimated, producing an erroneous low SNR. In addition, the above method of measuring the standard deviation in the signal area is badly affected by signal non-uniformity and ghosting artefacts, which are often present in MR images. This has stimulated several authors to propose others methods of noise estimation.

To avoid problems due to signal non-uniformity, several authors focussed on estimating the noise from the background of the images. Henkelman [19, 63] briefly discussed the problems of how to obtain an estimate of the noise from an ROI and presented the correction factor necessary if the ROI is placed in the background. The correction factor agrees with the one derived by Edelstein et al. [64] in the application of Rayleigh statistics to MRI. Unfortunately, this method also has many difficulties due to the presence of ghost artefacts in the phase encoded direction. These problems make the positioning of an ROI in the background noise crucial and require a good understanding of MRI and its artefacts. The positioning of ROI's within the signal and background regions was discussed in detail by Kaufman et al. [40]. To overcome these problems, one can use multiple realizations of the same image instead of one single image for SNR estimation. At present, these methods are generally preferred for SNR estimation.

7.1.2 The NEMA standard

The National Electrical Manufacturers Association (NEMA) is the largest trade association in the United States for companies that manufacture products used in generation, transmission, distribution, control ,and end use of electricity. NEMA is the leading developer of voluntary industry standards. The magnetic resonance section of NEMA's Diagnostic Imaging and Therapy Systems Division is developing performance standards for clinical MR systems. One of NEMA's performance standards, developed by R. M. Sano in 1988 [41], describes an SNR measure for the combined acquisition and reconstruction system, as used for imaging of humans:

- Acquisition: An NMR signal producing volume of a solution containing a spin density of about 20% of that of water is placed in the imaging volume. The solution must produce a coil loading equivalent to a 70 kg to 80 kg human, with relaxation characteristics of $T_1 < 1200$ ms and $T_2 > 50$ ms at operating field strength. Two identical single slice, transverse, SE, first echo images i_1 and i_2 are acquired at the isocenter of the phantom object with a $TR \leq 3T_1$ and TE within a clinically selectable range, a slice thickness smaller than 10 mm, and with less than 5 minutes time lapsed between the acquisitions.

- SNR estimation: The SNR is calculated by first determining the mean value of the first image: $\langle i_1 \rangle$. Then the second image is subtracted from the first image, pixel by pixel, and the standard deviation σ_n of the resulting image is computed:

$$\sigma_n^2 = \frac{1}{N^2 - 1} \sum_{\vec{r}} \left[i_1(\vec{r}) - i_2(\vec{r}) \right]^2 \quad , \tag{7.1}$$

where N^2 denotes the total number of image pixels, and $\vec{r}$ is the position vector. Finally, the SNR is the ratio of $\langle i_1 \rangle$ and σ_n, multiplied by the square root of two:

$$SNR = \sqrt{2} \frac{\langle i_1 \rangle}{\sigma_n} \quad . \tag{7.2}$$

The factor $\sqrt{2}$ is required as σ_n is derived from the subtraction image, rather than from one of the original images. Note that the method requires a perfect geometrical registration of the images.

At present, this is the standard procedure for SNR estimation in diagnostic MRI.

7.2 Cross correlation method

In this section, a new technique to estimate the SNR from MR images is proposed. The image SNR is estimated using the correlation function of two independent acquisitions of an image. To test the performance of the estimation, theoretically expected curves are fitted to the SNR measurement data. It is shown that the correlation technique can be implemented in a highly efficient way in almost any acquisition procedure of an MR imaging system.

In 1971, it has been suggested by Lenz that a cross-correlation technique could be used to estimate the SNR of band limited stochastic functions [65]. This technique has been exploited in the field of electron microscopy [66, 67]. In this section, we introduce the correlation technique in MRI to estimate the SNR directly from the time domain data, by cross-correlating two acquisitions of the same MR image. The correlation technique is very useful in MRI, as MR images are acquired in the Fourier domain. Indeed, because of the correlation theorem, it is favorable in terms of processing time to perform a correlation of images in the Fourier domain, which makes the technique extremely suited for implementation in a highly efficient way in many MR image acquisition procedures.

In Subsection 7.2.1, the theory of the correlation technique is outlined. In Subsection 7.2.2, two experiments are described in which the accuracy and precision of the SNR estimation is tested. The results of the experiments are reported in the last section. Finally, a practical way of implementing the SNR estimation method in an MR image acquisition procedure is proposed and discussed.

7.2.1 Theory

In this section, we outline the theory for estimation of the SNR. In the description of the method, we assume the MR imaging process to be stationary; i.e., the statistical properties of two images, acquired at different times, are equal [68]. We assume that an experimental MR image i, defined on an N×N square lattice, consists of a deterministic signal s, corrupted by additive, uncorrelated noise n with zero mean ($\langle n \rangle = 0$). The signal s includes possible blurring, caused by the system point spread function:

$$i(\vec{r}) = s(\vec{r}) + n(\vec{r}) \quad , \tag{7.3}$$

where $\vec{r}$ denotes the image point coordinates. As a definition of the SNR, the ratio of the signal standard deviation to the noise standard deviation is chosen:

$$\text{SNR} = \frac{\sigma_s}{\sigma_n} \quad . \tag{7.4}$$

The SNR, as defined above, cannot be determined exactly from one experimental acquisition only. However, it has been shown [67] that in case of uncorrelated, additive noise, two consequent acquisitions i_1 and i_2

$$i_1(\vec{r}) = s(\vec{r}) + n_1(\vec{r}) \tag{7.5}$$
$$i_2(\vec{r}) = s(\vec{r}) + n_2(\vec{r}) \tag{7.6}$$

can be used to estimate the SNR. The cross-correlation function (CCF) of the two images becomes:

$$i_1 \otimes i_2 = s \otimes s + n_1 \otimes s + s \otimes n_2 + n_1 \otimes n_2 \quad . \tag{7.7}$$

Since the noise is uncorrelated, one has

$$E\left[n_1 \otimes s\right] = E\left[s \otimes n_2\right] = E\left[n_1 \otimes n_2\right] = 0 \quad , \tag{7.8}$$

so that

$$E\left[i_1 \otimes i_2\right] = s \otimes s \quad , \tag{7.9}$$

i.e., the CCF of the two images is equal to the auto correlation function (ACF) of the signal. This observation is utilized in the cross-correlation coefficient (CCC), which is defined as:

$$\rho(\vec{r}) = \frac{i_1(\vec{r}) \otimes i_2(\vec{r}) - \langle i_1 \rangle \langle i_2 \rangle}{\sigma_1 \sigma_2} \quad , \tag{7.10}$$

where $\langle i_1 \rangle$, $\langle i_2 \rangle$, σ_1 and σ_2 are the mean and standard deviation of the two MR images i_1 and i_2, respectively. The SNR can be computed from the maximum of the CCC. When the two acquisitions are perfectly registered (no shift of the sample has occurred) this maximum occurs in the center of the CCC:

$$\rho_m = \frac{\langle i_1 i_2 \rangle - \langle i_1 \rangle \langle i_2 \rangle}{\sqrt{\left[\langle i_1^2 \rangle - \langle i_1 \rangle^2\right]\left[\langle i_2^2 \rangle - \langle i_2 \rangle^2\right]}} \tag{7.11}$$

or using Eq. (7.9):

$$\rho_m = \frac{\langle s^2 \rangle - \langle s \rangle^2}{\sqrt{\left[\langle s^2 \rangle - \langle s \rangle^2 + \langle n_1^2 \rangle\right]\left[\langle s^2 \rangle - \langle s \rangle^2 + \langle n_2^2 \rangle\right]}} \quad , \tag{7.12}$$

which finally results in the following simple expression:

$$\rho_m = \frac{\widehat{\sigma_s^2}}{\widehat{\sigma_s^2} + \widehat{\sigma_n^2}} \quad . \tag{7.13}$$

From this it is easy to derive the expression for the SNR estimate:

$$\widehat{\text{SNR}} = \sqrt{\frac{\rho_m}{1 - \rho_m}} \quad . \tag{7.14}$$

Notice that the subtraction of $\langle i_1 \rangle \langle i_2 \rangle$ in the numerator along with the denominator make the SNR measurement insensitive for differences in scaling constants between the two MR images.

The calculation of ρ_m can be performed completely in the Fourier domain. Indeed, using Parseval's theorem, one obtains from Eq. (7.11):

$$\rho_m = \frac{\langle I_1 I_2^* \rangle - I_1(\vec{0}) I_2(\vec{0})}{\sqrt{\left[\langle I_1^2 \rangle - I_1^2(\vec{0}) \right] \left[\langle I_2^2 \rangle - I_2^2(\vec{0}) \right]}} \quad , \tag{7.15}$$

where I and I^* are the complex raw MR data and its complex conjugate, respectively. The vector $\vec{0}$ represents the center of the CCC. Eq. (7.15) allows the SNR of the MR image to be calculated directly from the raw MR data. In this way the SNR can be predicted before the Fourier transformation takes place.

The method can be applied, provided the images are perfectly registered. If the acquisitions are not perfectly registered, the maximum of the CCF will in general decrease, which leads to an underestimation of the SNR. However, the CCF maximum will not be affected if the images differ from a uniform translational shift and hence the SNR estimation is still valid. Uniform geometrical registration can easily be performed by examining the position of the CCF maximum. In this way sub-pixel registration can even be achieved by for example bilinear interpolation.

7.2.2 Experiment

MR images were obtained on either an Oxford Biospec imaging system with a horizontal bore of 26.5 cm, a magnetic field strength of 1.9 Tesla, and a maximal gradient strength of 0.01 Tesla/m or on a SMIS MRI apparatus with a horizontal bore of 8 cm, a field strength of 7 Tesla and a maximal gradient strength of 0.2 Tesla/m. A spin-echo (SE) pulse sequence was used with TR = 1 s and TE = 24 ms. Test images were acquired at room temperature from a phantom object (a water filled rod) using a birdcage RF coil. The in-plane spatial resolution was 60 μm in both directions and the slice thickness was 1 mm. The following set of experiments were set up to test the performance of the SNR estimation of the correlation technique. For implementation of the outlined technique, a routine was developed, based on Eq. (7.14) and Eq. (7.15).

The validity of the SNR estimation was tested by averaging N identical MR acquisitions of the phantom object and checking the expected linear behavior of SNR^2 with respect to N. A first image of the phantom object was obtained after averaging N equal acquisitions. A second image was acquired with the same imaging parameters within a time lapse of 5 minutes. From the two resulting images, the SNR was calculated using Eq. (7.14) and Eq. (7.15). This procedure was repeated for different values of N.
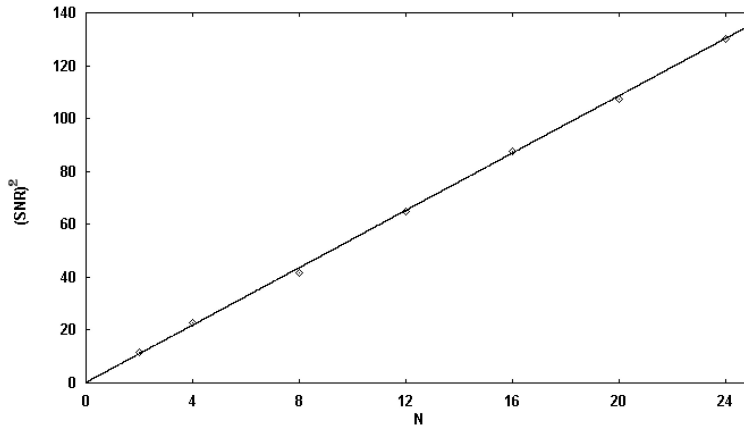
Figure 7.1: SNR^2 as a function of N, the number of acquisitions.

Furthermore, the accuracy of the SNR estimation was tested. This was done by determining the spin-lattice relaxation time T_1 of free water from two independent experiments: firstly from the course of the power spectrum height as a function of the Inversion Time (TI) and secondly directly from the phantom image SNR, calculated with the cross correlation method, described above. In this way, a possible bias in the SNR estimation could be detected.

In the first experiment, the exponential saturation of the signal was measured using an Inversion Recovery pulse sequence. Afterwards, the T_1 relaxation time was estimated by fitting the function

$$\text{SNR} \sim \rho(1 - 2e^{-\text{TI}/\text{T}_1}) \tag{7.16}$$

to the data, where ρ is the pseudo proton density of free water.

In the second experiment, the SNR was estimated of 30 images of the same phantom object, which were taken with incrementally larger TI values. A fast imaging sequence (snapshot FLASH) was used for this experiment. To minimize the influence of the spin-spin-relaxation (T_2), the smallest possible echo time TE = 1.7 ms was chosen. Because only the signal standard deviation of the acquired images changes with TI, the SNR data are expected to follow Eq. (7.16). From these data, the T_1 parameter could again be estimated. In both experiments, the theoretical curve [see Eq. (7.16)] was fitted to the data, using a two-parameter least squares fit.

7.3   Results and discussion

The precision of the image SNR estimate will be a complex function of the deterministic signal components of the image pixels, the number of pixels and the image noise variance. In general however, the SNR will improve linearly with the square root of the number of acquisitions, as can also be observed from Fig. 7.1. From independent SNR measurements of 50 acquisitions of the same image, the relative error of the SNR value for a 256×256 image was found to be within 2%. Here, the relative error is defined as the standard deviation of the SNR divided by the mean SNR. It is clear that the outlined method to estimate the SNR will even be much more precise for 3D images.

Fig. 7.2(a) shows the amplitude of the FID-signal as a function of TI. The data fitting to the theoretical curve of Eq. (7.16) reveals a T_1 value of (2800 ± 110) ms. This value is confirmed from the SNR measurements of images, which were taken with incrementally larger TI values. Also from Fig. 7.2(b) an exponential saturation of the SNR can be observed. The data fitting reveals a T_1 relaxation time of (2880 ± 90) ms. The observation that the T_1 values, obtained from two independent
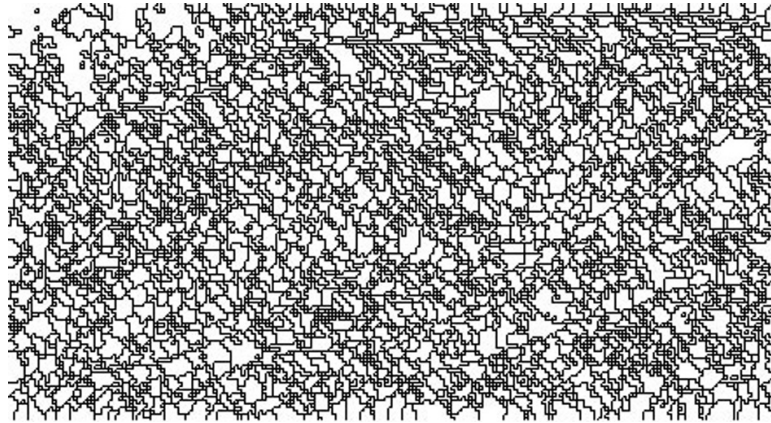
(a) Measurements of the FID amplitude as a function of TI
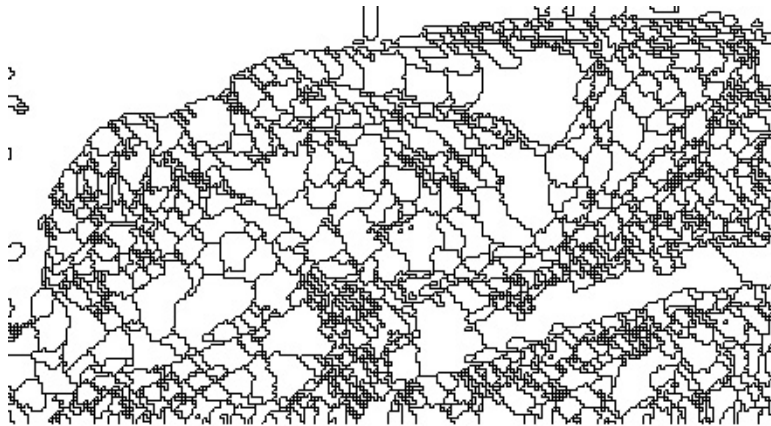
(b) SNR measurements from T_1 weighted images as a function of TI

Figure 7.2: Test of the cross-correlation SNR measurement: the T_1 relaxation parameter is estimated from FID amplitude measurements and from image SNR measurements.

experiments, are equal, indicates that there is no bias in the estimation of the SNR.

Finally, the use of the SNR estimation technique is suggested as an on-line evaluation of the image quality in terms of random noise. The next strategy could be followed during a Magnetic Resonance Imaging procedure. Instead of averaging directly multiple acquisitions to increase the SNR, the acquisitions are stored in two equal sets on the disk and are averaged separately. Each time a new pair of acquisitions is obtained, the SNR of the two sets averaged so far, is measured. At the end, the two sets can be combined again for additional improvement of the SNR. It must be stressed that the proposed SNR estimation technique is independent of the way K-space was sampled during the acquisition, i.e., independent of the pulse sequence, field-of-view, number of phase encode steps, etc. As a consequence, the described techniques can be implemented in any pulse sequence.

Chapter 8

SNR Improvement

8.1 Introduction

In this chapter, methods to improve the image signal-to-noise ratio (SNR) are discussed. The image SNR can be improved by either time or spatial averaging. The main goal is to increase the SNR, while leaving the spatial resolution intact.

The most common noise reduction technique is time averaging. It has the major advantage that SNR is increased while the spatial resolution remains intact, provided the imaging process is stationary. While this approach is quite time consuming and hence almost impossible in case of conventional 3D MR imaging, time averaging is usually replaced by spatial averaging. Wang and Lei [21] justified the heuristics that an MR image can be regarded as consisting of many regions in which the signal is stationary, has a Gauss probability density function (at high SNR) and is ergodic in the mean and variance. The mean ergodic property justifies the use of spatial averaging, within those regions, to estimate the pixel expectation value. The main problem is to find these stationary regions. In conventional lowpass filtering [69, 70], these filters act in the Fourier space, where all local spatial coherence is lost. As a consequence, although SNR increases significantly and is able to reduce Gibbs ringing artifacts, spatial resolution is severely degraded [71]. Recently, wavelet analysis [72] was proposed to overcome this and is quite effective in noise reduction and edge enhancement. However, the reported findings also indicate that some local edge artifacts are introduced [73].
The problem of finding the proper area for spatial averaging is partly solved by the so-called sigma filters [74], where spatial averaging is halted, as soon as strong image gradients are detected [75]. A more elaborated approach can be found in the work of Perona et al. [76], who developed an anisotropic diffusion scheme for image data, where the diffusion and flow functions are guided by local gradient strengths in different directions. The properties of Perona's filter are: 1) efficient noise removal in homogeneous regions 2) preservation of object boundaries and 3) edge sharpening. This filtering technique was successfully applied to 2D and 3D MR data by Gerig et al. [32]. Although the performance of the noise filter is excellent, the underlying image model is piecewise constant or slowly varying. As a result, the edge sharpening causes a region with a constant greyvalue slope to be broken up in constant plateaus. The edge sharpening property is not retained in the approach of Yang et al. [31]. In his paper, he also proposed a more robust way of measuring the anisotropy of the local structure [77]. In Subsection 8.3.2, this anisotropic diffusion filter is discussed. It will play an important role in the segmentation scheme, described in Chapter 9.

8.2 Time averaging

If one wishes to improve the image quality, one could start by improving the SNR of the FID's. An obvious way to achieve this is by signal averaging. Averaging FID's is shown to improve the SNR in proportion to the square root of the number of FID's averaged. An averaged FID $S_a(\vec{k})$ from N_{av} independent signal realizations $S_i(\vec{k})$ is defined by:

$$S_a(\vec{k}) = \frac{1}{N_{av}} \sum_{i=1}^{N_{av}} S_i(\vec{k}) \quad , \tag{8.1}$$

where $\vec{k}$ denotes the raw data point in K-space. If the noise is assumed to be uncorrelated, having variance σ_i^2, the variance of $S_a(\vec{k})$ can be shown to be

$$\sigma_a^2(\vec{k}) = \frac{1}{N_{av}^2} \sum_{i=1}^{N_{av}} \sigma_i^2(\vec{k}) \quad . \tag{8.2}$$

If the noise variance in each data point is additionally assumed to be equal, i.e., $\sigma_i^2(\vec{k}) = \sigma_n^2$, Eq. (8.2) becomes:

$$\sigma_a^2 = \frac{1}{N_{av}} \sigma_n^2 \quad . \tag{8.3}$$

Hence, as previously discussed, the SNR improvement by time averaging can be seen to be a factor of $N_{av}^{1/2}$:

$$\mathrm{SNR}_a(\vec{k}) = \sqrt{N_{av}} \mathrm{SNR}_i(\vec{k}) \quad . \tag{8.4}$$

It must be kept in mind that time averaging reduces only the contributions of random noise. Structured noise was not incorporated, which is in practice always present in MR images. For this reason, the image quality in an MR image cannot be increased indefinitely by time averaging [78]. As one continues increasing the number of averages, one ultimately reaches a region where the noise in the images is not due to random uncorrelated noise, but results from other systematic errors, which manifest themselves as correlated noise. The limitation of SNR improvement by averaging is similar to the case of photon imaging, where one encounters photon and detector noise. By increasing the dose (e.g., X-ray CT) the photon noise may be made arbitrarily small through integration but ultimately one asymptotically approaches a region where the images are dominated by detector noise rather than the photon noise (such as non-uniformity in a gamma camera).

Beside limits to SNR improvement by time averaging, due to structural noise, a more important aspect arises, which is the time constraint. A large number of averages is in practice not achievable, since it would require an unreasonable amount of time to gather the data. Because of this time constraint, one is normally limited to work with a small number of averages, such that the SNR response to the square root of the number of averages is linear.

8.3 Spatial averaging

8.3.1 Cross correlation

In Section 7.2, we saw that the cross correlation function (CCF) of two acquisitions of the same MR image reduces to the auto-correlation function (ACF) of the noiseless image. This property can also be exploited to improve the SNR. Indeed, the Fourier spectrum of the CCF leads to an estimate of the deterministic signal power spectrum $|S(\vec{k})|^2$ with

$$\left| S(\vec{k}) \right|^2 = \frac{I_1(\vec{k}) I_2^*(\vec{k}) + I_2(\vec{k}) I_1^*(\vec{k})}{2} \quad . \tag{8.5}$$

If the acquisitions I_1 and I_2 would not be corrupted by noise, the power spectrum would be positive everywhere. However, due to the noise, some points in the estimated spectrum may become negative. Because of the a priori information that the power spectrum should be positive everywhere, these pixel values are forced to zero. From Eq. (8.5), an estimate for the complex signal spectrum is derived:

$$\widetilde{S}_F(\vec{k}) = \sqrt{\left|S(\vec{k})\right|^2} e^{j\Phi(\vec{k})} \quad , \tag{8.6}$$

where Φ is the phase of the averaged complex image $\frac{I_1 + I_2}{2}$.

As was pointed out by Bonnet [79], another estimate of the signal spectrum is given by:

$$\widetilde{S}_W(\vec{k}) = \frac{\left|S(\vec{k})\right|^2}{\left|I(\vec{k})\right|} e^{j\Phi(\vec{k})} \quad , \tag{8.7}$$

which is obtained by using a Wiener filter, combined with the correlation procedure. This estimate leads to the best result in a least squares sense. Hence, this filter is especially recommended for images, corrupted by Gauss distributed noise. Like the SNR estimation method using cross correlation, SNR improvement using cross correlation will not be affected by a uniform translational shift between the two realizations.

Materials and methods

The SNR improvement was in a first phase tested by simulation experiments. Thereby, an image was constructed, consisting of a number of Gauss functions with arbitrary width and position. Of that image 8 copies were made, after which each image was independently corrupted with Gauss distributed noise. Next, SNR improvement was accomplished in three ways:

- Two of the 8 images were averaged on a pixel-by-pixel base (time averaging). The same was done for another pair of images. Of the resulting 2 images, the SNR was computed using Eq. (7.14) and Eq. (7.15).

- Next, the SNR of the time-averaged images was additionally improved by averaging 2 neighboring pixels, as to obtain an additional SNR improvement of a factor $\sqrt{2}$. Again, from the two resulting images the SNR was estimated.

- Finally, the SNR improvement was estimated after independent cross-correlation of another two pairs of images.

The same simulation experiment was repeated 100 times as to obtain accurate estimations of the variances of the SNR measurements.

The loss of resolution, which is an expected side effect of improving the SNR with any noise filter, was estimated by tracing the K-space position, where the signal spectrum disappeared in the noise spectrum: this point is referred to as the resolution limit. The resolution limits of the time averaged images (0% loss of resolution) and the time+spatial averaged images (50% loss of resolution) were used as reference resolution criteria. From these two resolution limits, the resolution limit for the cross-correlation methods was deduced.

It must be stressed that the resolution criterion used here is a global image resolution measure, which is easy to use. However, a much more powerful approach to describe resolution is based on the estimation of parameters that describe the imaging (and hence image-) model. Thereby, resolution is described in terms of the precision with which model parameters can be estimated. For an excellent treatment of model based resolution, it is referred to the Ph.D. thesis of A.J. den Dekker [80].

Next to the simulation experiment, MR images were acquired in the same way as was described in the first paragraph of Subsection 7.2.2. The applicability to enhance the SNR of MR images of realistic objects was tested in the following experiment. Four independent acquisitions of the same MR image of a cucumber were acquired (TR = 1s ; TE = 30ms) with an in-plane resolution of 0.4 mm and slice thickness of 2 mm. The signal spectrum was estimated via two by two cross-correlation of the images using Eq. (8.5), after which the SNR was calculated from the two final images. Again, the results were compared with the averaging procedures, described in the previous paragraph.

In addition to the SNR measurement of the filtered images, the contrast-to-noise ratio (CNR) for two distinct regions in the image is computed because this parameter is a better description of the visual perception. The CNR is defined as:

$$\text{CNR} = \frac{\langle s_a \rangle - \langle s_b \rangle}{\sigma_n} \quad , \tag{8.8}$$

where $\langle s_a \rangle$ and $\langle s_b \rangle$ denote the mean signal of region a and b, respectively. The noise standard deviation can easily be found from Eq. (7.9):

$$\sigma_n^2 = \left[\frac{i_1 \otimes i_1 + i_2 \otimes i_2}{2} - i_1 \otimes i_2 \right]_{max} \quad . \tag{8.9}$$

The CNR is expected to increase with the same factor as the SNR, as the improvement is based on the decrease of the noise power with only minor signal modifications. To test this hypothesis, two homogeneous regions, the seeds and the pulp, were selected from the cucumber image, after which the CNR was calculated for different filtered images, thereby using the same regions of interest.

Results and discussion

The results of the simulation experiment are shown in Table 8.1. The gain in SNR and CNR, along with the estimated loss of resolution, are shown for an original, noisy image, for the time average of two acquisitions, for images processed with the proposed correlation techniques, and for a the time averaged image with additional 2×1 spatial filtering. As is expected, the SNR improvement due to time averaging is indeed the square root of the number of averages (here $\sqrt{2}$), with no loss of resolution. After additional 2×1 spatial averaging (latter filter), the SNR improvement, compared to the time averaging, was $\sqrt{2}$, as is also expected.
The SNR improvement by cross-correlation, using Eq. (8.6) or Eq. (8.7), was observed to be a factor of 2.15 and 1.93, respectively.
Resolution loss of the original, noisy image was defined to be 0%. The loss of resolution due to the spatial averaging was used as a second reference resolution measure: it was defined to be 50%. Although the cross correlation methods revealed an SNR improvement of about a factor of 2, spatial resolution was better retained as can be observed from Table 8.1.

For the SNR improvements on MR images, we have also observed that, using the correlation method, the SNR improves with almost a factor of 2. The SNR of the unprocessed images was 3.24. Fig. 8.1(a) shows one of the four acquisitions of the original image. Fig. 8.1(b) is the average of the two acquisitions with SNR = 4.57. The results after improvement using Eq. (8.6) and Eq. (8.7), are displayed in Fig. 8.1(c) and 8.1(d), respectively. The SNR is 5.57 and 6.03, respectively. When using Eq. (8.6) and Eq. (8.7), the upper limit of the gain in SNR is determined by the noise on the Fourier phase, as the phase is obtained from a simple average of the two input images. Hence the phase image is necessarily polluted by noise. Till now we did not find a better way to reduce the noise contributions in the Fourier phase image.

As can be observed from the images in Fig. 8.1, the correlation method improves the SNR but, simultaneously, slightly decreases the image resolution. This blurring effect occurs with all noise-reducing techniques. In this procedure, it is probably caused by forcing the negative values of the estimated signal power spectrum to zero.

Finally, it is noted that SNR improvement by cross-correlation is independent of the way images were acquired in K-space. As a consequence, the described technique can efficiently be implemented in any pulse sequence. The computational requirements are limited.

	SNR	RESOLUTION LOSS (%)
Original image	1.232 ± 0.005	0
Time averaged	1.744 ± 0.006	0
Correlated	2.370 ± 0.010	24 ± 1
Wiener correlated	2.644 ± 0.011	26 ± 1
Time + spatial averaged	2.456 ± 0.008	50

Table 8.1: SNR and resolution measures for an original, unprocessed image, a pixel-by-pixel average of two acquisitions (time average), a correlated image, a Wiener-correlated image, and a 2×1 spatial average of the time averaged image.

	SNR	CNR
Original image	3.24	2.93
Time averaged	4.57	4.16
Correlated	5.57	5.04
Wiener Correlated	6.03	5.55
Time + spatial averaged	6.41	5.78

Table 8.2: SNR and CNR measures for an original image, a pixel-by-pixel average of two acquisitions (time average), a correlated image, a Wiener-correlated image, and a 2×1 spatial average of the time averaged image.

8.3.2 Anisotropic adaptive diffusion filter

As we saw in the previous sections, improvement of the SNR seems to be an inevitable trade off between increasing the acquisition time (time averaging) and decreasing the spatial resolution (spatial averaging). In this section, the adaptive anisotropic diffusion filter is discussed, which is able to increase the image SNR significantly while leaving the spatial resolution almost intact. In the following, we review the adaptive anisotropic diffusion filter and present an extension to 3D.
Suppose $f(\vec{r})$ is a 3D image, where $\vec{r} = (x_1, x_2, x_3)$ is a three-dimensional position vector. The filtering process consists of convolving $f(\vec{r})$ with a Gauss kernel $h(\vec{r})$ of which the shape is pointwise adapted to the local structure within a neighbourhood Ω. De resulting filtered function $g(\vec{r})$ can be written as follows:

$$g(\vec{r_0}) = \frac{\iiint\limits_{\Omega} h(\vec{r_0} - \vec{r}) f(\vec{r}) d\vec{r}}{\iiint\limits_{\Omega} h(\vec{r_0} - \vec{r}) d\vec{r}} \quad , \tag{8.10}$$

where

$$h(\vec{r} - \vec{r_0}) = \exp\left[-\frac{1}{2} \sum_{i=1}^{3} \frac{((\vec{r} - \vec{r_0}).\vec{n_i})^2}{\sigma_i^2(\vec{r_0})}\right] \quad . \tag{8.11}$$

(a) Original   (b) Time averaged   (c) Correlation technique
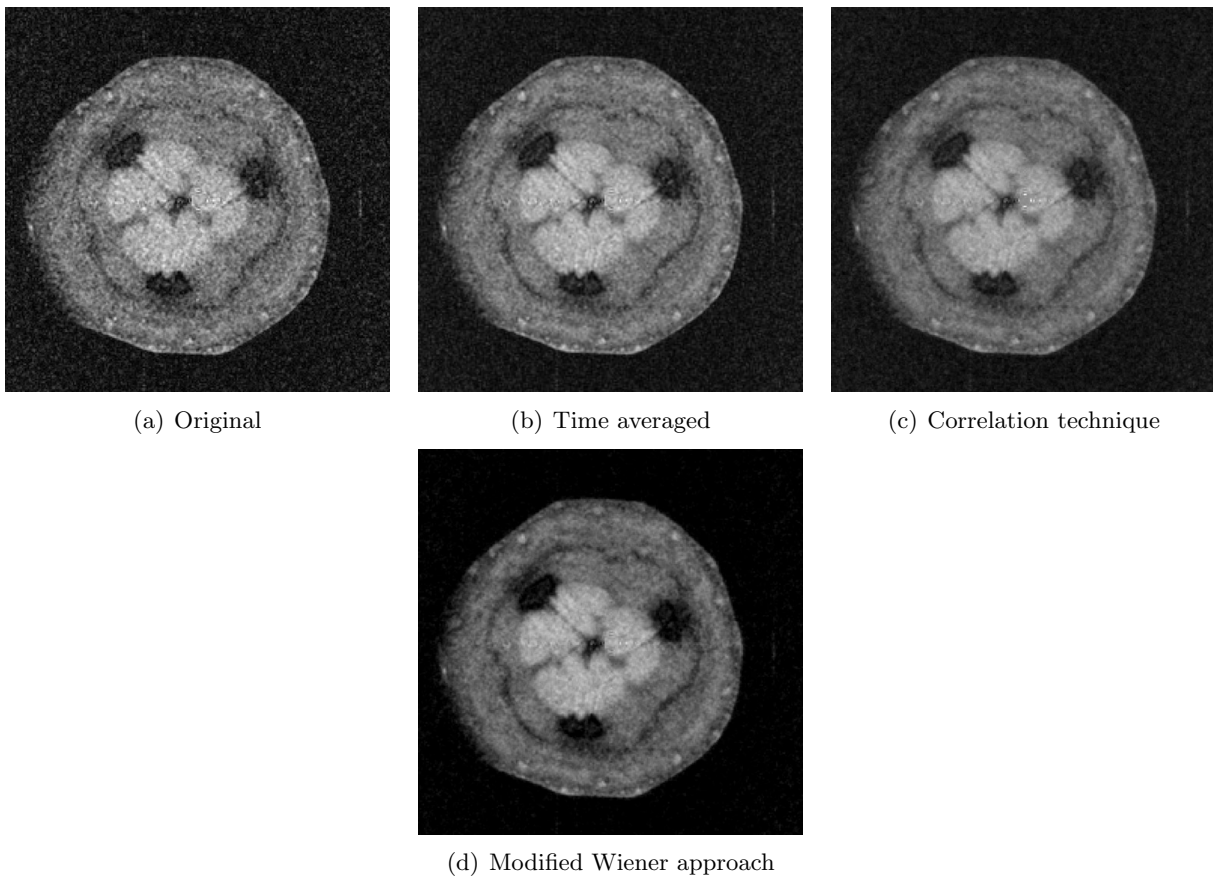

(d) Modified Wiener approach

Figure 8.1: Perceptual comparison of SNR improvements.

In Eq. (8.11), the vectors $\vec{n}$ are the eigenvectors of the $3{\times}3$ second moment matrix R of the Fourier spectrum $|F(u)|^2$. The coefficients of R can as well be calculated in the spatial domain:

$$R_{ij} = \iiint\limits_{\Omega} u_i u_j |F(u_1, u_2, u_3)|^2 du_1 du_2 du_3 \tag{8.12}$$

$$= \frac{1}{(2\pi)^3} \iiint\limits_{\Omega} \left(\frac{\partial f}{\partial x_i}\right)\left(\frac{\partial f}{\partial x_j}\right) dx_1 dx_2 dx_3 \quad , \tag{8.13}$$

where $i, j = 1, 2, 3$. R is positive semi-definite and Hermitian, hence having only positive eigenvalues. The direction of the eigenvector $\vec{n}_1$, corresponding to the smallest eigenvalue, say λ_1, determines the main direction of the pattern in the neighbourhood Ω of the spatial domain. Alternatively, the three eigenvalues λ_1, λ_2, and λ_3, with $\lambda_1 \leq \lambda_2 \leq \lambda_3$, determine the relative orientation of the pattern in the respective directions.

The shape of the kernel h [see Eq. (8.11)] is controlled by the standard deviations σ_1, σ_2 and σ_3, which are functions of the local gradient strength in the respective directions. From the eigenvalues, anisotropy measures are derived, which are used to design the standard deviations:

$$a_{12} = \frac{\lambda_2 - \lambda_1}{\sum\limits_i \lambda_i} \quad \text{and} \quad a_{13} = \frac{\lambda_3 - \lambda_1}{\sum\limits_i \lambda_i} \quad . \tag{8.14}$$

The standard deviations should be large along the main direction(s) of the pattern, such that the data are only smoothed in homogeneous regions and along instead of across edge surfaces.

In addition, corners should be preserved during filtering. A corner is identified as a condition, where the pattern is relative isotropic ($a_{12} \approx 0$; $a_{13} \approx 0$), while the local gradient strength $|\nabla f(\vec{r})|^2$ is large. Therefore, a spatial dependent corner strength C is defined as:

$$C(\vec{r}) = (1 - a_{12} - a_{13})|\nabla f(\vec{r})|^2 \quad . \tag{8.15}$$

From Eq. (8.14) and Eq. (8.15), the standard deviations are designed as follows:

$$\sigma_1(\vec{r}) = \frac{\sigma}{1 + C(\vec{r})} \quad \sigma_2(\vec{r}) = \frac{\sigma(1 - 2a_{12})}{1 + C(\vec{r})} \quad \sigma_3(\vec{r}) = \frac{\sigma(1 - a_{12} - a_{13})}{1 + C(\vec{r})} \quad , \tag{8.16}$$

where σ stands for the standard deviation of the image noise. As we saw in Chapter 4, σ can be estimated directly from a large, uniform signal region as the standard deviation of the voxel values in that region [40]. The simplest way, however, is by estimating the noise from signal amplitude values of non-signal regions [40], as these are often easier to find than large homogeneous signal regions. The noise standard deviation is then given by 1.53 times the measured standard deviation of the background voxel values. The multiplication constant results from the fact that background noise obeys a Rayleigh distribution [19, 49]. We used the background for noise estimation.

The effect of the adaptive anisotropic diffusion filter can be appreciated from Fig. (8.2), where the filter was applied to the cucumber image described in the previous section. Although it is acknowledged that the SNR improvement strongly depends on the image content, the SNR of this example was 2.4, while the general resolution loss as was defined above was observed to be 8 %.

In the next chapter, a segmentation scheme will be discussed, where the anisotropic adaptive diffusion filter, described here, is first applied to the image data. After the filtering process, the gradient magnitude image is calculated for the next phase in the segmentation procedure. In order to save computation time, one could argue that, instead of filtering and afterwards edge detecting, it would be more sensible to construct a robust edge detector. This however is not true. The gain in SNR, when filtering the original data, is due to spatial averaging in all directions. On the other hand, only the response of an edge detector in the direction corresponding to a strong gradient, increases the SNR. The response of the edge detector in the other directions does not increase the SNR; it even may lower the SNR.

(a) Original   (b) Adaptive anisotropic diffusion fil-
                                ter
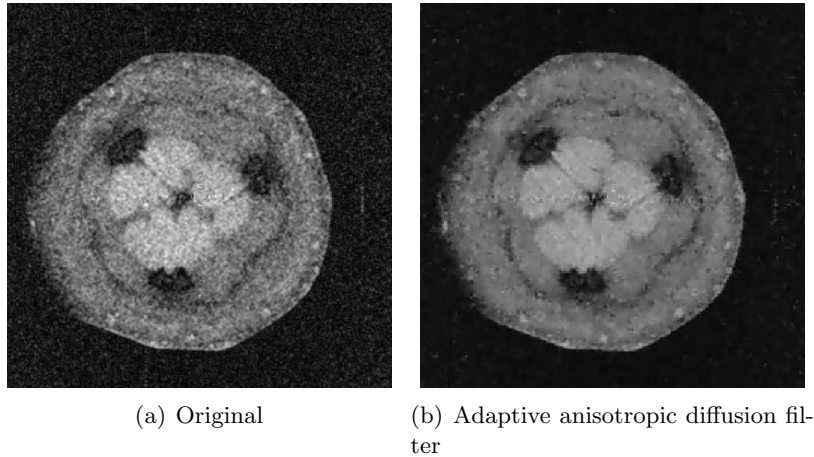
Figure 8.2: Diffusion filter: perceptual comparison of the SNR improvement.

8.4 Conclusions

Commonly, the image SNR is improved by time integration of raw MR data. For a stationary imaging
process, the SNR improves with the square root of the number of signal averages, without loss of
resolution. However, as acquisition time is limited, one is forced to apply noise filtering techniques
based on spatial averaging, which often goes along with loss of spatial resolution. In this chapter,
a method was proposed to improve the SNR, based on cross-correlation, which can be efficiently
implemented in most MR imaging sequences. The method was shown to improve the SNR with only a
minor expense of spatial resolution. Furthermore, it was demonstrated that the anisotropic adaptive
diffusion filter is capable of increasing the image SNR significantly while retaining the image details as
good as possible. A disadvantage of the latter filter, however, is the high computational requirements.
Finally, it need to be remarked that the anisotropic adaptive diffusion filter was originally constructed
for Gauss distributed data. Hence, the filter should only be applied to magnitude MR data when the
image SNR is high. Future work will focus on the construction of a similar filter for Rice distributed
data.

Chapter 9

3D Image Segmentation

9.1 Introduction

In many image processing tasks, segmentation is an important step toward the analysis phase. It allows quantification and visualization of the objects of interest. Recently, image segmentation methods were extensively reviewed by Clarke et al. [81]. They concluded that segmentation of medical images is still a difficult task and fully automatic segmentation procedures are far from satisfying in many realistic situations. Merely when the intensity or structure of the object differs significantly from the surroundings, segmentation is obvious. In all other situations, manual tracing of the object boundaries by an expert seems to be the only "valid truth", but it's undoubtedly a very time-consuming task.

On MR data, fully automatic image segmentation techniques have been developed, which can be subdivided in two major classes: gray scale single image segmentation and multispectral segmentation. Regarding the first class, the most intuitive approach is the threshold-based segmentation method, where the threshold is chosen globally [82, 83] or locally [84]. The method is restricted to relative simple structures and is hindered by variability of anatomical structures as well as image artefacts. Other approaches make use of edge detection for image segmentation [85, 86]. These, however, suffer from over- or undersegmentation, induced by improper threshold selection [87]. In addition, the edges found are usually not closed, such that edge linking techniques are further required. Concerning the multispectral class, segmentation techniques using clustering techniques like k-means clustering [88, 89], adaptive hierarchical clustering [90, 91], etc., are applied [92]. Like all unsupervised segmentation techniques, multispectral data analysis is fully automatic and superior in reproducibility, but it can only be exploited when the MR characteristics of the object of interest differ significantly from those of the surrounding structures.

On the other hand, results of supervised segmentation are less reproducible, but the segmentation process can be controlled by the operator. We choose for a semiautomatic single image segmentation procedure for 3D MR images in which user interaction is allowed to control the segmentation process and in which data are preprocessed as far as possible, such that the posterior user-interaction time is strongly reduced [93].

The first preprocessing step concerns the reduction of random noise, as segmentation results are usually highly dependent on image noise. This is because noise tends to dislocate edges and hampers the detection of fine image detail. In this chapter, we demonstrate the effect of random noise reduction. Among the vast amounts of noise filtering schemes already available in the literature, we choose for the filter that best serves the posterior segmentation method: the adaptive anisotropic diffusion filter, which was described in Subsection 8.3.2. In that section, it was shown that the filter is able to smooth out homogeneous regions while retaining the edge information in an anisotropic manner,

which is indispensable for accurate image segmentation. The diffusion filter is applied to combat over-segmentation of the data. In Section 9.3, the influence of this filter on the final segmentation results will be demonstrated.

The actual segmentation technique starts with a subdivision of the data in basic volume elements, called catchment basins, by application of a watershed algorithm to the gradient magnitude of the original 3D data set. Among several existing algorithms, the immersion-based approach of Vincent and Soilles [94] was selected because of its accuracy and speed of computation [95]. The technique is based on the assumption that image contours correspond to the crest lines of the gradient magnitude image, which can be detected via watershed tracing. The output of the watershed algorithm is a partitioning of the input data in volume regions of which the interior does not contain any sharp gray value transitions. Without preprocessing of the data, the algorithm leads inevitably to an oversegmentation of the data, as all the crest lines of the data set are detected. Therefore, the adaptive anisotropic filter [31], mentioned above, is a priori applied to the image data.

Afterwards, oversegmentation is additionally reduced by merging basic volume elements. A 2D merging scheme was suggested by Maes et al. [96], who used the Minimum Description Length Principle [97, 98, 99] to deal with the oversegmented output of the watershed algorithm. Thereby, the description length, i.e., the number of bits to encode each region primitive, was calculated. For encoding of the interior region an entropy criterion was applied, while the boundary was encoded by chain coding. Regions are merged when the total description length gain is positive. However, problems arise because not all regions can be chain coded uniquely. Moreover, extension to 3D using this criterion is not possible, as the boundary surface cannot uniquely be determined in the same way as was done in 2D. Also, for calculation of the entropy, the probability density function of the basic volume element is required. Thereby, the unknown distribution is usually estimated by convolving the original histogram with a Gaussian Parzen window [100]. However, because of the high number of basic volume elements, the convolution with each histogram would severely slow down the merging process.

In this chapter, an alternative merging scheme is proposed, based on hypothesis testing, which is not dimension restricted and computationally far less complex. Thereby, small volume primitives are merged with the most similar neighbouring region. In this way, the number of basic volume elements is significantly reduced, such that user interaction time during the posterior semiautomatic segmentation is strongly minimized.
All preprocessing steps are fully automatic. The final extraction of the object of interest takes place in the last part. The first slice is manually segmented, after which all subsequent slices are automatically segmented. Each segmentation result is contingently manually corrected by the user.

The accuracy of the presented volume quantization method is in a first phase tested on phantom objects with known volumes. In addition, the segmentation technique is applied to 3D MR data of the mouse head. It has been reported that the vermis of the cerebellum is smaller in human fragile X [1] patients than in controls [101]. Similar observations were made on patients with autism from 2D Magnetic Resonance scans [102] and on mice with the fragile X syndrome from 2D micrographs of histologic slices [103]. The authors reported volume measurements, obtained from invasive techniques (slicing of the fixated mouse head), where errors of more than 10% are common. 3D MR imaging and processing enable the study of physiological structures without destroying the object. The 3D information, present in the MR data, can fully be exploited for image processing and analysis. In addition, the nondestructive character of MR imaging allows in vivo study of the object of interest and

---

[1] The fragile X syndrome is caused by mutations in the fragile X gene FMR1. It's the most common cause of developmental disability.

hence allows the study of time-dependent processes. As an application, the volume of both cerebellum and the total mouse brains is computed from the segmentation output. Finally, 3D reconstructions from the segmentation results are shown.

9.2   3D semi-interactive segmentation

The actual semiautomatic segmentation procedure for 3D MR images consists of three parts:

- application of a 3D analogy of Vincent and Soille's watershed algorithm,

- reduction of the oversegmentation by application of a 3D adaptive anisotropic diffusion filter prior to the 3D watershed algorithm. Afterwards, selectively merging neighbouring catchment basins,

- interactive segmentation.

The first two steps are fully automatic. Some user interaction is required in the last part but the preceding ones will be shown to reduce this to a minimum.

9.2.1   Immersion-based watershed algorithm

In the first part, the watersheds of the gradient magnitude of the MR data are calculated. By that, the gradient magnitude image is considered as a topographic relief, where the brightness value of each voxel corresponds to a physical elevation. An efficient and accurate watershed algorithm was developed by Vincent and Soille [94] who proposed an immersion based approach to calculate the watersheds. The operation of their technique can simply be described by figuring that holes are pierced in each local minimum of the topographic relief. In the sequel, the surface is slowly immersed into a 'lake', by that filling all the catchment basins, starting from the basin that is associated to the global minimum. As soon as two catchment basins tend to merge, a dam is built. The procedure results in a partitioning of the image in many catchment basins, of which the borders define the watersheds.

Of all watershed transforms, the immersion technique was shown to be the most efficient one in terms of edge detection accuracy and processing time [95]. For 3D implementation of the algorithm, it is assumed that the crest surfaces of the gradient magnitude of the 4D topographic relief correspond to structure surfaces of the original 3D data. We implemented dynamic linked lists to reduce memory requirements. Also, a 26 connected (cubic) neighbourhood was used, which allows the water to flow in all directions. A 6 connected neighbourhood, i.e., only the first order neighbours, could have been implemented instead to save computation time, but this goes along with a stronger oversegmentation and loss of watershed detection accuracy.

9.2.2   Reduction of oversegmentation

A severe drawback to the calculation of watershed images is oversegmentation. Relevant object contours are lost in a sea of irrelevant ones. This is partly caused by random noise, inherent to MR data, which gives rise to additional local minima, such that many catchment basins are further subdivided. If, however, an anisotropic diffusion filter, described in Subsection 8.3.2, is first applied to the original data, this oversegmentation can already significantly be reduced.
In a next step, the partitioning is additionally diminished by properly merging catchment basins. This is done by iteratively merging neighbouring regions that have similar gray level distributions. The merging criterion is inspired from hypothesis testing, where it is assumed that the population means

(a) mosaic image   (b) region graph
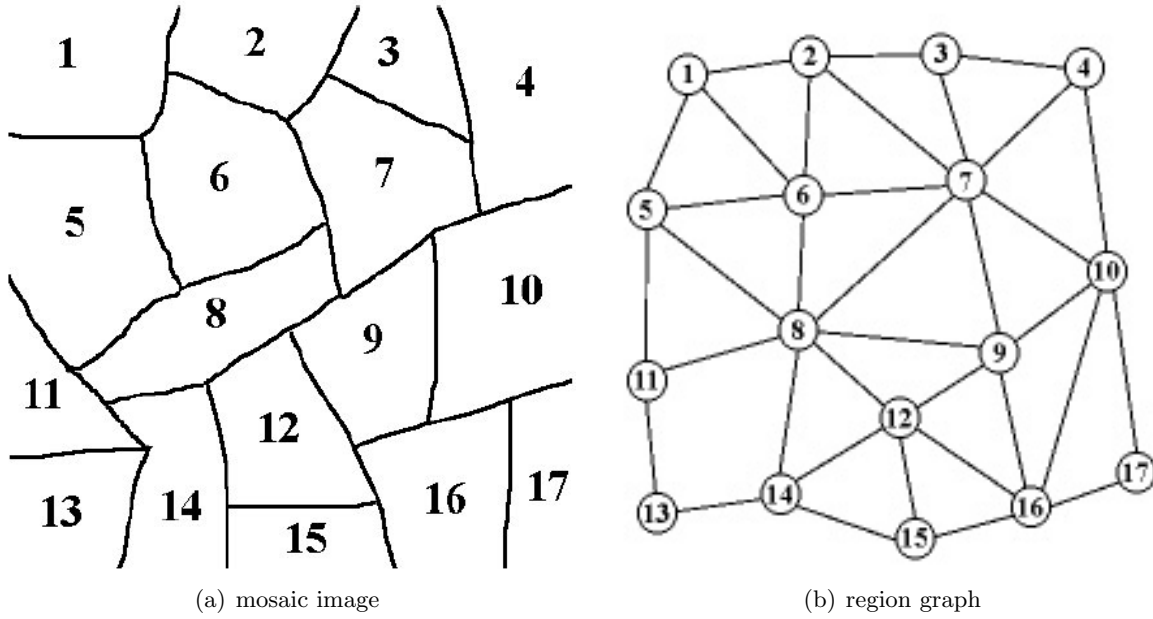
Figure 9.1: Use of a region graph for merging

are equal. Basic volume elements are assumed to be characterized by a Gauss distribution. For small sample size ($n < 30$) a Student's T test is most suited. The applied statistic is then given by:

$$T = \frac{\mu_1 - \mu_2}{\sigma\sqrt{\frac{1}{n_1} + \frac{1}{n_2}}} \quad , \text{ where } \quad \sigma = \sqrt{\frac{n_1 S_1^2 + n_2 S_2^2}{n_1 + n_2 - 2}} \quad . \tag{9.1}$$

The variable T obeys a Student's T distribution with $n_1 + n_2 - 2$ degrees of freedom, n_1 and n_2 denoting the number of pixels within the two populations. μ_1, μ_2 and S_1, S_2 are the estimated population means and standard deviations, respectively. Obviously, the smaller the T value, the similar the distributions are.

The merging process proceeds as follows. The 3D MR data set is characterized by an array of structures, where each structure describes one single basic volume element. The data of a structure contain the following information: the number of voxels, the voxel coordinates, the estimated mean gray value and standard deviation, and an array containing the labels of the neighbouring regions along with the corresponding value of the T statistic. A region graph was implemented for computational efficiency (see Fig. 9.1). The merging process starts by joining the smallest volume element with the most similar neighbouring region; i.e., the region that yields the smallest T value. During merging, all structure information of the two regions is combined and updated. Hereafter, the merging process is continued by again merging the smallest region with one of its neighbours. From our experimental observations, merging of more than about half of the original number of regions was found to degrade the posterior segmentation results too much in the sense that regions on the border of the cerebellum (object to be segmented) started to merge with neighbouring regions from the surroundings. Therefore, the merging process was stopped when half of the original number of regions was merged. This criterion to stop the merging process depends however on the complexity of the segmentation task. In general, the stronger the edges surrounding the object to be segmented, the more regions that may be merged. Reduction of the number of small regions significantly favors the posterior interactive segmentation task, as will be elucidated below.

9.2.3   Interactive segmentation

In the third part, the actual object segmentation takes place. Subsequent 2D slices from the 3D data set are presented to the user. For each slice, we keep track of the basic volume elements that intersect the corresponding slice of the merged data. These volume elements are not visible to the user. The first slice is quickly segmented by manually activating the volume regions that belong to the object of interest, through simple mouse clicking. This is done by drawing a contour around the region of interest, after which all interior regions are activated. All subsequent slices are consequently segmented as follows: The 'core' area of the previous slice (slice A), i.e., the area constituted of all previously activated regions, except those lying at the border, is projected onto the next slice (slice B). All volume elements of slice B that intersect with this core area, are automatically activated. Only the volume elements at the border of the core area of slice B are evaluated for activation. Volume elements at the border are automatically activated if a 'major part' is still contained in the segmentation result of slice A. The term 'major part' depends on the local deformation from one slice to another. If no deformation is observed 'major part' is more than 50%. This percentage is made dependent on the local size change (growing or shrinking) and can range from 0% till 100%. Remark that automatic volume selection in this way does not require the object to be convex. The user contingently manually corrects the result of the automatic segmentation.

The adaptation from one slice to the next one is fully automatic when the local deformation is smaller than the average size of the basic volume elements. For this reason the merging process was designed to iteratively merge only the smallest regions. In this way, user interaction is minimal, mainly due to the efficient use of the 3D information.

9.3   Experiments and discussion

9.3.1   Materials

All data were generated on an MR apparatus (SMIS, Surrey, England) with a horizontal bore of 8 cm, a field strength of 7 Tesla and a maximal gradient strength of 0.2 Tesla/m. In all experiments a birdcage RF coil with a diameter of 32 mm was used. For each experiment a 3D spin echo (SE) pulse sequence was used (TE = 56 ms; TR = 1500 ms) with $FOV_x = FOV_y = 20$ mm and $FOV_z = 22$ mm. The dimensions of the acquisition matrix were $256 \times 128 \times 128$, which was zero-filled to obtain an image matrix of $256 \times 256 \times 256$. The spatial resolution was $R_x = R_y = 78$ μm and $R_z = 86$ μm. For image processing a matrix of $120 \times 220 \times 150$ was chosen as a region of interest. All image processing was performed on an HP 720 workstation.

9.3.2   Phantom object data

After careful gradient calibrations, the proposed segmentation technique for volume quantization was in a first phase checked on images obtained from water filled phantom objects. Although segmentation in this case is obvious, this test was performed to reveal possible biases in the volume quantization. The object volumes were chosen in the range of mouse brain volume: 156, 316, 459 and 756 mm^3. Each phantom volume was quantized three times: the 3D data were presented to the user by slicing in the x-, y-, and z-direction.

Table 9.1 shows the true volumes of the phantom objects, along with the measured volumes. The measured volumes reveal a systematic quantization error of about 2%, while reproducibility tests revealed an intrinsic segmentation error of less than 1%, which indicates that the limiting factor in the volume quantization accuracy is due to the limited accuracy of the gradient calibration. As segmentation of our phantom object was a very simple problem, it is believed that the segmentation procedure itself was extremely accurate. Furthermore, segmentation results of the phantom objects were statistically

tested on their independence of slice direction. Thereby, ANOVA (analysis of variance) was applied to the segmentation results. It was found that the null hypothesis of equal volume means (between and within the slice directions) could not be rejected at a significance level of 0.05.

Table 9.1: Accuracy of phantom volume quantization

| Real object volumes (mm^3)	Volume 1 x-slicing (mm^3)	Volume 2 y-slicing (mm^3)	Volume 3 z-slicing (mm^3)	Volume quantization error (%)
156	163	159	160	1.7
316	322	322	320	0.8
459	469	468	469	0.5
736	753	753	752	0.4

9.3.3 Mouse data

To test the performance of the proposed segmentation technique on real data, we faced the problem of segmenting the cerebellum of mouse brains from 3D MR data. The proposed technique is very well suited for the cerebellum segmentation problem. Firstly because the cerebellum structure is strongly inhomogeneous, i.e., purely histogram-based segmentation techniques are useless. Secondly, multispectral properties can not be exploited to enhance the contrast between the cerebellum and the neighbouring cerebrum, as the cerebellum has no significantly different MR relaxation characteristics, compared to the cerebrum (both consist out of gray and white matter).

3D diffusion filter

The 3D raw MR data of the mouse head are first preprocessed with the anisotropic adaptive diffusion filter. Concerning the filtering neighbourhood Ω the following remarks can be made. First of all the filtering range in one direction should be proportional to the spatial resolution in that direction. In our case a cubic volume Ω was chosen as the raw data were zero filled to obtain a cubic data set. For optimal adaptation of the filtering kernel to the local structure, Ω must be as small as possible (e.g., a $3\times3\times3$ window). However the smaller Ω, the smaller the gain in SNR, which can be compensated by an iterative filtering scheme, although this solution drastically elongates the processing time. As a compromise, we opted for a $5\times5\times5$ voxel window. Fig. 9.2 shows the effect of this operation. Fig. 9.2(a) shows the midsagittal slice from the raw 3D MR data. Because of the large neighbourhood, the filtering process results in a significant noise reduction, as can be observed from the corresponding slice of the 3D output, shown in Fig. 9.2(b). Beside a visual enhancement, the diffusion filter has also an important influence on the output of the immersion-based watershed algorithm. This can visually be appreciated from Fig. 9.3, where the watersheds of the same slice of respectively the original and the filtered data are shown. From Fig. 9.3(a), an oversegmentation can clearly be observed: the volume is subdivided in about 74000 homogeneous volume elements. By diffusion filtering, the number of basic
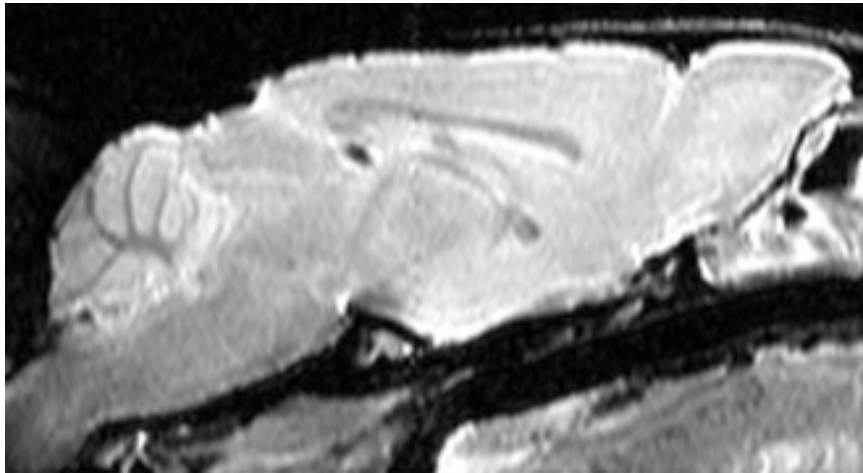
(a) Midsagittal slice from the raw data
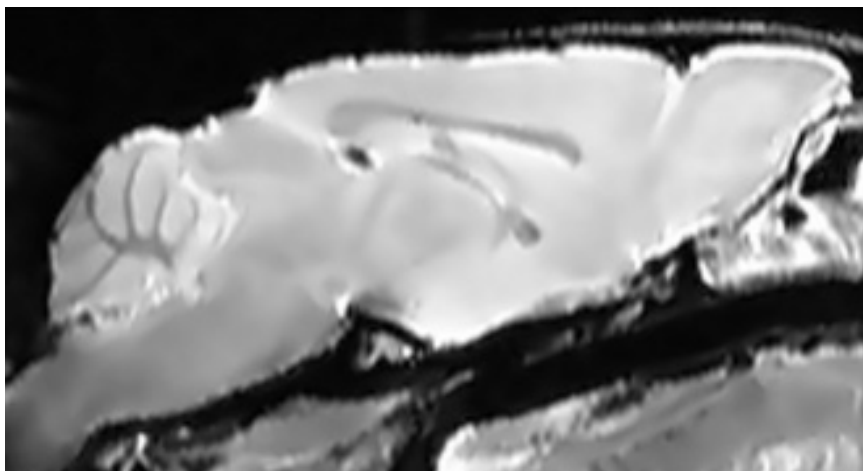
(b) Midsagittal slice from the filtered data

Figure 9.2: Result of 3D adaptive anisotropic diffusion filter.
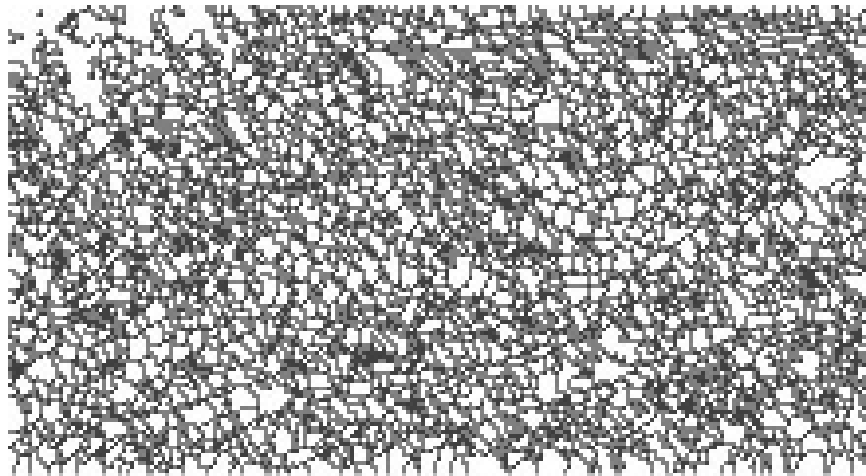
(a) Watersheds from the raw data
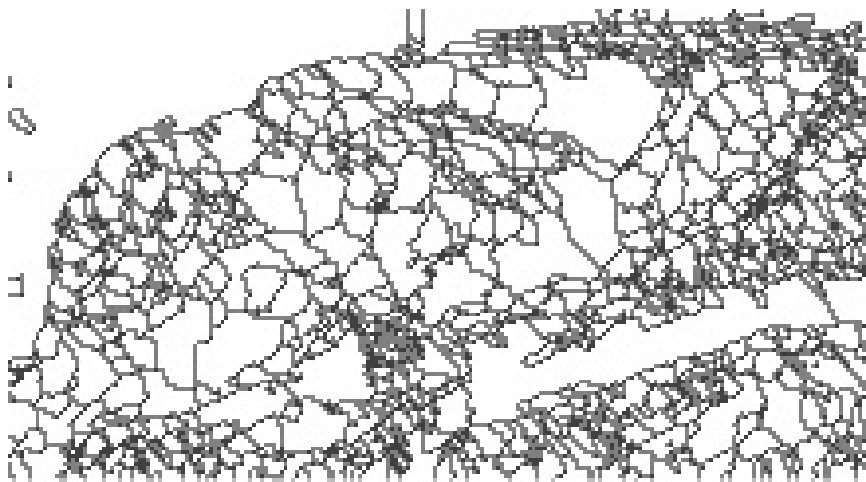
(b) Watersheds from the filtered data

Figure 9.3: Watershed transforms of raw, filtered and merged data.

volume elements in the 3D data set is reduced to less than one third of the original number, as can be seen from Fig. 9.3(b).

Merging

The result of the merging process is shown in Fig. 9.4 where Fig. 9.4(a) is a zoomed area from Fig. 9.3(b). Although the number of volume elements was again halved due to the merging process, it might be hard to observe the differences between Fig. 9.4(a) and Fig. 9.4(b). This is because only the smallest regions were considered for merging. However, the merging operation significantly diminishes the posterior user interaction time. The effect on the size of the volume elements is demonstrated in Fig. 9.5. Fig. 9.5(a) shows the histogram of the region sizes for the raw, filtered and merged data. From this figure, it is clear that many small regions are merged with neighbouring ones. Fig. 9.5(b) shows the cumulative volume histogram. Every curve finally converges to the total volume of the region of interest.

(a) Before merging   (b) After merging
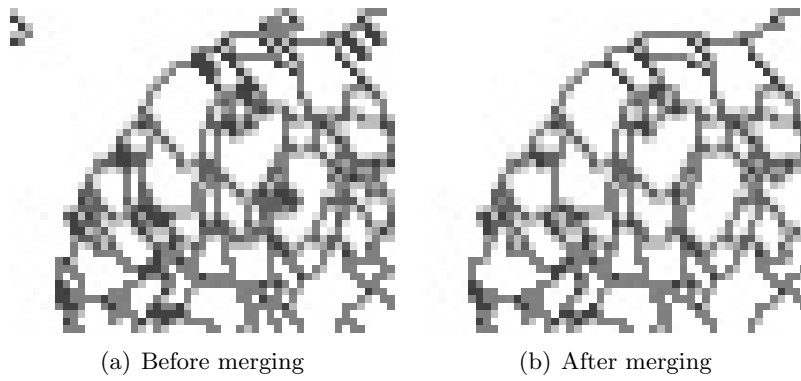
Figure 9.4: Result of the merging process.
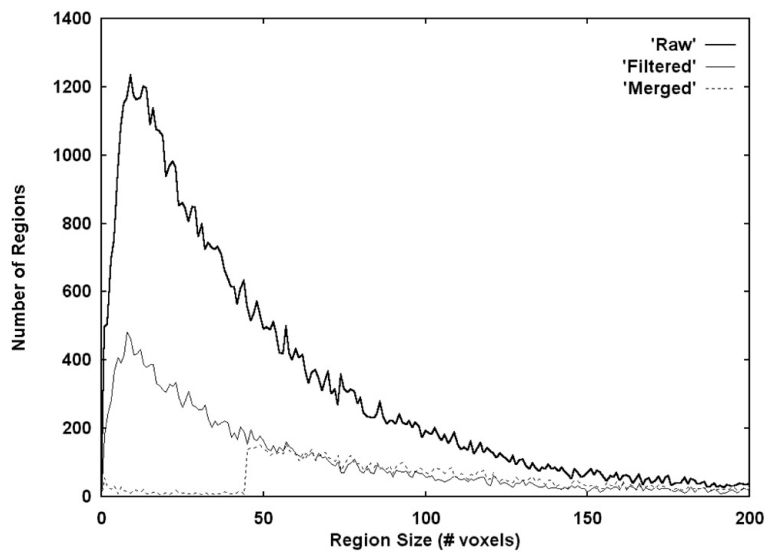
(a) Histogram of the region sizes.
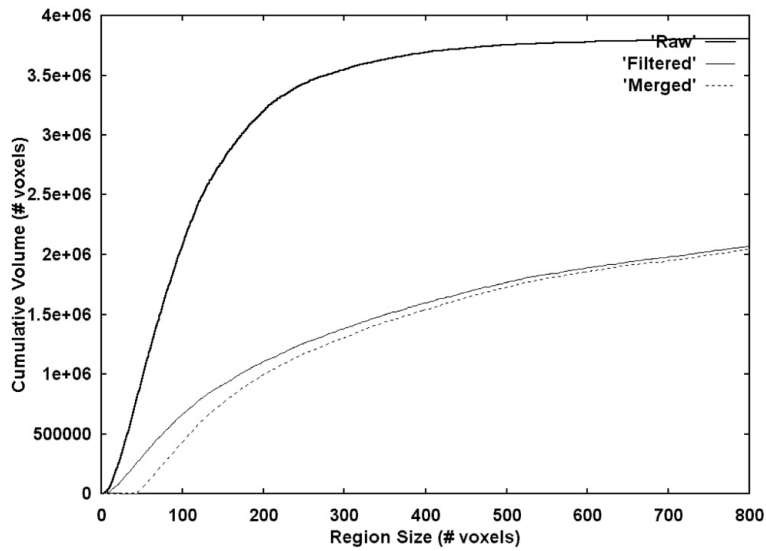
(b) Cumulative volumes histogram.

Figure 9.5: Effect of filtering and merging on the size of the volume elements.
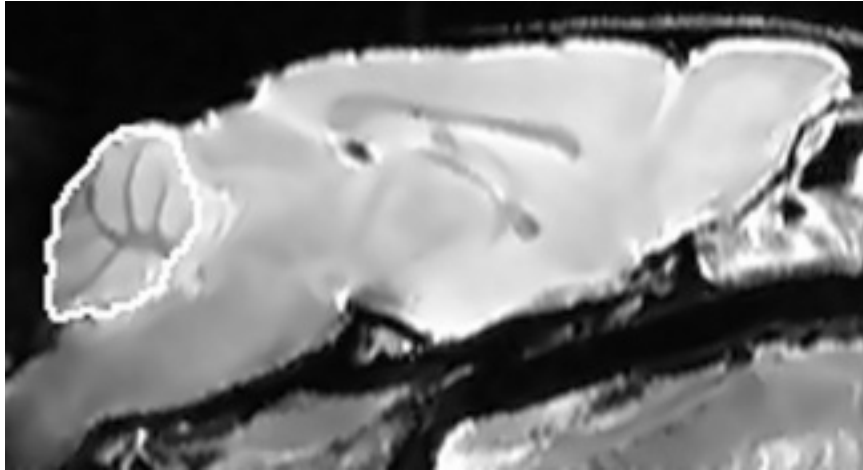
Figure 9.6: Cerebellum extraction via volume element selection.

Interactive segmentation

The result from the full automatic preprocessing steps is presented to the user for manual segmentation. With a few mouse clicks on the first slice, the cerebellum is extracted from the rest of the brains. This is not done by activating each single region from the cerebellum separately, but by selecting a region of interest, in which all volume elements are automatically activated. Starting from this slice, the segmentation process is proceeded, hereby fully exploiting the 3D information of the previously segmented slice. In Fig. 9.6, the segmented result of the midsagittal slice is shown. For clarity, only the border of the segmented volumes in the slice is shown as a white curve.

Volume quantization

Numerical results of the segmentation process are summarized in Table 9.2. Again, the segmentation error was obtain by presenting the slices in the three orthogonal directions. From the table, one can also observe that, as a consequence of the diffusion filter, the average number of manual interactions (mouse clicks) per slice is significantly reduced. Further iteratively merging volume primitives halves this number along with the interaction time. However, reduction of user interaction time goes along with minor expense of segmentation accuracy. For this reason, the merging process was not proceeded. Finally, 3D reconstructions of the whole brain and the cerebellum from the segmented slices are displayed in Fig. 9.7(a) and Fig. 9.7(b). The 3D shading renderings were created using Interactive Data Language (IDL) software. Slicing of the total mouse brains in different directions led to results, equal within 1%; the volume quantifications for the cerebellum were equal within 3%. The operator variability was about 3%. Although gradient calibration limitations must also be taken into account, these results are satisfying in comparison to the volume measurements, obtained from invasive techniques (slicing of the fixated mouse head), where errors of more than 10% are common. This is mainly due to the fixation process, which leads to volume changes (shrinking or expansion). Similar errors are introduced when cutting the cerebellum from the rest of the brain and measuring the volume after immersion into a fluid. In addition, the proposed non-invasive segmentation techniques for volume quantization has this advantage over the invasive method that in-vivo studies can be performed, which allows the study of volume dynamics.
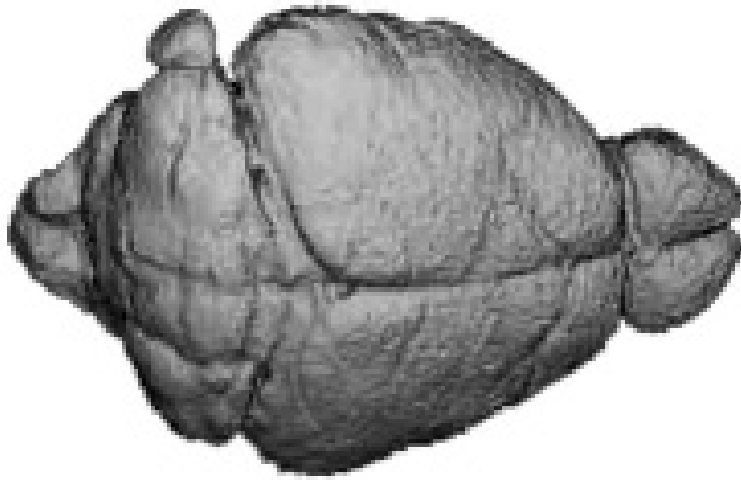
(a) Total mouse brains

(b) Mouse cerebellum

Figure 9.7: 3D reconstructions of the segmented objects.

Table 9.2: Segmentation results of mouse brain segmentation

Method	Number of volume elements	Number of man. interac. per slice	Total brain volume (mm^3)	Cerebellum volume (mm^3)
raw data	74053	17.1	559 ± 1	65.4 ± 1.4
after diff.filtering	23203	5.4	560 ± 2	64.0 ± 1.9
after merging	11601	2.6	559 ± 2	63.7 ± 2.1

Segmentation performance

3D adaptive anisotropic diffusion filtering with a 5×5×5 window took about 14 minutes. Calculation of the 3D watershed image took less than 4 minutes. Merging volume primitives required 9 minutes. Hence, all fully automatic preprocessing steps were completed within half an hour. Finally, the user interaction time, to extract the cerebellum from the rest of the image, took about 2.5 seconds per slice. The interactive segmentation for the cerebellum was completed within 7 minutes. The total brain was segmented within 11 minutes. Although far more volume elements were involved in the segmentation of the total brain, segmentation was less complex as the contrast between the total brain and the surroundings was higher. In general, the speed of segmentation depends very much on the clearness of the object boundary and in minor way on the shape of the object. Concerning the performance of the proposed segmentation procedure, some general conclusions can be drawn:

- The method obviously works best when the object of interest is delineated by a strong contour in the data.

- The segmentation performance depends on the deformation from one slice to the other: automation increases when the local deformation is smaller than the average size of a basic volume element. If this is a problem, a possible solution might be zero-filling of the raw data, thereby extrapolating between subsequent slices.

- Homogeneity within the object or convexity is not required.

- The influence of random noise on the segmentation performance can be managed as described in this paper. However, segmentation results will degrade when structured noise is present due to magnetic field inhomogeneities, object movement, etc.

9.4   Applications

The segmentation technique, described above, is currently used as a routine segmentation technique for 3D volume quantization. Below, two applications are described in which the segmentation technique, proposed in this chapter, was extensively applied.

Figure 9.8: 3D views of the segmented canary brain.

9.4.1   Fragile X knockout mice

Fragile X syndrome is the most frequent cause of inherited mental retardation. No specific pathological abnormalities have been described post mortem. However, with the aid of in-vivo MRI, performed on human brain, Reiss et al. showed a significantly decreased size of the posterior cerebellar vermis [101]. Recently, a transgenic mouse was developed with a loss-of-function (knockout) mutation in the FMR1. The mutant mice lack normal FMR1 mRNA and protein, as is also the case in human fragile X syndrome, and show cognitive and behavioural abnormalities comparable to those observed in humans. The purpose of the study of Verhoye et al. was to obtain quantitative MRI data from the mouse model [104, 105, 106]. In particular, the authors focussed on the size of the cerebellar vermis, as compared to the work performed on humans. Also, the application of 3D high resolution FSE MRI allowed an accurate and in-vivo determination of the volume of the cerebellum and the total brain. Despite accurate size measurements of the brain structures, results revealed no significant difference between knockouts and controls.

9.4.2   Canary brain

The volumes of song system nuclei in the brain of oscine birds (e.g., canaries) vary with season, sex and capacity for song learning. The brain is therefore considered as an excellent model for neural plasticity. However, using present techniques, volumes can only be measured once for a particular bird, after histology. By means of 3D FSE MRI microscopy and image post-processing brain structures could be mapped in a non-invasive and in-vivo manner. This was partially thanks to the accurate image segmentation. In addition, the combination of in vivo MRI microscopy and accurate image segmentation may allow experiments in which neuroanatomy of individuals is quantified, both before and after experimental treatments [107]. In Fig. (9.8) 3D views of the canary brain are shown.

9.5   Conclusions

In conclusion, a semiautomatic 3D segmentation technique was proposed, grounded on the immersion-based watershed algorithm. It was shown that preprocessing the data with a 3D adaptive anisotropic diffusion filter has a positive impact on the segmentation results. A posteriori merging of basic volume primitives additionally reduces the user interaction time. The proposed segmentation technique is successfully used to extract quantitative volume information from 3D images of in vitro as well as in vivo mouse and bird cerebella. It has proved to be superior in comparison with existing invasive methods.

Chapter 10

Conclusions

Magnetic resonance (MR) images are known to be polluted by various random as well as structured noise sources. The main contribution to random noise comes from thermal, white noise originating from the object to be imaged, as well as from the MR equipment. As thermal noise is characterized by a Gauss probability density function (PDF), the acquired complex, raw MR data are also Gauss distributed. However, in practice, MR data are non-linearly transformed into magnitude and/or phase MR data, which changes the PDF that characterize these data types. Throughout this work, the importance of incorporating the correct data PDF in various image processing tasks was emphasized.

One of these tasks concerns the estimation of the image noise variance (NV) or the noise standard deviation from magnitude MR images. Conventional techniques to estimate the NV from a single magnitude MR image, were discussed and compared to the Maximum Likelihood (ML) estimation method, as ML estimation is known to have optimal properties asymptotically. In addition, ML estimation is able to incorporate the PDF of magnitude MR data, which is the (generalized) Rice distribution, in an optimal way. It was shown that the mean squared error (MSE), which is inversely related to the combined precision and accuracy of an estimator, was smallest for the proposed ML estimator.
Concerning the estimation of the image noise variance, methods, based on a double acquisition, are far superior to single image techniques in terms of precision. However, existing double acquisition methods become useless when different phase variations are present in the two images. To overcome this problem, a noise variance estimation method has been proposed, based on two magnitude MR images. Under the condition of geometrical registration, the proposed noise variance estimator has been shown to be highly precise and accurate.

In addition, the problem of signal estimation from magnitude (generalized) Rice distributed MR data was addressed. It was shown that conventional signal estimation techniques yield biased results, as the knowledge of the (generalized) Rice distribution was not fully exploited. Again, a Maximum Likelihood estimator was proposed, which was shown to outperform the conventional methods with respect to accuracy. The usefulness of the proposed ML signal estimator is demonstrated in the problem of estimating T_1- and T_2-maps from magnitude MR data.

Beside the estimation of signal and noise, attention has been paid to the estimation and improvement of the image signal-to-noise ratio (SNR). A new double acquisition method, based on cross-correlation, was proposed for the estimation of the SNR, which can be implemented in a highly efficient way in most MR acquisition schemes.
Furthermore, it was shown that cross-correlation of two acquisitions of the same image can as well be used to improve the image SNR. However, the advantages of significant SNR improvement and ease of implementation are compromised by loss of spatial resolution. Therefore, in this thesis the anisotropic

adaptive diffusion filter was discussed, which is capable of increasing the image SNR significantly while retaining the spatial resolution and hence the image details amazingly well.

Finally, a semi-automatic 3D segmentation technique was proposed, grounded on the immersion based watershed algorithm. It was shown that preprocessing the data with a 3D adaptive anisotropic diffusion filter had a positive impact on the segmentation results. The proposed segmentation technique is successfully used to extract quantitative volume information from 3D images of in vitro as well as in vivo biological objects. It has proved to be superior in comparison with existing invasive methods. The technique is currently implemented as a routine segmentation procedure for 3D volume quantization.

Bibliography

[1] F. Bloch. Nuclear induction. *Physical Review*, 70:460–474, 1946.

[2] E. M. Purcell, H. C. Torrey, and R. V. Pound. Resonance absorption by nuclear magnetic moments in a solid. *Physical Review*, 69:37, 1946.

[3] P. C. Lauterbur. Image formation by induced local interactions: examples employing nuclear magnetic resonance. *Nature*, 242:190, 1973.

[4] P. Slichter. *Principles of Magnetic Resonance*. Springer, New York, 3rd edition, 1996.

[5] P. T. Callaghan. *Principles of Nuclear Magnetic Resonance Microscopy*. Clarendon Press, Oxford, 2nd edition, 1995.

[6] A. Abragam. *The principles of nuclear magnetism*. Clarendon Express, Oxford, 1961.

[7] P. Mansfield and P. K. Grannell. *Journal of Physics C*, 6:L422, 1973.

[8] D. I. Hoult and R. E. Richards. The signal-to-noise ratio of the nuclear magnetic resonance experiment. *Journal of Magnetic Resonance*, 24:71–85, 1976.

[9] W. A. Edelstein, P. A. Bottomley, H. R. Hart, and L. S. Smith. Signal, noise, and contrast in nuclear magnetic resonance (NMR) imaging. *Journal of Computer Assisted Tomography*, 7(3):391–401, 1983.

[10] J. P. Mugler and J. R. Brookeman. The optimum data sampling period for maximum signal-to-noise in MR imaging. *Reviews of Magnetic Resonance in Medicine*, 3(1):1–51, 1988.

[11] F. R. Connor. *Noise*. Edward Arnold, London, 2nd edition, 1982.

[12] L. Breiman. *Probability*. Addison-Wesley, Reading, Massachusetts, 1968.

[13] D. I. Hoult and P. C. Lauterbur. The sensitivity of the zeugmatographic experiment involving human samples. *Journal of Magnetic Resonance*, 34:425–433, 1979.

[14] P. G. Morris. *Nuclear Magnetic Resonance in Medicine and Biology*. Clarendon Press, Oxford, 1986.

[15] J. M. Libove and J. R. Singer. Resolution and signal-to-noise relationships in NMR imaging in the human body. *Journal of Physics, E: Scientific Instruments*, 13:38–44, 1980.

[16] D. L. Parker and G. T. Gullberg. Signal-to-noise eficiency in magnetic resonance imaging. *Medical Physics*, 17(2):250–257, 1990.

[17] E. M. Bellon, E. M. Haacke, P. E. Coleman, D. C. Sacco, D. A. Steiger, and R. E. Gangarosa. MR artifacts: A review. *The American Journal of Roentgenology*, 147:1271–1281, 1986.

[18] S. O. Rice. Mathematical analysis of random noise. *Bell System Technological Journal*, 23:282, 1944.

[19] R. M. Henkelman. Measurement of signal intensities in the presence of noise in MR images. *Medical Physics*, 12(2):232–233, 1985.

[20] A. H. Andersen and J. E. Kirsch. Analysis of noise in phase contrast MR imaging. *Medical Physics*, 23(6):857–869, 1996.

[21] Y. Wang and T. Lei. Statistical analysis of MR imaging and its applications in image modeling. In *Proceedings of the IEEE International Conference on Image Processing and Neural Networks*, volume I, pages 866–870, 1994.

[22] A. Van den Bos. Estimation of Fourier coefficients. *IEEE transactions on instrumentation and measurement*, 38(4):1005–1007, 1989.

[23] S. Ross. *A first course in probability*. Collier Macmillan Publishers, New York, 1976.

[24] M. Abramowitz and I. A. Stegun. *Handbook of mathematical functions*. Dover Publications, New York, 1970.

[25] I. S. Gradshteyn and I. M. Ryzhik. *Table of integrals, series and products*. Academic Press, New York and London, 4th edition, 1965.

[26] C. D. Constantinides, E. Atalar, and E. R. McVeigh. Signal-to-noise measurements in magnitude images from NMR phased arrays. *Magnetic Resonance in Medicine*, 38:852–857, 1997.

[27] N. J. Pelc, M. A. Bernstein, A. Shimakawa, and G. H. Glover. Encoding strategies for three-direction phase-contrast MR imaging of flow. *Journal of Magnetic Resonance Imaging*, 1(4):405–413, 1991.

[28] H. Gudbjartsson and S. Patz. The Rician distribution of noisy MRI data. *Magnetic Resonance in Medicine*, 34:910–914, 1995.

[29] S. J. Garnier and G. L. Bilbro. Magnetic resonance image restoration. *Journal of Mathematical Imaging and Vision*, 5:7–19, 1995.

[30] M. R. Banham and A. K. Katsaggelos. Digital image restoration. *IEEE signal processing magazine*, 3:24–41, 1997.

[31] G. Z. Yang, P. Burger, D. N. Firmin, and S. R. Underwood. Structure adaptive anisotropic filtering for magnetic resonance image enhancement. In *Proceedings of CAIP: Computer Analysis of Images and Patterns*, pages 384–391, 1995.

[32] G. Gerig, O. Kubler, R. Kikinis, and F. A. Jolesz. Nonlinear anisotropic filtering of MRI data. *IEEE Transactions on Medical Imaging*, 11(2):221–232, 1992.

[33] S. I. Olsen. Estimation of noise in images: an evaluation. *Graphical Models and Image Processing*, 55(4):319–323, 1993.

[34] R. A. Close and J. S. Whiting. Maximum likelihood technique for blind noise estimation. In *Proceedings of SPIE Medical Imaging*, volume 2708, pages 18–28, Newport Beach CA, 1996.

[35] R. Bracho and A. C. Sanderson. Segmentation of images based on intensity gradient information. In *Proceedings of the CVPR-85 Conference on Computer Vision and Pattern Recognition*, pages 341–347, San Francisco, CA, 1985.

[36] J. S. Lee. Refined filtering of image noise using local statistics. *Computational Vision Graphics and Image Processing*, 15:380–389, 1981.

[37] G. A. Mastin. Adaptive filters for digital image smoothing, an evaluation. *Computational Vision Graphics and Image Processing*, 31:103–121, 1985.

[38] J. S. Lee and K. Hoppel. Noise modeling and estimation of remotely-sensed images. In *Proceedings of 1989 International Geoscience and Remote Sensing*, volume 2, pages 1005–1008, Vancouver, 1989.

[39] P. Meer, J. Jolion, and A. Rosenfeld. A fast parallel algorithm for blind noise estimation of noise variance. *IEEE Transactions on Pattern Analysis and Machine Intelligence*, 12(2):216–223, 1990.

[40] L. Kaufman, D. M. Kramer, L. E. Crooks, and D. A. Ortendahl. Measuring signal-to-noise ratios in MR imaging. *Radiology*, 173:265–267, 1989.

[41] R.L. Dixon, editor. *MRI: Acceptance Testing and Quality Control - The Role of the Clinical Medical Physicist*, Madison, Wisconsin, April 1988. Medical Physics Publishing Corporation.

[42] B. W. Murphy, P. L. Carson, J. H. Ellis, Y. T. Zhang, R. J. Hyde, and T. L. Chenevert. Signal-to-noise measures for magnetic resonance imagers. *Magnetic Resonance Imaging*, 11:425–428, 1993.

[43] J. Sijbers, A. J. den Dekker, M. Verhoye, J. Van Audekerke, and D. Van Dyck. Estimation of noise from magnitude MR images. *Magnetic Resonance Imaging*, 16(1):87–90, 1998.

[44] R. A. Fisher. On the mathematical foundations of theoretical statistics. *Phylosophical Transactions on the Royal Society of London, Series A*, 222:309–368, 1922.

[45] R. A. Fisher. Theory of statistical estimation. *Proceedings of the Cambridge Phylosophical Society*, 22:700–725, 1925.

[46] A. Van den Bos. *Handbook of Measurement Science*, volume 1, chapter 8: Parameter Estimation, pages 331–377. Edited by P.H. Sydenham, Wiley, Chichester, England, 1982.

[47] A. Stuart and K. Ord. *Kendall's advanced theory of statistics*. Arnold, London, 1994.

[48] A. M. Mood, F. A. Graybill, and D. C. Boes. *Introduction to the Theory of Statistics*. McGraw-Hill, Tokyo, 3$^{\mathrm{rd}}$ edition, 1974.

[49] M. A. Bernstein, D. M. Thomasson, and W. H. Perman. Improved detectability in low signal-to-noise ratio magnetic resonance images by means of phase-corrected real construction. *Medical Physics*, 16(5):813–817, 1989.

[50] G. McGibney and M. R. Smith. An unbiased signal-to-noise ratio measure for magnetic resonance images. *Medical Physics*, 20(4):1077–1078, 1993.

[51] A. J. Miller and P. M. Joseph. The use of power images to perform quantitative analysis on low SNR MR images. *Magnetic Resonance Imaging*, 11:1051–1056, 1993.

[52] J. Sijbers, A. J. den Dekker, D. Van Dyck, and E. Raman. Estimation of signal and noise from Rician distributed data. In *Proceedings of the International Conference on Signal Processing and Communications*, pages 140–142, Gran Canaria, Canary Islands, Spain, February 1998.

[53] B. Efron. *The Jackknife, the Bootstrap, and Other Resampling Plans*, volume 38 of *CBMS-NSF Regional Conference Series in Applied Mathematics*. Society for Industrial and Applied Mathematics, Philadelphia, 1982.

[54] T. Poston and I. N. Stewart. *Catastrophe Theory and its Applications*. Pitman, London, 1980.

[55] W. H. Press, W. T. Vettering, S. A. Teukolsky, and B. P. Flannery. *Numerical Recipes in C*. University Press, Cambridge, 1994. Chap. 10.

[56] J. Liu, A. Nieminen, and J. L. Koenig. Calculation of T_1, T_2 and proton spin density in nuclear magnetic resonance imaging. *Journal of Magnetic Resonance*, 85:95–110, 1989.

[57] J. M. Bonny, M. Zanca, J. Y. Boire, and A. Veyre. T_2 maximum likelihood estimation from multiple spin-echo magnitude images. *Magnetic Resonance in Medicine*, 36:287–293, 1996.

[58] P. S. Tofts and A. G. Kermode. Measurement of blood-brain barrier permeability and leakage space using dynamic MR imaging. *Magnetic Resonance in Medicine*, 17:357–367, 1991.

[59] P. S. Tofts, B. Berkowitz, and M. D. Schnall. Quantitative analysis of dynamic Gd-DTPA enhancement in breast tumors using a permeability model. *Magnetic Resonance in Medicine*, 33:564–568, 1995.

[60] D. Artemov and Z. M. Bhujwalla. Three dimensional MRI quantification of tumour vascular volume and permeability. In *Proceedings of the International Society of Magnetic Resonance in Medicine (Nr. 491)*, Vancouver, April 1997.

[61] J. Sijbers, P. Scheunders, N. Bonnet, D. Van Dyck, and E. Raman. Quantification and improvement of the signal-to-noise ratio in a magnetic resonance image acquisition procedure. *Magnetic Resonance Imaging*, 14(10):1157–1163, 1996.

[62] R. R. Price, L. Axel, T. Morgan, R. Newman, W. Perman, N. Schneiders, M. Selikson, M. Wood, and S. R. Thomas. Quality assurance methods and phantoms for magnetic resonance imaging: report of AAPM nuclear magnetic resonance task group No. 1a. *Medical Physics*, 17(2):287–295, 1990.

[63] R. M. Henkelman. Erratum: Measurement of signal intensities in the presence of noise in MR images. *Medical Physics*, 13(4):544, 1986.

[64] W. A. Edelstein, P. A. Bottomley, and L. M. Pfeifer. A signal-to-noise calibration procedure for NMR imaging systems. *Medical Physics*, 11(2):180–185, 1984.

[65] F. Lenz. *Electron Microscopy in Material Science*. Academic, London, 1971.

[66] J. Frank and L. Al-Ali. Signal-to-noise ratio of electron micrographs obtained by cross correlation. *Nature*, 256:376–379, 1975.

[67] N. Bonnet, S. Lebonvallet, H. El Hila, G. Colliot, and A. Beorchia. Quantitative evaluation of the signal-to-noise ratio and of its improvement (or degradation) by digital filters. *Journal of Physics III*, 1:1349–1358, 1991.

[68] A. Papoulis. *Probability, Random Variables and Stochastic Processes*. McGraw-Hill, Tokyo, Japan, 2nd edition, 1984.

[69] E. R. McVeigh, R. M. Henkelman, and M. J. Bronskil. Noise and filtration in magnetic resonance imaging. *Medical Physics*, 12(5):586–591, 1985.

[70] D. L. Parker, G. T. Gullberg, and P. R. Frederick. Gibbs artifact removal in magnetic resonance imaging. *Medical Physics*, 14(4):640–645, 1987.

[71] M. Fuderer. The information content of MR images. *IEEE Transactions on Medical Imaging*, 7(4):368–380, 1988.

[72] I. Daubechies. Orthonormal bases of compactly supported wavelets. *Communications on Pure and Applied Mathematics*, 41(7):909–996, 1988.

[73] J. B. Weaver, Y. Xu, D. M. Healy, and L. D. Cromwell. Filtering noise from images with wavelet transforms. *Magnetic Resonance in Medicine*, 21:288–295, 1991.

[74] P. Saint-Marc, J. S. Chen, and G. Medioni. Adaptive smoothing: A general tool for early vision. *IEEE Transactions on Pattern Analysis and Machine Intelligence*, 12:629–639, 1990.

[75] K. Ying, B. D. Clymer, and P. Schmalbrock. Adaptive filtering processing of magnetic resonance images. In *Proceedings of the Society of Magnetic Resonance, 2nd meeting;*, page 803, 1994.

[76] P. Perona and J. Malik. Scale space and edge detection using anisotropic diffusion. *IEEE Transactions on Pattern Analysis and Machine Intelligence*, 12(7):629–639, 1990.

[77] J. Weickert. Multiscale texture enhancement. In Radim Sara Vaclav Hlavac, editor, *Proceedings of CAIP: Computer Analysis of Images and Patterns*, pages 230–237, Prague, Czech Republic, September 1995.

[78] O. Nalcioglu and C. H. Cho. Limits to signal-to-noise improvement by FID averaging in NMR imaging. *Physics in Medicine and Biology*, 29(8):969–978, 1984.

[79] N. Bonnet. On the use of correlation functions for improving the image signal-to-noise ratio. *Optik*, 80(3):103–106, 1988.

[80] A. J. Den Dekker. *Model based resolution.* PhD thesis, Technische Universiteit Delft, 1997.

[81] L. P. Clarke, R. P. Velthuizen, M. A. Camacho, J. J. Heine, M. Vaidyanathan, L. O. Hall, R. W. Thatcher, and M. L. Silbiger. MRI segmentation: Methods and applications. *Magnetic Resonance Imaging*, 13(3):343–368, 1995.

[82] H. Suzuki and J. Toriwaki. Automatic segmentation of head MRI images by knowledge guided thresholding. *Computerized Medical Imaging and Graphics*, 15:233–240, 1991.

[83] K. O. Lim and A. Pfefferbaum. Segmentation of MR brain images into cerebrospinal fluid spaces, white and gray matter. *Journal of Computational Assistant Tomography*, 13(4):588–593, 1989.

[84] A. Kundu. Local segmentation of biomedical images. *Computerized Medical Imaging and Graphics*, 14:173–183, 1990.

[85] M. Bomans, K. H. Hohne, U. Tiede, and M. Riemer. 3D segmentation of MR images of the head for 3D display. *IEEE Transactions on Medical Imaging*, 9:177–183, 1990.

[86] M. Ashtari, J. L. Zito, B. I. Gold, J. A. Lieberman, M. T. Borenstein, and P. G. Herman. Computerized measurement of brain structure. *Investigations on Radiolology*, 25:798–805, 1990.

[87] S. Dellepiane. Image segmentation: Errors, sensitivity and uncertainty. *Proceedings of the 13th IEEE-Engineering of Medical Biological Society*, 13:253–254, 1994.

[88] G. Gerig, J. Martin, R. Kikinis, O. Kubler, M. Shenton, and F. A. Jolesz. Unsupervised tissue type segmentation of 3D dual-echo MR head data. *Image and Vision Computing*, 10:346–360, 1992.

[89] L. O. Hall, A. M. Bensaid, L. P. Clarke, R. P. Velthuizen, M. S. Silbiger, and J. C. Bezdek. A comparison of neural network and fuzzy clustering techniques in segmenting magnetic resonance images of the brain. *IEEE Transactions on Neural Networks*, 3:672–682, 1992.

[90] S. Geman and D. Geman. Stochastic relaxation, Gibbs distribution and the Bayesian restoration of images. *IEEE Transactions on Pattern Analalysis and Machine Intelligence*, 6(6):721–741, 1984.

[91] T. N. Pappas. An adaptive clustering algorithm for image segmentation. *IEEE Transactions on Signal Processing*, SP-40:901–914, 1992.

[92] J. C. Bezdek, L. O. Hall, and L. P. Clarcke. Review of MR image segmentation techniques using pattern recognition. *Medical Physics*, 20:1033–1048, 1993.

[93] J. Sijbers, P. Scheunders, M. Verhoye, A. Van der Linden, D. Van Dyck, and E. Raman. Watershed-based segmentation of 3D MR data for volume quantization. *Magnetic Resonance Imaging*, 15(6):679–688, 1997.

[94] L. Vincent and P. Soille. Watersheds in digital spaces: An efficient algorithm based on immersion simulations. *IEEE Transactions on Pattern Analysis and Machine Intelligence*, 13(6):583–593, 1991.

[95] D. Hagyard, M. Razaz, and P. Atkin. Analysis of watershed algorithms for greyscale images. In *Proceedings of the IEEE International Conference on Image Processing*, volume 3, pages 41–44, 1996.

[96] F. Maes, D. Vandermeulen, P. Suetens, and P. Marchal. Automatic image partitioning for generic object segmentation in medical images. In *Proceedings of the 14th International Conference on Image Processing in Medical Imaging*, pages 215–226, 1995.

[97] T. M. Cover and J. A. Thomas. *Elements of Information Theory*. John Wiley and Sons, New York, 1991.

[98] J. Rissanen. *Minimum Description Length Principle*, volume 5 of *Encyclopaedia of Statistical Sciences*. Wiley, New York, 1987.

[99] Y. G. Leclerc. Constructing simple stable descriptions for image partitioning. *International Journal of Computer Vision*, 3:73–102, 1989.

[100] B. W. Silverman. *Density Estimation for Statistics and Data Analysis*. Chapman and Hall, London, 1986.

[101] A. L. Reiss, L. Freund, J. E. Tseng, and P. K. Joshi. Neuroanatomy in fragile X females: The posterior fossa. *American Journal of Human Genetics*, 49:279–288, 1991.

[102] E. Courchesne, R. Yeung-Courchesne, G. A. Press, J. R. Hesselink, and T. L. Jernigan. Hypoplasia of cerebellar vermal lobules VI and VII in autism. *The New England Journal of Medicine*, 318(21):1349–1358, 1988.

[103] The Dutch-Belgian Fragile X Consortium. Fmr1 knockout mice: A model to study fragile X mental retardation. *Cell*, 78:23–33, 1994.

[104] M. Verhoye, A. Van der Linden, J. Sijbers, P. Scheunders, D. Van Dyck, E. Reniers, R.F. Kooy, P.J. Willems, P. Cras, and B.A. Oostra. High resolution MRI study of the cerebellum of mice as a function of age, in a mouse model for fragile X mental retardation. In 13th *Annual Meeting of the European Society for Magnetic Resonance in Medicine and Biology*, volume IV (II), page 168, Prague, September 1996.

[105] M. Verhoye, J. Sijbers, P. Scheunders, D. Van Dyck, E. Reniers, R.F. Kooy, P.J. Willems, P. Cras, B.A. Oostra, and A. Van der Linden. In vivo assessment of cerebellum volume in transgenic fragile X knockout mice using MRI microscopy at 7T. In 14th *Annual Meeting of the European Society for Magnetic Resonance in Medicine and Biology*, volume 5(2), pages 45–46, Brussels, September 1997.

[106] M. Verhoye, J. Sijbers, R. F. Kooy, E. Reyniers, E. Fransen, B. B. Oostra, P. Willems, and A. Van der Linden. MRI as a tool to study brain structure from mouse models of mental retardation. In *Proceedings of SPIE Medical Imaging'98*, volume 3337, pages 314–320, San Diego, CA, USA, February 1998.

[107] J. Van Audekerke, M. Verhoye, J. Sijbers, T. J. DeVoogd, T. Smulders, S. W. Newman, and A. Van der Linden. Imaging birds $\cdots$ in a bird cage: In vivo MRI microscopy of the canary brain at 7T. In *Proceedings of Magnetic Resonance Materials in Physics, Biology, and Medicine*, volume V (II), pages 162–163, September 1997.

Appendix A

The generalized Rice PDF

In this appendix, the generalized Rice probability density function (PDF) is derived, which characterizes magnitude phase contrast magnetic resonance (PCMR) data. In the first section, the PDF of one PCMR pixel variable is derived, which was previously also deduced by Andersen and Kirsch [20]. Based on that PDF, in the second section, the PDF of a spatial average of a number of squared PCMR pixel variables is deduced.

A.1 PDF of one PCMR pixel variable

PCMR data are obtained by computing the square root of the sum of squared independent variables $\{x_k\}$:

$$M = \sqrt{\sum_{k=1}^{K} x_k^2} \quad , \tag{A.1}$$

where x_k is assumed to be Gauss distributed with variance σ^2 and mean a_k:

$$p_{x_k}(x_k) = \frac{1}{\sqrt{2\pi\sigma^2}} \exp\left(-\frac{(a_k - x_k)^2}{2\sigma^2}\right) \quad . \tag{A.2}$$

As a first step, we derive the PDF of x_k^2 from its characteristic function:

$$\Phi_{x_k^2}(\omega) = E\left[e^{i\omega x_k^2}\right] \tag{A.3}$$

$$= \frac{1}{\sqrt{2\pi\sigma^2}} \int_{-\infty}^{\infty} e^{i\omega x_k^2} e^{-\frac{(x_k - a_k)^2}{2\sigma^2}} dx_k \tag{A.4}$$

$$= \frac{e^{-\frac{a_k^2}{2\sigma^2}}}{\sqrt{2\pi\sigma^2}} \int_{-\infty}^{\infty} e^{-\left(\frac{1}{2\sigma^2} - i\omega\right)x_k^2} e^{\frac{a_k x_k}{\sigma^2}} dx_k \quad . \tag{A.5}$$

The integral is the two-side Laplace transform of a Gauss function with complex "variance" $(1/2\sigma^2 - i\omega)^{-1}$, evaluated at $x_k = a_k/\sigma^2$:

$$\Phi_{x_k^2}(\omega) = \frac{e^{-\frac{a_k^2}{2\sigma^2}}}{\sqrt{2\sigma^2(1/2\sigma^2 - i\omega)}} e^{\frac{(a_k/2\sigma^2)^2}{1/2\sigma^2 - i\omega}} \tag{A.6}$$

$$= \frac{1}{\sqrt{1 - 2i\omega\sigma^2}} \exp\left(\frac{i\omega a_k^2}{1 - 2i\omega\sigma^2}\right) \quad . \tag{A.7}$$

Now, consider the sum y of K squared Gauss distributed variables $\{x_k\}$:

$$y = M^2 = \sum_{k=1}^{K} x_k^2 \quad . \tag{A.8}$$

When all x_k's are statistically independent random variables, the characteristic function of y is simply the product of the characteristic functions of $\{x_k\}$:

$$\Phi_y(\omega) = \prod_{k=1}^{K} \Phi_{x_k^2}(\omega) \tag{A.9}$$

$$= \frac{1}{(1 - 2i\omega\sigma^2)^{K/2}} \exp\left(\frac{i\omega A^2}{1 - 2i\omega\sigma^2}\right) \quad , \tag{A.10}$$

where A denotes the deterministic signal component, i.e., the vector magnitude of the means of the individual random variables $\{x_k\}$:

$$A = \sqrt{\sum_{k=1}^{K} a_k^2} \quad . \tag{A.11}$$

The PDF of y in turn can be found as the inverse Fourier transform of its associated characteristic function $\Phi_y(\omega)$:

$$p_y(y) = \frac{1}{2\pi} \int_{-\infty}^{\infty} \frac{e^{i\omega A^2/(1-2i\omega\sigma^2)}}{(1 - 2i\omega\sigma^2)^{K/2}} e^{-i\omega y} d\omega \quad . \tag{A.12}$$

Substituting $s = 1 - 2i\omega\sigma^2$, Eq. (A.12) becomes a Laplace transform:

$$p_y(y) = \frac{1}{2\pi} \frac{i}{2\sigma^2} \int_{1+i\infty}^{1-i\infty} \frac{e^{A^2(1-s)/2\sigma^2}}{s^{K/2}} e^{-y(1-s)/2\sigma^2} ds \tag{A.13}$$

$$= \frac{e^{-(y+A^2)/2\sigma^2}}{2\sigma^2} \frac{1}{2\pi i} \int_{1-i\infty}^{1+i\infty} \frac{e^{A^2/(2s\sigma^2)}}{s^{K/2}} e^{sy/2\sigma^2} ds \quad . \tag{A.14}$$

From tables of Laplace transforms [24], we finally obtain:

$$p_y(y) = \frac{1}{2\sigma^2} \left(\frac{y}{A^2}\right)^{\frac{K-2}{4}} \exp\left(-\frac{y + A^2}{2\sigma^2}\right) I_{\frac{K}{2}-1}\left(\frac{\sqrt{y}A}{\sigma^2}\right) \epsilon(y) \quad . \tag{A.15}$$

From the PDF of y, it is now easy to derive the PDF of the magnitude variable, given in Eq. (A.1) [68]:

$$p_M(M) = 2M p_y(M^2) \quad , \tag{A.16}$$

or explicitly:

$$p_M(M) = \frac{M}{\sigma^2} \left(\frac{M}{A}\right)^{\frac{K}{2}-1} \exp\left(-\frac{M^2 + A^2}{2\sigma^2}\right) I_{\frac{K}{2}-1}\left(\frac{MA}{\sigma^2}\right) \epsilon(M) \quad , \tag{A.17}$$

which is called the generalized Rice PDF.

A.2 PDF of the average of squared PCMR pixel variables

As was deduced in the previous section, the PDF of a PCMR pixel variable M_i at spatial position i is given by:

$$p_{M_i}(M_i) = \frac{M_i}{\sigma^2} \left(\frac{M_i}{A}\right)^{\frac{K}{2}-1} \exp\left(-\frac{M_i^2 + A^2}{2\sigma^2}\right) I_{\frac{K}{2}-1}\left(\frac{M_i A}{\sigma^2}\right) \epsilon(M_i) \quad , \tag{A.18}$$

where it is assumed that the deterministic signal component of all M_i's is A, given in Eq. (A.11). We now derive the PDF of a spatial average over N squared, independent PCMR pixel variables M_i. The average will be written as:

$$\langle M^2 \rangle \quad = \quad \frac{1}{N} \sum_{i=1}^{N} M_i^2 \tag{A.19}$$

$$= \quad \frac{1}{N} \sum_{i=1}^{N} \sum_{k=1}^{K} x_{i,k}^2 \quad . \tag{A.20}$$

Again, consider first the variable y, where

$$y = \sum_{i=1}^{N} M_i^2 = \sum_{i=1}^{N} \sum_{k=1}^{K} x_{i,k}^2 \quad . \tag{A.21}$$

If summation is over a region where the signal component is constant, y is a sum of N times K squared Gauss distributed variables with NA^2 as deterministic signal component (cfr. Eq. A.11). Then, from Eq. (A.18) the PDF of y becomes:

$$p_y(y) = \frac{1}{2\sigma^2} \left(\frac{y}{NA^2} \right)^{\frac{NK-2}{4}} \exp \left(-\frac{y + NA^2}{2\sigma^2} \right) I_{\frac{NK}{2}-1} \left(\frac{\sqrt{y}NA}{\sigma^2} \right) \epsilon(y) \quad . \tag{A.22}$$

Finally, because

$$p_{\langle M^2 \rangle} \left(\langle M^2 \rangle \right) = N p_y \left(N \langle M^2 \rangle \right) \tag{A.23}$$

we obtain the PDF of $\langle M^2 \rangle$:

$$p_{\langle M^2 \rangle} \left(\langle M^2 \rangle \right) = \frac{N}{2\sigma^2} \left(\frac{\langle M^2 \rangle}{A^2} \right)^{\frac{NK-2}{4}} \exp \left(-N \frac{\langle M^2 \rangle + A^2}{2\sigma^2} \right) I_{\frac{NK}{2}-1} \left(\frac{\sqrt{\langle M^2 \rangle}NA}{\sigma^2} \right) \epsilon \left(\langle M^2 \rangle \right) \quad . \tag{A.24}$$

Appendix B

List of symbols and abbreviations

B.1 Greek symbols

α	excitation flip angle
γ	gyromagnetic ratio
Γ	Gamma function
$\delta(.)$	Dirac delta function
$\epsilon(.)$	unit step Heaviside function
λ_i	i^{th} matrix eigenvalue
μ	magnetic moment of the proton
ρ	pseudo proton density
ρ_m	population of the substate with magnetic quantum number m
σ	standard deviation
σ^2	variance
σ_n	noise standard deviation
θ	arbitrary function of ρ, T_1 and T_2
Φ	phase value
$\Delta\Phi$	phase difference
ω_0	angular Larmor frequency related to B_0 via: $\omega_0 = \gamma B_0$
Ω	local neighbourhood

B.2   Roman symbols

a_{ij}	anisotropy coefficients
$\hat{A}_c$	conventional signal estimator
$\hat{A}_{ML}$	maximum likelihood signal estimator
B_0	main magnetic induction
B_1	magnetic induction produced by an RF coil
$E[.]$	expectation operator
$_1F_1$	confluent hypergeometric function
G_x	gradient field strength in the x direction
G_y	gradient field strength in the y direction
$h()$	filter kernel
$\hbar$	Planck's constant
I	proton spin
I_k	k^{th} order modified bessel function of the first kind.
FOV_x	field of view in the x direction
FOV_y	field of view in the y direction
k_b	Boltzman's constant
k_x	x coordinate of a K-space data point
k_x	y coordinate of a K-space data point
K	number of flow encoding directions
l	conductor length
L	coil inductance
m	magnetic quantum number
M	magnitude variable
M_0	magnetization per unit volume
N	number of data points
N_{av}	number of averages
N_s	number of spins of the sample per unit volume
N_x	number of samples in the x direction
N_y	number of samples in the y direction
p	conductor circumference
$\vec{r}$	spatial coordinate vector
R_c	coil resistivity
t	time variable
S_n	noise spectrum
T_1	spin-lattice relaxation constant
T_2	spin-spin relaxation constant
T_c	coil temperature
T_s	sample temperature
V_s	sample volume

B.3 Abbreviations

3D	three dimensional
ACF	auto correlation function
ANOVA	analysis of variance
CCC	cross correlation coefficient
CCF	cross correlation function
CNR	contrast to noise ratio
CR	Cramér Rao
CRLB	Cramér Rao lower bound
DC	direct current
FID	free induction decay
FLASH	fast low angle shot
FOV	field of view
FSE	fast spin echo
FT	Fourier transformation
FFT	Fast Fourier transformation
GE	gradient echo
HP	Hewlett Packard
IR	inversion recovery
LF	likelihood function
LS	least squares
IDL	Interactive Data Language
ML	maximum likelihood
MR	magnetic resonance
MRI	magnetic resonance imaging
MSE	mean squared error
MVB	minimum variance bound
NA	number of averages
NEMA	National Electrical Manufacturers Association
NMR	Nuclear magnetic resonance
NV	noise variance
PCMR	phase contrast magnetic resonance
PD	probability distribution
PDF	probability density function
RF	radio frequent
RMS	root mean squared
ROI	region of interest
SD	standard deviation
SE	spin echo
SMIS	Surrey medical imaging systems
SNR	signal to noise ratio
SRV	signaal/ruis verhouding
TE	echo time
TI	inversion time
TR	repetition time
WDF	waarschijnlijkheidsdichtheidsfunctie
WLS	weighted least squares

Appendix C

Nederlandse samenvatting

Dit proefwerk handelt in het algemeen over het schatten van ruis en signaal van Magnetische Resonantie (MR) data, waarbij de nadruk wordt gelegd op de bewerking van magnitude MR beelden. Verder worden een aantal onderwerpen behandeld die sterk gerelateerd zijn aan het schatten van ruis en signaal: het schatten en verbeteren van de signaal/ruis verhouding. Tenslotte wordt nog een semi-automatisch algoritme beschreven voor de segmentatie van 3D MR data.

Na een korte introductie, waarin de basisprincipes van MR beeldvorming worden toegelicht, wordt er in hoofdstuk 2 een overzicht gegeven van de oorsprong en de statistische eigenschappen van MR ruis en signaal. De magnetisatieverdeling welke men zou bekomen bij stationaire opname condities en een oneindig lange opnametijd wordt beschouwd als het (deterministisch) signaal. Random afwijkingen t.o.v. dit signaal worden beschouwd als ruis. De ruis blijkt voornamelijk zijn oorsprong te vinden in de warmte van het beeldvormend systeem en van het te beeldvormen object. Deze 'thermische ruis' genereert random signalen in de ontvanger en kan beschreven worden met een Gaussische waarschijnlijkheidsverdeling. Het eerste moment van deze Gauss verdeling is nul terwijl het tweede moment gelijk is aan de variantie van de ruis. De verhouding van de grootte van het signaal ten opzichte van de standaard afwijking van de ruis wordt gedefinieerd als de signaal/ruis verhouding (SRV).

Om data op een wetenschappelijk verantwoorde manier te verwerken, is kennis van de onderliggende waarschijnlijkheidsdichtheidsfunctie (WDF) onontbeerlijk. Om die reden worden in hoofdstuk 3 de waarschijnlijkheidsverdelingen van al dan niet bewerkte MR data afgeleid en besproken. Zoals reeds vermeld, zijn de in de K-ruimte bemonsterde, complexe MR data Gaussisch verdeeld. Na een Fourier reconstructie blijft de verdeling van de complexe data Gaussisch vanwege de ortogonaliteit en de lineariteit van de Fourier transformatie. In de praktijk wordt er nu, eerder dan met complexe data, veelal met magnitude en fase data gewerkt gezien deze data rechtstreeks gerelateerd kunnen worden aan fysische grootheden zoals de peudo-protondichtheid, stroming, diffusie, e.a. Het berekenen van magnitude en/of fase data is echter een niet-lineaire transformatie. Dit heeft voor gevolg dat de verdeling van zulke data niet meer gekarakteriseerd wordt door een Gaussische WDF maar, in het geval van magnitude data, door een Rice WDF. Fig. 3.1 op pagina 10 toont de Rice verdeling als functie van de signaal/ruis verhouding (SRV). Bij zeer lage SRV benadert de Rice verdeling een Rayleigh verdeling. Deze verdeling karakteriseert de signaal-loze achtergrond in een magnitude MR beeld. Bij zeer hoge SRV benadert de Rice verdeling een Gaussische verdeling. Zoals uit de volgende hoofdstukken zal blijken, speelt de WDF van de data een belangrijke rol bij het oplossen van schattingsproblemen. Steunend op Fig. 3.1 kan men dan ook reeds verwachten dat schattingsmethodes, welke gebaseerd zijn op Gaussisch verdeelde data, enkel op magnitude MR data toegepast mogen worden wanneer de SRV in het beeld erg hoog is.

Naast de WDF van magnitude MR data worden de WDF's van fase-contrast magnitude MR data en fase MR data afgeleid en besproken.

De schattingsproblemen die in dit proefwerk worden beschreven, omvatten het bepalen van ruis en signaal uit magnitude MR data welke besproken worden in respectievelijk hoofdstuk 4 en 5. In magnitude MR beelden wordt de ruis conventioneel geschat aan de hand van achtergrond data, welke Rayleigh verdeeld zijn. In hoofdstuk 4 wordt aangetoond dat de standaard afwijking van de ruis bij voorkeur via de Maximum Likelihood methode dient geschat te worden. Daarnaast wordt een methode voorgesteld voor het schatten van de ruis variantie aan de hand van twee realisaties van hetzelfde beeld.

In hoofdstuk 5 worden methodes voor het schatten van signaal, die conventioneel worden toegepast in magnitude MR beeldverwerking, vergeleken met de Maximum Likelihood (ML) schattingsmethode. Deze laatste methode maakt specifiek gebruik van de WDF die de data karakteriseert. Bovendien zijn ML schatters consistent en asymptotisch meest precies. Conventionele schattingsmethodes zijn veelal gebaseerd op Gaussisch verdeelde data. Aangezien magnitude en faze MR data niet 'normaal' verdeeld zijn, is het intuïtief duidelijk dat er fouten zullen sluipen in dergelijke schattingsprocedures. In hoofdstuk 4 en 5 wordt aangetoond dat het niet benutten van de kennis van de juiste WDF inderdaad kan leiden tot systematische afwijkingen bij het schatten van ruis of signaal. De ML schattingsmethode blijkt telkens superieur te zijn in termen van de gemiddelde kwadratische fout, welke een gecombineerde maat is voor precisie en juistheid.

In hoofdstuk 6 wordt het belang van ML schatten via de correcte WDF geïllustreerd aan de hand van het schatten van T_1- en T_2-mappen. Het construeren van deze mappen is een veel gebruikte techniek om karakteristieke fysiologische informatie te visualiseren. T_1- en T_2-mappen worden veelal afgeleid van magnitude MR data, welke Rice verdeeld zijn. Voor zover bekend werd deze voorkennis tot op heden echter nauwelijks benut. Nochtans heeft de Rice verdeling een significante invloed op de kwantitatieve bepaling van T_1- en T_2-mappen. In dit hoofdstuk wordt de conventionele kleinste-kwadraten schattingsmethode, welke gebaseerd is op Gaussisch verdeelde data, vergeleken met de ML schattingsprocedure. Figuren 6.2 en 6.3 op respectievelijk pagina 43 en 44 tonen de resultaten van simulatie-experimenten waarbij de pseudo-protondichtheid (de echte waarde is $\rho = 100$) geschat werd, samen met de T_1 of de T_2 parameter (de echte waarden zijn $T_1 = 2000$ ms en $T_2 = 100$ ms), en dit als functie van de signaal/ruis verhouding. Uit de figuren is het duidelijk dat de ML schattingsmethode superieur is qua juistheid.

In hoofdstuk 7 en 8 wordt er aandacht besteed aan respectievelijk het bepalen en het verbeteren van de signaal/ruis verhouding (SRV) in een beeld. In dit werk wordt een procedure voorgesteld om de SRV van een MR beeld te bepalen, gebaseerd op de kruiscorrelatie van twee realisaties van hetzelfde beeld. De methode is bijzonder efficiënt gezien kruiscorrelatie overeenstemt met een vermenigvuldiging in het Fourierdomein; dit is het domein waar de MR data bemonsterd worden. Kruiscorrelatie kan eveneens aangewend worden om de beeld-SRV te verbeteren (zie Fig. 8.1 op pagina 59). Echter, verbetering van de SRV gaat veelal gepaard met verlies aan ruimtelijke resolutie. Daarom wordt de adaptieve en anisotrope diffusie filter besproken welke in staat is de SRV sterk te verbeteren terwijl de ruimtelijke resolutie vrijwel intact blijft (zie ook Fig. 8.2 op pagina 61).

Tenslotte wordt in hoofdstuk 9 een segmentatie methode beschreven welke werd ontwikkeld voor nauwkeurige volume bepaling a.h.v. 3D MR beelden. De methode is semi-automatisch en laat toe op een interactieve manier het segmentatie proces te volgen. De segmentatie procedure is opgebouwd uit de volgende stappen:

- <u>Ruis filter</u>: Als eerste voorverwerkingsstap wordt een 3D, adaptieve en anisotrope diffusie filter

toegepast op de data. Figuur 9.2 op pagina 68 toont hier het effect van op de midsagitale snede. Merk op dat de randen goed bewaard blijven, wat erg belangrijk is voor latere segmentatie.

- <u>Watershed algoritme</u>: Na het filteren van de ruis, wordt een 3D watershed (waterscheiding) algoritme op de gradient magnitude van de data toegepast. Hierbij wordt de 3D data set onderverdeeld in een groot aantal, kleine, homogene volume-elementjes. Opdat deze onderverdeling nuttig zou zijn voor segmentatie dient dit aantal drastisch verminderd te worden, zonder daarbij volume-elementjes, behorende bij verschillende structuren, samen te voegen. Dankzij de diffusie filter werd dit aantal reeds sterk gereduceerd (zie figuur 9.3 op pagina 69).

- <u>Samenvoegen</u>: De oversegmentatie wordt in een tweede fase nogmaals sterk verminderd door het samenvoegen van naburige volume-elementjes. Dit gebeurt op basis van hun grijswaardenverdeling. Vooral de samenvoeging van de kleinste volume-elementjes krijgt hierbij de voorkeur gezien deze het segmentatieproces vertragen. Figuur 9.4 op pagina 70 toont het effect van de samenvoegingsfase.

- <u>Segmentatie</u>: De eigenlijke segmentatie start met het tonen van de eerste snede aan de gebruiker waarin het te segmenteren object verschijnt. Na manuele segmentatie van de eerste snede, waarbij de relevante volume-elementjes geactiveerd werden, wordt het resultaat gebruikt voor automatische segmentatie van de volgende snede. Eventueel volgt er een manuele correctie door de gebruiker. Figuur 9.6 op pagina 71 toont de segmentatie. Op deze manier wordt de volledige 3D data set doorlopen.

Na segmentatie kan het volume kwantitatief bepaald worden. Enkele voorbeelden van 3D reconstructies na segmentatie zijn weergegeven in figuur 9.7 en 9.8 op respectievelijk pagina's 72 en 74.
Experimenten wezen uit dat data voorverwerking met de 3D adaptieve anisotrope diffusie filter alsmede het samenvoegen van elementaire volume elementjes de segmentatietijd beduidend verkleint. De beschreven segmentatie techniek werd en wordt nog steeds gebruikt om op een accurate manier kwantitatieve volume informatie te extraheren uit 3D beelden van in vitro zowel als van in-vivo biologische strukturen.

Appendix D

Personalia

D.1   Curriculum Vitae

Jan Sijbers was born in Maaseik, Belgium, on the 13th of November 1971. He received the High School diploma from the H.-Kruis College Maaseik in June 1989. In September of the same year, he started the study of Physics at the Limburg University Center Diepenbeek. After two years, he went to the university of Antwerp, where he continued the Physics study. In 1993, he received his B. Sc. degree in Physics at the University of Antwerp, Belgium. Since then, he was working as an assistant within the BioMedical Physics group in cooperation with the Vision Lab and the BioImaging Lab at the University of Antwerp, where he prepared a doctoral thesis on signal and noise estimation from magnetic resonance (MR) data.

D.2   List of publications

D.2.1   Journal papers

- J. Sijbers, J.P. Straatman, P. Scheunders, and D. Van Dyck, "SNR quantification and improvement of multiple SPECT images by means of cross-correlation", European Journal of Nuclear Medicine, Vol. 23, Nr. 9, p. 1131, (1996)

- J. Sijbers, P. Scheunders, N. Bonnet, D. Van Dyck, and E. Raman, "Quantification and improvement of the signal-to-noise ratio in a magnetic resonance image acquisition procedure", Magnetic Resonance Imaging, Vol. 14, Nr. 10, p. 1157-1163, (1996)

- J. Sijbers, M. Verhoye, P. Scheunders, A. Van der Linden, D. Van Dyck, and E. Raman, "Watershed based segmentation of 3D MR data for volume quantization", Magnetic Resonance Imaging, Vol. 15, Nr. 6, p. 679-688, (1997)

- J. Sijbers, A.J. den Dekker, P. Scheunders, and D. Van Dyck, "Maximum Likelihood estimation of Rice distribution parameters", Submitted to IEEE Transactions on Medical Imaging, July, (1997)

- D. Van Dyck, E. Bettens, J. Sijbers, and M. Op de Beeck, "From high resolution image to atomic structure: how far are we?", Accepted for publication in Scanning Microscopy, (1998)

- J. Sijbers, A.J. den Dekker, J. Van Audekerke, M. Verhoye, and D. Van Dyck, "Estimation of the noise in magnitude MR images", Magnetic Resonance Imaging, Vol. 16, Nr. 1, p. 87-90, (1998)

- J. Sijbers, A.J. den Dekker, E. Raman, and D. Van Dyck, "On optimal parameter estimation from MR data with special reference to magnitude MR images", International Journal of Imaging Science and Technology. Invited paper in preparation, (1998)

D.2.2 Conference Proceedings

- J. Sijbers, E. Raman, J. Van Audekerke, W. Malfliet, A. Van der Linden, M. Verhoye, and C. Cloeck, "The construction of a gradient set", 4th Meeting of the FGWO/FRSM Contact Group Biomedical MR, p. 5, Louvain-la-Neuve, Belgium, May, (1993)

- J. Sijbers, P. Scheunders, D. Van Dyck, and E. Raman, "Optimization of the SNR in NMR images using image sequences", Proceedings of the Royal Microscopical Society, Vol. 29, Nr. 4, p. 232, London, UK, September, (1994)

- J. Sijbers, P. Scheunders, D. Van Dyck, and E. Raman, "The use of two NMR realizations for determining and improving of the image SNR", Proceedings of the Joint Meeting of the Belgian and Dutch Societies for Electron Microscopy, p. 65, Papendal, May, (1994)

- J. Sijbers, A. Van der Linden, P. Scheunders, J. Van Audekerke, D. Van Dyck, and E. Raman, "Volume quantization of the mouse cerebellum by semi-automatic 3D segmentation of MR images", Proceedings of SPIE Medical Imaging, Vol. 2710; p. 553-560, Newport Beach, CA, USA, February, (1996)

- J. Sijbers, A. Van der Linden, P. Scheunders, J. Van Audekerke, E. Raman, and D. Van Dyck, "Semi-automatic mouse cerebellum extraction from 3D magnetic resonance data", Proceedings of the International Society for Magnetic Resonance in Medicine, Vol. 3, p. 1585, New York, USA, May, (1996)

- M. Verhoye, A. Van der Linden, J. Sijbers, P. Scheunders, D. Van Dyck, E. Reniers, R.F. Kooy, P.J. Willems, P. Cras, and B.A. Oostra, "High resolution MRI study of the cerebellum of mice as a function of age, in a mouse model for fragile X mental retardation", Proceedings of the 13th Annual Meeting of the European Society for Magnetic Resonance in Medicine and Biology, Vol. IV, Nr. II, p. 168, Prague, Czech Republic, September, (1996)

- E. Bettens, P. Scheunders, J. Sijbers, D. Van Dyck, and L. Moens, "Automatic segmentation and modeling of two-dimensional electrophoresis gels", Proceedings ICIP'96 IEEE international conference on image processing, Vol II, p. 665-668, Lausanne, Switserland, September, (1996)

- J. Sijbers, M. Verhoye, P. Scheunders, A. Van der Linden, J. Van Audekerke, D. Van Dyck, and E. Raman, "Segmentation scheme for volume quantization from 3D microscopic MR images", Proceedings of the Joint Meeting NVvM and BVM, Information Beyond the Microscopical Image, p. 168-169, Ghent, Belgium, December, (1996)

- R.F. Kooy, E. Reyniers, R. D'Hooghe, P.P. De Deyn, A. Van der Linden, M. Verhoye, J. Sijbers, B. A. Oostra, and P. J. Willems, "Characterization of the Fragile X knockout mouse", Abstracts of the 2nd annual meeting of the Belgian society of neuroscience, Brussels, Belgium, May, (1997)

- R.F. Kooy, E. Reyniers, M. Verhoye, J. Sijbers, E. Fransen, C. Van Camp P. Cras, B.A. Oostra, A. Van der Linden, and P.J. Willems, "MRI as a tool to study brain structure from mouse models of mental retardation", Abstracts of the 8th international workshop on Fragile X syndrome and X-linked mental retardation", Picton, Ontario, Canada, August, (1997)

- J. Sijbers, A.J. den Dekker, P. Scheunders, E. Raman, and D. Van Dyck, "Unbiased signal estimation in magnitude MR images", Proceedings of ESMRMB'97: 14th annual meeting. Magnetic Resonance Materials in Physics, Biology, and Medicine, Vol. V, Nr. II, p. 174, Brussels, Belgium, September, (1997)

- D. Van Dyck, E. Bettens, J. Sijbers, A.J. den Dekker, A. Van den Bos, M. Op de Beeck, J. Jansen, and H. Zandbergen, "Resolving atoms: What do we have? What do we want?", EMAG'97 Electron Microscopy and Analysis Group Conference, Nr. 153, p. 95-100, Cavendish laboratory, Cambridge UK, September, (1997)

- M. Verhoye, J. Sijbers, P. Scheunders, D. Van Dyck, E. Reyniers, R.F. Kooy, P.J. Willems, P. Cras, B.A. Oostra, and A. Van der Linden, "In vivo assessment of cerebellum volume in transgenic fragile X knockout mice using MTI microscopy at 7T", Proceedings of ESMRMB'97: 14th annual meeting. Magnetic Resonance Materials in Physics, Biology, and Medicine, Vol. V, Nr. II, p. 45-46, Brussels, Belgium, September, (1997)

- J. Van Audekerke, M. Verhoye, J. Sijbers, T.J. DeVoogd, T. Smulders, S.W. Newman, and A. Van der Linden, "Imaging birds ... in a bird cage: In vivo MRI microscopy of the canary brain at 7T", Proceedings of ESMRMB'97: 14th annual meeting. Magnetic Resonance Materials in Physics, Biology, and Medicine, Vol. V, Nr. II, p. 162-163, Brussels, Belgium, September, (1997)

- P.J. Willems, E. Fransen, R.F. Kooy, R. D'Hooghe, J. Sijbers, A. Van der Linden, E,. Reyniers, P.P. De Deyn, and C. Van Camp, "Transgenic mice with a knockout mutation of l1, a neural cell adhesion molecule", American Journal of Human Genetics, Vol. 61, Nr. 2056, p. A351, Baltimore, October, (1997)

- J. Sijbers, A.J. den Dekker, D. Van Dyck, and E. Raman, "Estimation of signal and noise from Rician distributed data", Proceedings of the IASTED International Conferences on Signal Processing and Communications, p. 140-143, Gran Canaria, Canary Islands, Spain, February, (1998)

- J. Sijbers, A.J. den Dekker, M. Verhoye, D. Van Dyck, and E. Raman, "Optimal estimation of T_2 maps from magnitude MR data", Proceedings of SPIE Medical Imaging, San Diego, CA, USA, February, (1998).

- A.J. den Dekker, J. Sijbers, M. Verhoye, and D. Van Dyck, "Maximum Likelihood estimation of the signal component magnitude in phase contrast MR images", Proceedings of SPIE Medical Imaging, San Diego, CA, USA, February, (1998).

- M. Verhoye, J. Sijbers, R.F. Kooy, E. Reyniers, E. Fransen, B.A. Oostra, P.J. Willems, and A. Van der Linden, "MRI as a tool to study brain structure from mouse models of mental retardation", Proceedings of SPIE Medical Imaging, San Diego, CA, USA, February, (1998).

- A.J. den Dekker, J. Sijbers, and D. Van Dyck, "How to design an HREM experiment so as to attain the highest precision?", Submitted to the 14th International congress on Electron Microscopy, Mexico, (1998)